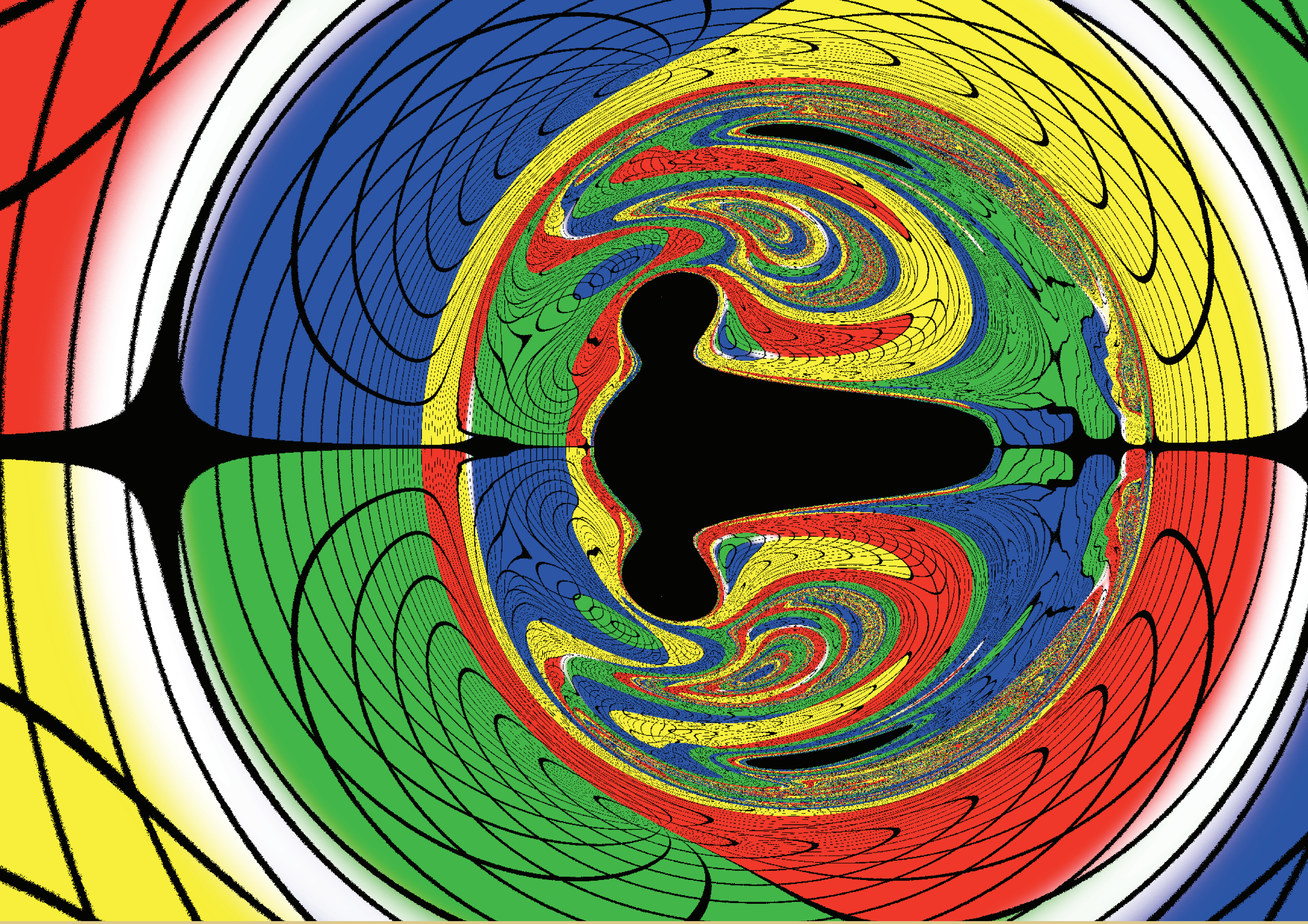

Pedro Vieira Pinto da Cunha

BLACK HOLE SHADOWS

SOMBRAS DE BURACOS NEGROS

Dissertação de Mestrado em Astrofísica e Instrumentação para o Espaço

21/9/2015

· U C ·

UNIVERSIDADE DE COIMBRA

Black Hole Shadows

Master thesis
University of Coimbra, Portugal

Pedro V. P. da Cunha

September 24, 2015

Dedicado à minha avó Nena,

Agradecimentos

Agradeço ao meu orientador, Prof. Carlos Herdeiro, pelo incansável apoio, ajuda e conselhos que me tem prestado durante todo o desenvolvimento deste projecto tão interessante, bem como ao grupo Gr@v de Aveiro pela sua hospitalidade. Gostaria igualmente de agradecer ao Laboratório de Computação Avançada da Universidade de Coimbra pelo acesso a recursos computacionais, e em particular ao Prof. Fernando Nogueira pela sua enorme ajuda e ao Prof. Rui Travasso que amavelmente me deixou usar o seu gabinete.

Numa nota mais pessoal, gostaria de agradecer à minha família, nomeadamente à minha mãe pelo seu encorajamento, ao meu pai por me lembrar que "as coisas antes de serem fáceis são difíceis". À minha irmã e amiga pelas suas sugestões de inglês (e a sua longa espera para ver Doctor Who comigo) e ao meu avô Emanuel pelo seu contínuo apoio. Queria também agradecer à Joana, minha namorada, pela inspiração e carinho, por ter estado presente nos momentos difícies, e pela sua paciência durante estas férias de Verão. Devo muito também muito aos meus amigos, em particular ao Maurício pela amizade, inúmeros conselhos e grande companhia, e ao Mário e ao Tiago pelos bons momentos de descontração no gabinete deles. Fica também uma nota de gratidão para todos os meus colegas, amigos e professores do Departamento de Física em Coimbra, que tornaram os últimos anos inesquecíveis. *Allons-y*!

Abstract

Black Holes (BHs) are predicted within Einstein's General Relativity, and they are a consequence of the gravitational collapse of matter into a extremely compact state, from which even light is prevented to escape. This master thesis explores the shadows of BHs and some of their fascinating properties. For an observer, a shadow is a BH's apparent shape in the sky due to gravitational lensing of nearby radiation, emitted by an external source. Not surprisingly, the shadow bears an indirect fingerprint of the space-time geometry around the BH. Kerr BHs, which are BHs with rotation, are presently the most "standard" solutions, and possibly also the most realistic ones. However, in order to provide alternative shadow templates for upcoming astronomical observations, namely for the observation of the supermassive BH candidate Sgr A* in the center of our galaxy by the *Event Horizon Telescope*, it is timely to also consider different types of solutions.

Hence, a novel class of BHs in equilibrium with a massive scalar field, dubbed "hair", was considered, exhibiting intriguing properties. The readers are assumed to be familiar with General Relativity, but not necessarily with BH physics. The first chapter of this thesis covers some important features of the Kerr solution, necessary for the following discussion on "hairy" BHs in the second chapter. This family of solutions yields interesting features, some of which are shadows that differ significantly from the Kerr prediction. In particular, during this thesis development it was discovered that these "hairy" BHs possess smaller shadows than the corresponding Kerr BHs. Additionally, under some conditions novel exotic shadow shapes can arise. Thus, hairy BHs could potentially provide new shadow templates for the aforementioned experiments.

These are the main results of this thesis, along with the analysis of gravitational lensing of Boson Stars (BSs). The latter are simply self-gravitating scalar configurations, described by the massive Klein-Gordon equation in curved space-time.

Two different "ray-tracing" algorithms were developed in order to represent the shadows, the first for Kerr BHs and the other for hairy BHs (plus BSs). Additionally, high definition images of the shadows were produced during this work. The main results presented here are qualitatively new and have already been submitted for publication.

Resumo

Os Buracos Negros (BNs) são previstos pela Relatividade Geral de Einstein, e são uma consequência do colapso gravitacional de matéria para um estado extremamente compacto, do qual a luz é impedida de escapar. Esta tese de

mestrado explora as sombras de BNs e algumas das suas propriedades fascinantes. Para um observador, uma sombra é a aparente forma do BN no céu devido ao efeito de lente gravitacional da radiação próxima, emitida por uma fonte externa. Não é pois surpreendente que a sombra seja uma manifestação indirecta da geometria do espaço-tempo em redor do BN. BNs de Kerr, que são BNs com rotação, são presentemente as soluções mais "padrão", e possivelmente também as mais realistas. No entanto, é necessário fornecer variados *templates* experimentais para analisar os futuros dados de observações astronómicas. Em particular, avizinha-se a observação do candidato a BN supermassivo Sgr A* no centro da nossa galáxia pelo *"Event Horizon Telescope"*. É pois actual e adequado também considerar outros tipos de soluções.

Deste modo, foi considerado uma nova classe de BNs em equilíbrio com um campo escalar, denominado "cabelo", exibindo propriedades intrigantes. Assume-se que os leitores estão familiarizados com a Relatividade Geral, mas não necessariamente com a física de BNs. O primeiro capítulo desta tese cobre alguns aspectos importantes da solução de Kerr, necessários para a discussão seguinte sobre BNs "cabeludos" no segundo capítulo. Esta família de soluções é caracterizada por alguns aspectos interessantes, entre os quais sombras que diferem de forma significativa das associadas a BNs de Kerr. Em particular, durante o desenvolvimento desta tese foi descoberto que estes BNs cabeludos possuem sombras mais pequenas do que os BNs de Kerr correspondentes, e também que sob certas condições novas formas exóticas podem aparecer para as mesmas. Portanto, os BNs cabeludos podem potencialmente fornecer novos *templates* experimentais para as referidas observações. Estes são os principais resultados da tese, juntamente com a análise do efeito de lente gravitacional de Estrelas de Bosões (EBs). Estas últimas são simplesmente configurações escalares que auto-gravitam, descritas pela equação massiva de Klein-Gordon em espaço-tempo curvo.
Dois algoritmos de *ray-tracing* foram desenvolvidos de forma a representar sombras, o primeiro para BNs de Kerr e o outro para BNs cabeludos (juntamente com EBs). Além disso, imagens de alta-definição foram desenvolvidas durante este trabalho. Os principais resultados aqui apresentados são qualitativamente novos e já foram submetidos para publicação.

Contents

Chapter 1

Kerr Black Holes

1.1 Brief introduction to Black Holes

Black Holes (BHs) are extremely compact objects predicted by Einstein's Theory of General Relativity and are one of the most enigmatic places in the universe. They are by definition "regions in space-time in which the gravitational field is so strong that it precludes even light from escaping to infinity" [1].
There is astronomical evidence for a supermassive Black Hole (BH) in our galaxy center, namely from star trajectories suffering a strong deviation by an extremely massive object (see Fig. 1.1.1) [2]. However, a large mass by itself does not imply the existence of a BH. A BH candidate must also be very compact, with a size not much larger than the gravitational radius $\sim GM/c^2$, where M is the mass of the object, G is the gravitational constant and c is the velocity of light in vacuum [3].

After BHs, neutron stars are the most compact objects in the cosmos and can be formed at the endpoint of stellar dynamics [4]. Still, the neutron-degeneracy pressure, which prevents the gravitational collapse, cannot overcome the gravitational attraction above a certain mass. Thus any compact astrophysical object detected with a mass bigger than $\approx 3M_\odot$ ($M_\odot$ is the solar mass) is thought to be a BH, since this is the expected upper mass limit for a neutron star [1, 3, 4].

Three possible types of BHs in the Universe are considered in modern astrophysics: stellar BHs, supermassive BHs and primordial BHs [1]. Stellar mass BHs are most likely created in the final stage of massive star collapse, due to the tremendous pressure in the star core and in situations where the fermionic pressure between particles is not enough to prevent further collapse [5,6]. Therefore this type of BH is expected to have a few star masses in order of magnitude ($\simeq 3M_\odot$ up to $\sim 10M_\odot$). In contrast, supermassive BHs

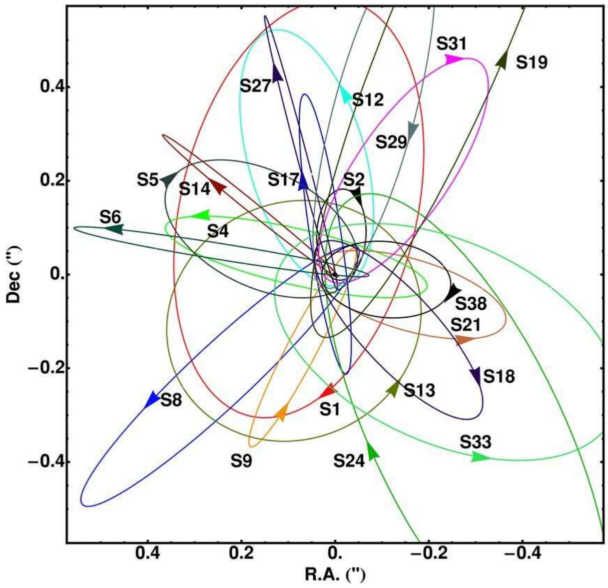

Figure 1.1.1: Plot of star orbits around a massive object dubbed Sagittarius A* (Sgr A*) in the center of our galaxy, the Milky Way. The coordinate system was chosen such that Sgr A* is at rest. This graph combines data from a survey that spanned 16 years. From this analysis it was possible to measure the mass of the object Sgr A* to be $(4.31 \pm 0.36) \times 10^6 M_\odot$, where $M_\odot$ is the mass of the Sun. It is suspected that this object is a supermassive BH. Image adapted from the article from Gillessen et al. (2009) [2].

found in the center of galaxies, like our Milky Way galaxy, can be millions of times more massive than stellar BHs (from $10^6 M_\odot$ up to $10^{10} M_\odot$) [1, 3]. It has also been hypothesized that some BHs could have been formed in the early stages of the expansion of the Universe, namely with microscopic sizes, due to the enormously high matter density at that time. Hence these are given the name primordial BHs. [1].

A surprising discovery was made recently, which implies that the mass of supermassive BHs correlate quite strongly with global properties of their host galaxies, namely luminosity and velocity dispersion. This correlation is fairly intriguing since typically the supermassive BH is 10^8 smaller and 10^3 less massive that his host galaxy [3]. At present however (2015), powerful accretion disk winds were observed, produced in a active galactic nuclei and driven by a supermassive BH [7]. These winds generate large scale molecular outflows, which influence the evolution of the entire galaxy. This process could hence be a possible mechanism which might explain the previous correlation.

According to the Theory of General Relativity (GR), the geometry of space-time is determined by the Einstein field equations

$$R_{\mu\nu} - \frac{1}{2} g_{\mu\nu} R = \frac{8\pi G}{c^4} T_{\mu\nu},$$

where $R_{\mu\nu}$ is the Ricci tensor, $g_{\mu\nu}$ is the metric, R is the Ricci scalar and $T_{\mu\nu}$ is the energy-momentum[1] tensor [5]. An extra term which incorporates the cosmological constant can also be included. The left-hand side of the equations concerns the geometric side of space-time, namely its curvature, whereas the right-hand side is connected to distribution of mass and energy. Thus curvature influences the distribution and motion of matter in the cosmos, but on the other hand matter (and energy) also determines the curvature of space-time.

The simplest BH solution to the Einstein equations is given by the Schwarzschild metric for a static, non-charged and spherically symmetric (non-rotating) BH in vacuum. However, more astrophysically relevant are uncharged spinning BHs in vacuum, described by the Kerr metric. The electric charge[2] is not likely to play a major role, due to the fact that in average matter in the cosmos is mostly neutral [1, 5].

1.1.1 Kerr metric in Boyer-Lindquist coordinates

The metric $g_{\mu\nu}$ of a hyper-space with n dimensions contains its relevant geometric information. The line element is generally written in the form:

$$ds^2 = g_{\mu\nu} dx^\mu dx^\nu,$$

where summation is implied by Einstein convention.

The space-time geometry in General Relativity ($n = 4$) for a spinning BH is given by the Kerr metric. In Boyer-Lindquist coordinates $\{t, r, \theta, \varphi\}$ this metric[3] is given by [5, 6]:

$$\begin{aligned} ds^2 = &-\left(1 - \frac{2mr}{\rho^2}\right) dt^2 - \left(\frac{4mar\sin^2\theta}{\rho^2}\right) dt d\varphi + \left(\frac{\rho^2}{\Delta}\right) dr^2 + \rho^2 d\theta^2 + \\ &+ \sin^2\theta \left(r^2 + a^2 + \frac{2mra^2\sin^2\theta}{\rho^2}\right) d\varphi^2. \end{aligned} \tag{1.1.1}$$

---

[1] The exponent of c depends on the units used for $T_{\mu\nu}$. For the present case, the scalar $T^\mu{}_\mu = T$ has units of energy density.

[2] However the so called Kerr-Newman metric for a spinning and electrically charged BH is also known [5].

[3] We use the $(-, +, +, +)$ signature convention [1].

The parameter m is given by $m = GM/c^2$ where M is the mass[4] of the BH [5]. Also, the expressions for ρ^2 and Δ are given by

$$\rho^2 = r^2 + a^2 \cos^2\theta,$$

$$\Delta = r^2 - 2mr + a^2.$$

The parameter a is related to the spin of the BH and it turns out to be the specific angular momentum $a = J/(Mc)$ (where J is the BH's angular momentum) [1, 5]. In order to prevent a naked singularity (one observable from infinity), as imposed by the *Cosmic Censorship Conjecture* [6, 8], the value of a is restricted to the interval $a \in [-m, m]$, or equivalently $m^2 \geq a^2$. A physical interpretation for this restriction (dubbed Kerr bound) comes from the fact that during the formation of a BH from matter, the centrifugal forces due to rotation cannot overcome the gravitational pull [9] (see also Appendix A.1). BHs with $|a| = m$ are also named "extremal" and correspond to the cases with maximum rotation. Notice also that the parameter m has dimensions of a distance and defines the scale of the physical system: a stellar and a supermassive BH are both equally described by the Kerr metric (in vacuum), although with different values of m (in S.I. units). Throughout the text sometimes the dimensionless rotation parameter $a_o = a/m$ is used instead of a.

Despite what the notation $\{t, r, \theta, \varphi\}$ used for Boyer-Lindquist coordinates might suggest, if $a \neq 0$ the limit $m \to 0$ (which is Minkowski space) does not yield spherical coordinates for the spatial part of the metric[5]. Instead, the coordinates $\{r, \theta, \varphi\}$ are part of a coordinate system with spheroidal symmetry, not spherical[6]. For instance, the set of spatial points defined by the condition $r = Const.$ is given by an ellipsoid of revolution. The deviation from a sphere is characterized by the rotation parameter a (for $a = 0$ we get a sphere). Despite this fact, usually the coordinate r is loosely called "radius" and surfaces of constant r are designated as "spherical"[7]. Also, the coordinate θ will sometimes be referred to as the "latitude" coordinate and φ as the "azimuthal" coordinate, due to their interpretation in the limit $a \to 0$ and $m \to 0$. For instance, the condition $\theta = \{0, \pi\}$ corresponds to the set of points in space-time along the BH's axis of rotation and the condition $\theta = \pi/2$ corresponds to the BH's equatorial plane.

---

[4] Some authors use units $c = 1$ and $G = 1$, which is equivalent to say that the m **is** the mass of the BH but measured in units of distance.

[5] The spatial part is obtained by setting $dt = 0$.

[6] Unless of course if $a = 0$, which yields spherical coordinates in the limit $m \to 0$.

[7] Although this surfaces are *topologically* spherical, they are certainly not *geometrically* spherical in most cases.

Notice that the coordinate t in (1.1.1) has spatial rather than time dimensions, as the symbol notation would naively suggest. In fact, in the limit $m \to 0$ (which is Minkowski space-time (flat space)), t does embody the classical time coordinate t^* by the transformation $t = ct^*$. Equivalently, we can use t as a time coordinate but in units $c = 1$ and with time as measured in units of distance.

A close inspection of the Kerr metric (1.1.1) reveals that no element $g_{\mu\nu}$ depends explicitly on either t or φ. This solution to the Einstein field equations is therefore stationary and also has axial symmetry. However it is not static, since the time reversal operation $t \to -t$ does not leave the metric invariant (due to the crossed term $dt\,d\varphi$). Only by applying both $t \to -t$ and $\varphi \to -\varphi$ is the solution unchanged. Each of these symmetries can be expressed by a *Killing*[8] *vector* field, namely ∂_t (stationary) and ∂_φ (axial symmetry), where the partial derivative operators stands for a coordinate basis vector field [5].

1.1.2 Inverse metric

For some purposes it is useful to compute the inverse metric $g^{\mu\nu}$:

$$\partial_s^2 = g^{\mu\nu}\partial_\mu\partial_\nu.$$

In this formalism the partial derivative operator ∂_ν stands for the coordinate basis vector associated with the coordinate ν; the element $\partial_\mu\partial_\nu$ stands for a tensor product $\partial_\mu \otimes \partial_\nu$ between basis vectors.
In Boyer-Lindquist coordinates the inverse metric is:

$$\begin{aligned}\partial_s^2 = -\frac{1}{\Delta}\left(r^2 + a^2 + \frac{2mra^2\sin^2\theta}{\rho^2}\right)\partial_t^2 - \left(\frac{4mar}{\Delta\rho^2}\right)\partial_t\partial_\varphi + \left(\frac{\Delta}{\rho^2}\right)\partial_r^2 \\ + \left(\frac{1}{\rho^2}\right)\partial_\theta^2 + \left(\frac{\rho^2 - 2mr}{\rho^2\Delta\sin^2\theta}\right)\partial_\varphi^2. \qquad (1.1.2)\end{aligned}$$

The elements of $g^{\mu\nu}$ were computed by assigning each component of the metric $g_{\mu\nu}$ to elements of a matrix and by using standard algebra techniques for matrix inversion [10].
Some of the inverse metric components can also be rewritten as:

$$g^{tt} = -\frac{1}{\rho^2\Delta}[(r^2 + a^2)^2 - a^2\Delta\sin^2\theta], \qquad (1.1.3)$$

---

[8] The Killing vectors express isometries, in the sense that the Lie derivative of the metric tensor is zero in the direction of those vectors. A Killing vector ξ^μ has then to satisfy the equation $\nabla_\nu\xi_\mu + \nabla_\mu\xi_\nu = 0$ [5,8].

$$2g^{t\varphi} = -\frac{2a}{\Delta\,\rho^2}(r^2 + a^2 - \Delta) \qquad \text{and} \qquad g^{\varphi\varphi} = \frac{\Delta - a^2 \sin^2\theta}{\rho^2 \Delta \sin^2\theta}. \tag{1.1.4}$$

1.1.3 Event horizon and ring singularity

The Kerr metric (1.1.1) has a singularity if either

$$\Delta = r^2 + a^2 - 2mr = 0, \tag{1.1.5}$$

or

$$\rho^2 = r^2 + a^2 \cos^2\theta = 0. \tag{1.1.6}$$

The roots of the equation (1.1.5) are coordinate singularities, as they can be eliminated by a change of coordinates. The condition $\Delta = 0$, or equivalently

$$r = r_\pm \equiv m \pm \sqrt{m^2 - a^2},$$

gives rise to two null surfaces r_- and r_+, with $r_- \leq r_+$; the surface defined by r_+ is commonly called event horizon. This surfaces is a “one-way membrane”, as it can only be crossed once [6], even by light. As a consequence, the event horizon r_+ is for an observer at infinity the limit from which information can be measured. In fact, any events that occur beyond this surface will never be observed for $r > r_+$ and so r_+ can be taken as the boundary of the BH. Therefore, throughout the text, analysis will be done outside r_+ and will be not continued inside[9] this surface.

The second equation (1.1.6) corresponds to a physical singularity, as it can be proven for instance that the Kretschmann scalar $R_{\mu\nu\alpha\beta}R^{\mu\nu\alpha\beta}$, which is invariant, is infinite in this region of space-time [8]. This singularity cannot be removed by any change of coordinates and it is thus an intrinsic property of the Kerr space-time. Equation (1.1.6) yields

$$r = 0 \qquad \text{and} \qquad \theta = \frac{\pi}{2}. \tag{1.1.7}$$

Notice that the condition $r = 0$ does not correspond to a single point in space-time if $a \neq 0$. In fact, recalling that the limit $m \to 0$ yields coordinates with spheroidal symmetry, embedding in Cartesian space of points satisfying condition $r = 0$ gives a disc of radius a. Condition (1.1.7) yields then only the edge of that disk, a ring singularity [8, 11].

As a final remark, notice that $\Delta = 0$ only has real roots if $m^2 \geq a^2$. Outside this range the singularity is not “cloaked” by an event horizon, giving rise to a naked singularity as was previously stated.

---

[9] By the words “beyond” or “inside” the event horizon surface it is meant $r < r_+$.

1.1.4 Ergoregion

For a static time-like observer/particle we have $dr = d\varphi = d\theta = 0$ and so the line element (1.1.1) becomes

$$ds^2_{\text{static}} = -\left(1 - \frac{2mr}{\rho^2}\right) dt^2.$$

For time-like trajectories we must have

$$ds^2_{\text{static}} < 0,$$

which requires

$$\left(1 - \frac{2mr}{\rho^2}\right) > 0.$$

This condition breaks down for

$$r_+ < \; r \; < m + \sqrt{m^2 - a^2\cos^2\theta}.$$

We conclude that in this region, which is outside the event horizon, it is impossible to have static observers. For reasons that will become apparent in a moment, this interval is called ergoregion. Also, the surface defined by $r = m + \sqrt{m^2 - a^2\cos^2\theta}$ is called ergosphere and only photons can be static on it. The ergosphere is therefore the static limit[10] [1]. Because g_{rr}, $g_{\theta\theta}$ and $g_{\varphi\varphi}$ are all positive for $r > r_+$ we must have in the ergoregion:

$$d\varphi > 0 \quad \text{if} \quad a > 0,$$

or

$$d\varphi < 0 \quad \text{if} \quad a < 0,$$

as consequence of the coupled term between t and φ (in the ergoregion it is the only negative metric term). A time-like particle/observer in this region is therefore "forced to rotate"[11] around the BH, and must do so in the sense of the spin. For instance, a trajectory in the ergoregion with opposite rotation relative to the BH would require a velocity higher than the speed of light, an impossible condition (see also [1, 12]). This result is independent of the angular momentum of the particle and it is valid even for counter-rotating particles at infinity that enter the ergoregion (see Fig. 1.1.2).

This effect is a consequence of the cross term $dtd\varphi$ in the metric and it is connected to frame-dragging, which is an angular shift in the azimuthal coordinate φ as measured by infinity, due to the fact that space-time itself

---

[10] In the ergoregion even photons cannot be static.

[11] A static observer at infinity will observe the particle rotate around the BH. The word "rotation" here is only associated with variations in the azimuthal coordinate φ.

is “dragged” by the BH spin [1,5]. Frame-dragging is not specific to the ergoregion, but it rather occurs in all space-time (although not equally for all points). The ergoregion is then the set of points in space-time with $r > r_+$ where frame-dragging is “too strong” to overcome (counter rotation is impossible). Notice however that particles can enter the ergoregion and still escape to infinity since the ergosphere is not a null surface.

It can be proven [5,13] that energy extraction is possible within the ergoregion by the so called Penrose process. In very simple terms, this consists on sending a particle A, that latter decays into particles B and C, inside the ergoregion (see Fig. 1.1.3). Particle C is created such in a way that its energy is negative in relation to infinity[12] and it is also absorbed by the BH. The energy of the BH is then decreased by C and if particle B escapes it will have more energy that the initial particle A, by conservation of the total energy. The difference comes in practice from the rotational energy of the BH, which decreases after this process is implemented [6].
This is part of the reason for the name: *ergo* in “ergoregion” comes from the Greek word for work [14].

---

[12] However, the energy measured by a local observer must be positive for physical particles

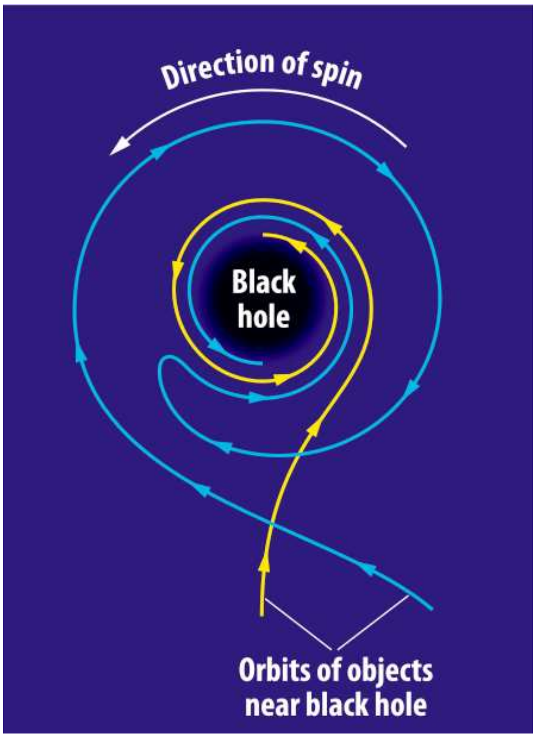

Figure 1.1.2: Any particle must rotate in the sense of the BH before entering the ergoregion, even for initially counter-rotating particles. Image adapted from [15].

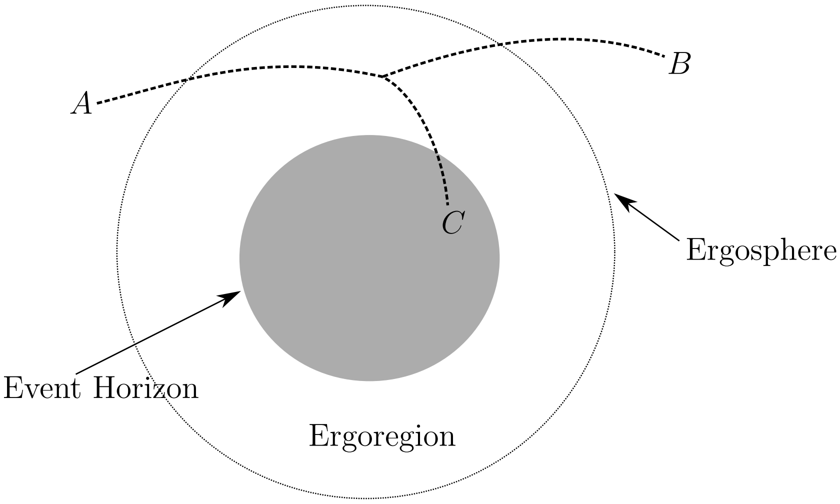

Figure 1.1.3: Illustrative drawing of the Penrose process. A particle A enters the ergoregion and decays into particle B and C. Particle C has negative energy in relation to infinity and is absorbed by the BH. Particle B escapes with more energy that particle A by conservation of the total energy. The grey area in the figure represents the BH.

1.2 Hamilton-Jacobi formalism in GR

Much can be learned by the the study of geodesics of massive particles and photons around BHs, leading to some insight about the underlining space-time physics. For the analytic study of this trajectories it is sometimes easier to use a certain type of formalism. In this section the Hamilton-Jacobi formalism is developed, in order to be used as a tool in the next section to understand geodesics in the Kerr metric.

1.2.1 Hamilton Equations

The geodesic equations of motion of a particle are obtained by requiring the action functional $\mathcal{S}[x^\mu]$ to be stationary[13] [6, 8, 16]:

$$\mathcal{S}[x^\mu] = \int_{\lambda_1}^{\lambda_2} L(x^\mu, \dot{x}^\mu, \lambda)\,\mathrm{d}\lambda,$$

where the Lagrangian[14] is given by $L(x^\mu, \dot{x}^\mu, \lambda) = \frac{1}{2} g_{\mu\nu} \dot{x^\mu} \dot{x^\nu}$. The set of n coordinates $\{x^\mu\}$ used is general and so the arguments used below do not rely on a specific coordinate system[15]. The metric of such a hyper-space $g_{\mu\nu}$ is assumed to depend only on the coordinates $\{x^\mu\}$. Also, the integration and the derivative $\dot{x}^\mu$ are given with respect to an affine parameter.

The proper time τ^* is the elapsed time in the rest frame of a given particle. It is a frame invariant quantity, which makes it a promising candidate for an affine parameter. However, following the nomenclature used for the coordinate t, we will use a parameter τ with spatial dimensions and related to proper time τ^* by $\tau = c\tau^*$ (see page 5). Despite this fact, the symbol τ will still be sloppily called "proper time", in order to be consistent with literature.

For time-like particles, the proper time τ is usually a good choice for an affine parameter. However, for null or massless particles there is no rest frame and so $d\tau = 0$; in this case τ is not good for parametrization or differentiation. It is then more convenient to use an affine parameter λ defined from the proper time τ by $\tau = \mu\lambda$. If the parameter μ (which here is not a component index!) is proportional to the rest mass of the particle, then the affine parameter λ can be used for both null and time-like particles, since

---

[13] For time-like particles this condition is equivalent to find an extremum for the proper-time (actually not necessarily an extremum but rather a stationary point).

[14] Observation regarding notation: The Einstein summation convention is implied throughout the text. Also, an index of a variable in functions is taken to be free (for instance in the expression $L(x^\mu, \dot{x}^\mu, \lambda)$, μ is a free index).

[15] For a space-time in General Relativity we consider the specific case $n = 4$.

$\mu = 0$ does not imply $d\lambda = 0$. We have then the following normalization [17]:

$$-d\tau^2 = g_{\mu\nu} dx^\mu dx^\nu,$$

$$-\mu^2 = g_{\mu\nu} \dot{x}^\mu \dot{x}^\nu.$$

By convention, the affine parameter λ is taken to be dimensionless. Since τ has spatial dimensions, then μ must also have dimensions of a distance. We conclude therefore, by dimensional analysis, that $\mu = G\mu^*/c^2$, where μ^* is the rest mass. If units $c = 1$ and $G = 1$ are used however, then μ is the same as the mass of the particle (see also footnote 22 on page 17).

The Euler-Lagrange equations provide the stationary condition for the functional $\mathcal{S}[x^\mu]$:

$$\frac{\partial L}{\partial x^\mu} = \frac{d}{d\lambda}\left(\frac{\partial L}{\partial \dot{x}^\mu}\right). \tag{1.2.1}$$

This equation gives n second order differential equation for the geodesic motion of the particle.

The physical domain of $L(x^\mu, \dot{x}^\mu, \lambda)$ is restricted by the normalization condition to the hyper-surface $-\frac{\mu^2}{2} = L(x^\mu, \dot{x}^\mu, \lambda)$. Defining the conjugate momenta as

$$p_\mu = \frac{\partial L}{\partial \dot{x}^\mu} = g_{\mu\nu} \dot{x}^\nu,$$

the Hamiltonian is given by the Legendre transform:

$$\boxed{H(x^\mu, p_\mu, \lambda) = p_\mu \dot{x}^\mu - L(x^\mu, \dot{x}^\mu, \lambda).} \tag{1.2.2}$$

Hence:

$$H = g_{\mu\nu} \dot{x}^\mu \dot{x}^\nu - \frac{1}{2} g_{\mu\nu} \dot{x}^\mu \dot{x}^\nu = \frac{1}{2} g_{\mu\nu} \dot{x}^\mu \dot{x}^\nu = L.$$

Consequently H has the same magnitude as the Lagrangian L and so there are no potentials involved (the motion only depends on the curvature of space-time) [14]. However these two functions have different functional dependencies, as in this formalism p_μ is an independent coordinate (p_μ is connected to x^μ and $\dot{x}^\mu$ only *a posteriori* by the equations of motion[16]) [18].

---

[16] Observation: Defining

$$p_\mu - \frac{\partial}{\partial \dot{x}^\mu} L(x^\mu, \dot{x}^\mu, \lambda) = \xi(p_\mu, x^\mu, \dot{x}^\mu, \lambda),$$

where $p_\mu, x^\mu, \dot{x}^\mu$ and λ are independent coordinates, and the Hamiltonian as

$$H(x^\mu, \dot{x}^\mu, p_\mu, \lambda) = p_\mu \dot{x}^\mu - L(x^\mu, \dot{x}^\mu, \lambda), \qquad \text{we get} \qquad \frac{\partial H}{\partial \dot{x}^\mu} = p_\mu - \frac{\partial}{\partial \dot{x}^\mu} L = \xi(p_\mu, x^\mu, \dot{x}^\mu, \lambda).$$

Restricting ourselves by choice to the hyper-surface $\xi(p_\mu, x^\mu, \dot{x}^\mu, \lambda) = 0$, the Hamiltonian does not have an effective dependence on $\dot{x}^\mu$, but the coordinates $\{p_\mu, x^\mu, \dot{x}^\mu, \lambda\}$ are still strictly speaking independent, there is only a implicit dependence *a posteriori*.

Nonetheless, in the end of the day $\dot{x}_\mu = p_\mu$ in magnitude; this symbol notation is fortunate since for the normalization used $\underline{\dot{x}}$ is the 4-momentum vector[17] in units $c = 1$, $G = 1$. If this units are not used then $\underline{p} = G\,\underline{p^*}/c^3$, with $\underline{p^*}$ in S.I. units[18].

H is then a $2n$ coordinate function:

$$H(x^\mu, p_\mu, \lambda) = \frac{1}{2} g^{\mu\nu} p_\mu p_\nu. \tag{1.2.3}$$

The geodesic motion can also be obtained from Hamilton equations [18], starting from Euler-Lagrange:

$$\frac{\partial H}{\partial x^\mu} = -\frac{\partial L}{\partial x^\mu} = -\frac{d}{d\lambda}\left(\frac{\partial L}{\partial \dot{x}^\mu}\right) = -\frac{d}{d\lambda} p_\mu = -\dot{p}_\mu.$$

Because $\dot{x}^\mu$ is independent of p_μ we get:

$$\dot{p}_\mu = -\frac{\partial H}{\partial x^\mu}(x^\mu, p_\mu, \lambda), \tag{1.2.4a}$$
$$\dot{x}^\mu = \frac{\partial H}{\partial p_\mu}(x^\mu, p_\mu, \lambda). \tag{1.2.4b}$$

Those $2n$ first order differential equations are called the Hamilton equations. This set contains the same information as the n Euler-Lagrange equations (1.2.1), and both lead to the same geodesic motion. Additionally, we have:

$$\frac{\partial H}{\partial \lambda} = -\frac{\partial L}{\partial \lambda}.$$

The Hamilton equations can also be obtained from the variational principle, by requiring the action functional to be stationary:

$$\int_{\lambda_1}^{\lambda_2} L(x^\mu, \dot{x}^\mu, \lambda) d\lambda = \int_{\lambda_1}^{\lambda_2} \left(p_\mu \dot{x}^\mu - H(x^\mu, p_\mu, \lambda)\right) d\lambda = \int_{\lambda_1}^{\lambda_2} f(x^\mu, \dot{x}^\mu, p_\mu, \dot{p}_\mu, \lambda) d\lambda.$$

Formally speaking the last integral can be taken as a functional of $2n$ independent coordinates x^μ and p_μ, although f does not depend effectively on $\dot{p}_\mu$. So without loss of generality we can fix $\delta p_\mu = 0$ for $\lambda = \{\lambda_1, \lambda_2\}$, in addition to the condition $\delta x^\mu = 0$ in those points. Therefore, the variational principle can be generalized to the coordinate set $\{x^\mu, p_\mu\}$.

---

[17] The notation $\underline{a}$ represents the full vector $\underline{a} = a^\mu \partial_\mu$.

[18] By units of a vector $\underline{a}$ it is meant the units of its norm $\sqrt{a^\mu a_\mu}$.

From the Euler-Lagrange equations (1.2.1) for the $2n$ coordinate function f:

$$\frac{d}{d\lambda}\left(\frac{\partial f}{\partial \dot{x}^\mu}\right) = \frac{\partial f}{\partial x^\mu} \quad \longrightarrow \quad \frac{d}{d\lambda}\left(p_\mu\right) = -\frac{\partial H}{\partial x^\mu} \quad \longrightarrow \quad \frac{\partial H}{\partial x^\mu} = -\dot{p}_\mu,$$

$$\frac{d}{d\lambda}\left(\frac{\partial f}{\partial \dot{p}_\mu}\right) = \frac{\partial f}{\partial p_\mu} \quad \longrightarrow \quad \frac{\partial f}{\partial p_\mu} = 0 \quad \longrightarrow \quad \frac{\partial H}{\partial p_\mu} = \dot{x}^\mu.$$

We obtain Hamilton equations as expected (see (1.2.4)). We conclude that the geodesic equations can be obtained by applying the variational principle to the integral:

$$\int_{\lambda_1}^{\lambda_2} \left(p_\mu \dot{x}^\mu - H(x^\mu, p_\mu, \lambda)\right) d\lambda.$$

1.2.2 Canonical transformations

The coordinates used were general, so it should also be possible to write the Lagrangian L' in another system of coordinates $\{Q^\mu, \dot{Q}^\mu\}$ with equivalent geodesic motion[19]. The Hamiltonian in this coordinates will take the form:

$$K(Q^\mu, P_\mu, \lambda) = P_\mu \dot{Q}^\mu - L'(Q^\mu, \dot{Q}^\mu, \lambda),$$

where the canonical momenta is

$$P_\mu = \frac{\partial L'}{\partial \dot{Q}^\mu}(Q^\mu, \dot{Q}^\mu, \lambda).$$

We use a different symbol for the Hamiltonian because $K(Q^\mu, P_\mu, \lambda)$ is a distinct function from $H(x^\mu, p_\mu, \lambda)$; however K is simply the same Hamiltonian in a different coordinate system and written in a different form [18].

In fact, this corresponds to assign new coordinates to the same point in phase space $(x^\mu, p_\mu) \longrightarrow (Q^\mu, P_\mu)$. Canonical transformations is the set of transformations in phase space that preserves the form of the Hamilton equations:

$$\frac{\partial K}{\partial Q^\mu}(Q^\mu, P_\mu, \lambda) = -\dot{P}_\mu,$$
$$\frac{\partial K}{\partial P_\mu}(Q^\mu, P_\mu, \lambda) = \dot{Q}^\mu.$$

The variational principle applied to the following integrals should lead to the same geodesic motion:

$$\delta \int_{\lambda_1}^{\lambda_2} \left(p_\mu \dot{x}^\mu - H(x^\mu, p_\mu, \lambda)\right) d\lambda = \delta \int_{\lambda_1}^{\lambda_2} \left(P_\mu \dot{Q}^\mu - K(Q^\mu, P_\mu, \lambda)\right) d\lambda = 0.$$

---

[19] The following reasoning strongly follows the book by Goldstein [18].

Of course the integrand functions are not necessarily equal, only the stationary solution for each functional is equivalent. Each of these solutions is invariant by multiplying a constant σ and by adding the derivative of a function F, namely $\frac{dF}{d\lambda}$. This function F only depends on the coordinates and should have continuous second order derivatives [18].

The integrand functions should then be related by:

$$\sigma\left(p_\mu \dot{x}^\mu - H(x^\mu, p_\mu, \lambda)\right) = P_\mu \dot{Q}^\mu - K(Q^\mu, P_\mu, \lambda) + \frac{dF}{d\lambda}.$$

The factor σ is only associated with a scale change and is always possible to find a scale transformation to intermediate coordinates $(x^\mu, p_\mu) \longrightarrow (x'^\mu, p'_\mu)$ such that $\sigma = 1$ for the transformation $(x'^\mu, p'_\mu) \longrightarrow (Q^\mu, P_\mu)$. So without loss of generality we will set $\sigma = 1$.

We have then:

$$p_\mu \dot{x}^\mu - H(x^\mu, p_\mu, \lambda) = P_\mu \dot{Q}^\mu - K(Q^\mu, P_\mu, \lambda) + \frac{dF}{d\lambda}.$$

The function F can depend on any of the coordinates $\{x^\mu, p_\mu, Q^\mu, P_\mu, \lambda\}$, as the variation of any of them is zero for $\lambda = \{\lambda_1, \lambda_2\}$, and so it does not affect the stationary solution of the functional (although it can shift the value of the integral by a constant value).

The function F is most useful when half the variables are from the old coordinate set and the other half from the new one. F works then like a "bridge" between the two systems, establishing an implicit connection between them. That is why F is usually called a "generating function".

We now define $F(x^\mu, Q^\mu, \lambda) = S(x^\mu, P_\mu, \lambda) - Q^\mu P_\mu$ where S is called action function and also constitute a generating function.
We then have:

$$\begin{aligned} \frac{dF}{d\lambda} &= \frac{dS}{d\lambda} - \dot{Q}^\mu P_\mu - Q^\mu \dot{P}_\mu, \\ &= \frac{\partial S}{\partial x^\mu}\dot{x}^\mu + \frac{\partial S}{\partial P_\mu}\dot{P}_\mu + \frac{\partial S}{\partial \lambda} - \dot{Q}^\mu P_\mu - Q^\mu \dot{P}_\mu. \end{aligned}$$

So we get:

$$p_\mu \dot{x}^\mu - H(x^\mu, p_\mu, \lambda) = \cancel{P_\mu \dot{Q}^\mu} - K(Q^\mu, P_\mu, \lambda) + \frac{\partial S}{\partial x^\mu}\dot{x}^\mu + \frac{\partial S}{\partial P_\mu}\dot{P}_\mu + \frac{\partial S}{\partial \lambda} - \cancel{\dot{Q}^\mu P_\mu} - Q^\mu \dot{P}_\mu,$$

which can be organized into

$$\left(\frac{\partial S}{\partial x^\mu} - p_\mu\right)\dot{x}^\mu + \left(\frac{\partial S}{\partial P_\mu} - Q^\mu\right)\dot{P}_\mu + \left(H + \frac{\partial S}{\partial \lambda} - K\right) = 0.$$

Because $\dot{x}^\mu$ and $\dot{P}_\mu$ are both independent, this relation requires [18]:

$$\frac{\partial S}{\partial x^\mu}(x^\mu, P_\mu, \lambda) = p_\mu, \tag{1.2.5a}$$

$$\frac{\partial S}{\partial P_\mu}(x^\mu, P_\mu, \lambda) = Q^\mu, \tag{1.2.5b}$$

$$H(x^\mu, p_\mu, \lambda) + \frac{\partial S}{\partial \lambda}(x^\mu, P_\mu, \lambda) = K(Q^\mu, P_\mu, \lambda). \tag{1.2.5c}$$

This set of equations makes the connection from the old coordinates (x^μ, p_μ) to the new ones (Q^μ, P_μ) and the relation between the different forms of the Hamiltonian H and K.

1.2.3 Hamilton-Jacobi equation

In the Hamilton-Jacobi formalism the new coordinates (Q^μ, P_μ) are chosen such that they are constants of motion, namely associated with the initial conditions of the problem. The idea is that by knowing $x^\mu(Q^\mu, P_\mu, \lambda)$ we have obtained a solution to the motion of the particle.

Choosing $K = 0$ it is assured that Q^μ and P_μ are constants of motion, since:

$$\frac{\partial K}{\partial Q^\mu} = -\dot{P}_\mu = 0,$$

$$\frac{\partial K}{\partial P_\mu} = \dot{Q}^\mu = 0.$$

We then obtain the equation:

$$\frac{\partial S}{\partial \lambda}(x^\mu, P_\mu, \lambda) + H(x^\mu, p_\mu, \lambda) = 0,$$

with $p_\mu = \frac{\partial S}{\partial x^\mu}$. It is then possible to write a differential equation for the action function $S(x^\mu, P_\mu, \lambda)$ called Hamilton-Jacobi equation:

$$\boxed{H\left(x^\mu, \frac{\partial S}{\partial x^\mu}, \lambda\right) = -\frac{\partial S}{\partial \lambda}.} \tag{1.2.6}$$

The Hamilton-Jacobi equation contains $n+1$ partial derivatives of the function S, associated with $n+1$ integration constants. However the total function S does not appear itself in the equation, only its derivatives. Any transformation of the form $S \longrightarrow S + Const.$ still gives the same physical solution. There is therefore one extra degree of freedom in the integration constants that has no significance. So we conclude that S has in fact n integration constants to be evaluated.

Designating the n significant constants of integration α_μ, there is liberty in choosing $\alpha_\mu = P_\mu$; however the choice of the constants is to a certain extent arbitrary, as we can equally choose $\alpha_\mu = \alpha_\mu(P_\nu)$. In that case the action S has the functional dependence $S = S(x^\mu; \alpha_\mu; \lambda)$ (here a semicolon ";" is used instead of a comma "," to distinguish from the S dependence on P_μ.)

Because $\frac{\partial \alpha_\mu}{\partial P_\nu} = Const.$, we have:

$$\frac{\partial S}{\partial \alpha_\mu} = \frac{\partial S}{\partial P_\nu}\frac{\partial P_\nu}{\partial \alpha_\mu} = Q^\nu \frac{\partial P_\nu}{\partial \alpha_\mu} = Const. \equiv \beta^\mu,$$

where β^μ is also a constant of motion (see 1.2.5).
In the end this is equivalent to the transformation $(Q^\mu, P_\mu) \longrightarrow (\beta^\mu, \alpha_\mu)$ [18].

After a given function S has been determined that satisfies the Hamilton-Jacobi equation is then possible to establish a connection between the coordinates (x^μ, p_μ) and (β^μ, α_μ).

From (1.2.5) we have that $\frac{\partial S}{\partial x^\mu}(x^\mu; \alpha_\mu; \lambda) = p_\mu$, and so for a given value $\lambda = \lambda_o$ for which the initial conditions are defined, we can obtain the values of the constants α_μ as function of the initial values of x^μ and p_μ (n equations for n unknowns).

Because $\frac{\partial S}{\partial \alpha_\mu}(x^\mu; \alpha_\mu; \lambda) = \beta^\mu$, for $\lambda = \lambda_o$, we can obtain the values of the constants β^μ as function of the initial values of x^μ and the values of the constants α_μ already obtained (n equations for n unknowns).

Finally $x^\mu(\beta^\mu; \alpha_\mu; \lambda)$ can be obtained using the last equation "inside out" for any value of λ. At this point the solution is complete.

1.2.4 Cyclic coordinates

For the special case that a given coordinate x^a with $\mu = a$ is cyclic, or $\frac{\partial H}{\partial x^a} = 0$, the physical system is invariant along that coordinate and has an associated symmetry.

From Hamilton equations:

$$\frac{\partial H}{\partial x^a} = -\dot{p}_a = 0 \implies p_a = Const. \equiv \gamma.$$

Because $\frac{\partial S}{\partial x^\mu} = p_\mu$ this implies that:

$$\gamma = \frac{\partial S}{\partial x^a}(x^\mu; \alpha_\mu; \lambda) \longrightarrow S = \gamma x^a + \widetilde{S}(x^\mu; \alpha_\mu; \lambda)_{\mu \neq a}.$$

So for each cyclic coordinate x^a is possible to write a term in S associated with that coordinate in the form $x^a p_a$, where p_a is constant.

1.3 Hamilton-Jacobi equation in Kerr space-time

The Hamiltonian in General Relativity is given by (see (1.2.3)):

$$H(x^\mu, p_\mu, \lambda) = \frac{1}{2} g^{\mu\nu} p_\mu p_\nu.$$

The Hamilton-Jacobi equation in (1.2.6),

$$H\left(x^\mu, \frac{\partial S}{\partial x^\mu}, \lambda\right) = -\frac{\partial S}{\partial \lambda},$$

gives then:

$$\frac{1}{2} g^{\mu\nu} \frac{\partial S}{\partial x^\mu} \frac{\partial S}{\partial x^\nu} = -\frac{\partial S}{\partial \lambda}.$$

In the Kerr space-time, due to the symmetry of the problem, the Hamiltonian does not depend explicitly on t, φ and λ (see (1.1.1)), giving rise to three different separable terms in the function S:

$$S(x^\mu; \alpha_\mu; \lambda) = p_t t + p_\varphi \varphi + \gamma \lambda + S_2(r, \theta),$$

with[20]

$$\frac{\partial S}{\partial \lambda} = \gamma = -H = \frac{\mu^2}{2}.$$

The conserved quantities $E \equiv -p_t$ and $p_\varphi \equiv \Phi$ turn out to be respectively the energy and the axial (z) component of the angular momentum in relation to infinity[21], if units $c = 1$ and $G = 1$ are used[22]. See also footnote 42 on page 44.

---

[20] Observation: μ in this next equation is the rest mass of the particle, not an index component!

[21] More specifically in relation to a static observer at infinity.

[22] In S.I. units: $\Phi = G\Phi^*/c^3$, $E = GE^*/c^4$ and $\mu = G\mu^*/c^2$, where Φ^* and E^* are respectively the z component of the angular momentum and the energy with respect to infinity; also μ^* is the rest mass of the particle. However for simplicity and following the standard nomenclature in literature, Φ, E and μ are named after the respective physical quantities.

1.3.1 Variable separation

We now assume that the function $S_2(r,\theta)$ can be decoupled [14, 19] into two terms of the form

$$S_2(r,\theta) = S_r(r) + S_\theta(\theta).$$

If S is built from this ansatz, and it is a solution to the Hamilton-Jacobi equation then it should provide the correct motion for the particle.
According to the ansatz, the function S then becomes

$$S(x^\mu;\alpha_\mu;\lambda) = \frac{\mu^2}{2}\lambda - Et + \Phi\varphi + S_r(r) + S_\theta(\theta).$$

Substitution in the Hamilton-Jacobi equation yields:

$$\frac{1}{2}g^{tt}\,[\partial_t S]^2 + \frac{2}{2}g^{\varphi t}\,\partial_t S\,\partial_\varphi S + \frac{1}{2}g^{rr}\,[\partial_r S]^2 + \frac{1}{2}g^{\theta\theta}\,[\partial_\theta S]^2 + \frac{1}{2}g^{\varphi\varphi}\,[\partial_\varphi S]^2 = -\partial_\lambda S,$$

$$\underbrace{g^{tt}E^2 + g^{\varphi\varphi}\Phi^2 - 2g^{t\varphi}E\Phi}_{\mathcal{C}} + g^{rr}\left(\frac{dS_r}{dr}\right)^2 + g^{\theta\theta}\left(\frac{dS_\theta}{d\theta}\right)^2 = -\mu^2.$$

Explicitly (see (1.1.3) and (1.1.4)):

$$\mathcal{C} = -\frac{E^2}{\rho^2\Delta}[(r^2+a^2)^2 - a^2\Delta\sin^2\theta] + \frac{(\Delta - a^2\sin^2\theta)\Phi^2}{\rho^2\Delta\sin^2\theta} + \frac{2E\Phi a(r^2+a^2-\Delta)}{\Delta\rho^2},$$

$$\mathcal{C} = \left(-\frac{E^2(r^2+a^2)^2}{\rho^2\Delta} - \frac{a^2\Phi^2}{\rho^2\Delta} + \frac{2a(r^2+a^2)E\Phi}{\rho^2\Delta}\right) + \left(\frac{E^2a^2\sin^2\theta}{\rho^2} + \frac{\Phi^2}{\rho^2\sin^2\theta} - \frac{2aE\Phi}{\rho^2}\right).$$

This expression can be simplified using factorization [20]:

$$\mathcal{C} = -\frac{1}{\rho^2\Delta}[\underbrace{E(r^2+a^2) - a\Phi}_{P}]^2 + \frac{1}{\rho^2\sin^2\theta}[aE\sin^2\theta - \Phi]^2.$$

Using $p_r(r) = \partial S/\partial r$ and $p_\theta(\theta) = \partial S/\partial\theta$, the initial expression becomes

$$\mathcal{C} + \frac{\Delta}{\rho^2}p_r^2 + \frac{1}{\rho^2}p_\theta^2 = -\mu^2,$$

$$-\frac{1}{\rho^2\Delta}P^2 + \frac{1}{\rho^2\sin^2\theta}[aE\sin^2\theta - \Phi]^2 + \frac{\Delta}{\rho^2}p_r^2 + \frac{1}{\rho^2}p_\theta^2 = -\mu^2.$$

Multiplication by $\rho^2\Delta\sin^2\theta$ on both sides yields:

$$-P^2\sin^2\theta+\Delta[aE\sin^2\theta-\Phi]^2+p_r^2\Delta^2\sin^2\theta+p_\theta^2\Delta\sin^2\theta=-\rho^2\Delta\mu^2\sin^2\theta.$$

Expanding the ρ^2 factor and moving the terms with only θ dependence on $\sin^2\theta$ to the left side of the equation:

$$-P^2\sin^2\theta+p_r^2\Delta^2\sin^2\theta+\Delta\,r^2\mu^2\sin^2\theta=-\Delta\left(a^2\mu^2\sin^2\theta\cos^2\theta+[aE\sin^2\theta-\Phi]^2+\,p_\theta^2\sin^2\theta\right).$$

Dividing by $\Delta\sin^2\theta$:

$$\frac{-P^2+\Delta^2p_r^2+\Delta\,r^2\mu^2}{\Delta}=f_r(r)=f_\theta(\theta)=-a^2\mu^2\cos^2\theta-\left(aE\sin\theta-\frac{\Phi}{\sin\theta}\right)^2-p_\theta^2.$$

Because $\Delta(r)$ and $P(r)$, the left side of the equation only depends on r and the right side only depends on θ. This equality implies that both sides are equal to a constant [19,21] that we define as:

$$f_r(r)=f_\theta(\theta)=Const.\equiv-K.$$

where K is a constant of motion. Sometimes other conserved quantity is used:

$$Q\equiv K-(aE-\Phi)^2.$$

This constant Q is called Carter constant after Brandon Carter. Its geometric interpretation is not obvious, although it is related to θ motion [17,21].

Starting from the left side:

$$\Delta^2p_r^2=P^2-\Delta[Q+(aE-\Phi)^2+\mu^2r^2].$$

Using the relation $\dot r=p^r=g^{rr}p_r=\frac{\Delta}{\rho^2}p_r$, we can write the equation of motion in r:

$$\boxed{\rho^2\dot r=\pm\sqrt{R},}\qquad\text{with}\qquad\boxed{R\equiv P^2-\Delta[Q+(aE-\Phi)^2+\mu^2r^2]},\qquad(1.3.1)$$

and $P = E(r^2 + a^2) - a\Phi$.

The θ equation of motion can be obtained from the right side of the initial equation:

$$K = a^2\mu^2\cos^2\theta + \left(aE\sin\theta - \frac{\Phi}{\sin\theta}\right)^2 + p_\theta^2.$$

From this relation it is clear that we must have:

$$K \geq 0,$$

$$p_\theta^2 = Q - a^2\mu^2\cos^2\theta + \underbrace{(aE - \Phi)^2 - \left(aE\sin\theta - \frac{\Phi}{\sin\theta}\right)^2}_{\zeta}.$$

Simplifying the ζ term:

$$\zeta = (a^2E^2 + \Phi^2 - \cancel{2aE\Phi}) - \left(a^2E^2\sin^2\theta + \frac{\Phi^2}{\sin^2\theta} - \cancel{2aE\Phi}\right),$$

$$\zeta = a^2E^2\cos^2\theta - \frac{\Phi^2\cos^2\theta}{\sin^2\theta}.$$

Therefore we have:

$$p_\theta^2 = Q - \cos^2\theta\left(a^2(\mu^2 - E^2) + \frac{\Phi^2}{\sin^2\theta}\right).$$

Using $\dot\theta = p^\theta = g^{\theta\theta}p_\theta = \frac{1}{\rho^2}p_\theta$ we obtain the θ equation of motion:

$$\boxed{\rho^2\dot\theta = \pm\sqrt{\Theta},} \quad \text{with} \quad \boxed{\Theta = Q - \cos^2\theta\left(a^2(\mu^2 - E^2) + \frac{\Phi^2}{\sin^2\theta}\right).} \tag{1.3.2}$$

1.3.2 Motion in t and φ

Due to the symmetry of the problem, the following conjugate momenta are conversed:

$$p_t = -E \qquad \text{and} \qquad p_\varphi = \Phi.$$

For t:

$$p^t = g^{tt}p_t + g^{t\varphi}p_\varphi.$$

So we get:

$$\boxed{\rho^2\dot t = \frac{E}{\Delta}[(r^2 + a^2)^2 - a^2\Delta\sin^2\theta] - \frac{2mar}{\Delta}\Phi.} \tag{1.3.3}$$

For φ:

$$p^\varphi = g^{\varphi t}p_t + g^{\varphi\varphi}p_\varphi,$$

$$\boxed{\rho^2\dot{\varphi} = \frac{2maEr}{\Delta} + \Phi\frac{(\Delta - a^2\sin^2\theta)}{\Delta\sin^2\theta}.} \tag{1.3.4}$$

1.3.3 Solution in integral form

The equations of motion obtained in the previous subsection completely determine the tangent vector $dx^\mu/d\lambda$ along the geodesic path (see (1.3.1), (1.3.2), (1.3.3) and (1.3.4)). The trajectory can thus be found directly by numerical integration. However, a full solution can still be obtained in integral form.

From a close analysis of the equations of motion we can conclude that there is still coupling between different coordinates, namely θ and r. To avoid integrals with mixing coordinates one can continue to use the Hamilton-Jacobi approach and also use the fact that derivatives of the action function S with respect to the constants of integration α_μ are also constants (see section 1.2.3).

Making use of the relations $p_r = \partial S_r(r)/\partial r$ and $p_\theta = \partial S_\theta(\theta)/\partial\theta$, the action S can be written as [22]:

$$S(x^\mu;\alpha_\mu;\lambda) = \frac{\mu^2}{2}\lambda - Et + \Phi\varphi + \varepsilon_r\int^r \frac{\sqrt{R}}{\Delta}\,dr + \varepsilon_\theta\int^\theta \sqrt{\Theta}\,d\theta.$$

The integrals here only express an anti-derivative operation, as any constant of integration is the same as adding a constant to S, which has no physical implications as was previously discussed. The numbers ε_r and ε_θ are independent and both can be either 1 or -1. These come from the plus and minus sign ($\pm$) in the r and θ equations of motion (see (1.3.1) and (1.3.2)).

From the Hamilton-Jacobi formalism, the function S has n constants of integration with physical significance, which were named α_μ. For space-time $n = 4$, and so we must select four constants of integration to be our set α_μ. At this point the most natural choice is $\alpha_\mu = \{\mu^2, E, \Phi, Q\}$, although there are other possible choices which are equally valid. For instance, some authors use the constant $K = Q + (aE - \Phi)^2$ instead of Q (see [21]). For that matter any independent combination of these constants should do the job.

In section 1.2.3 it was described a general procedure to obtain a solution for a particle's motion: from initial values of x^μ and p_μ at $\lambda = \lambda_o$ we can obtain the constants α_μ; afterwords one could obtain the values of the β^μ constants of motion (more on that later) and then obtain x^μ as function of α_μ, β^μ and the affine parameter λ.

The initial conditions are then set by the values $\{t_o, r_o, \theta_o, \varphi_o\}$ and by $\{p_{t_o}, p_{r_o}, p_{\theta_o}, p_{\varphi_o}\}$ at $\lambda = \lambda_o$.

The equation $\partial S/\partial x^\mu = p_\mu$ explicitly becomes:

$$\frac{\partial S}{\partial t} = -E = p_t, \tag{1.3.5a}$$

$$\frac{\partial S}{\partial \varphi} = \Phi = p_\varphi, \tag{1.3.5b}$$

$$\frac{\partial S}{\partial r} = \varepsilon_r \frac{\sqrt{R}}{\Delta} = p_r, \tag{1.3.5c}$$

$$\frac{\partial S}{\partial \theta} = \varepsilon_\theta \sqrt{\Theta} = p_\theta. \tag{1.3.5d}$$

For $\lambda = \lambda_o$, the equations (1.3.5a) and (1.3.5b) directly give the values of E and Φ. Equations (1.3.5c) and (1.3.5d) both lead to:

$$R(r_o, E, \Phi, Q, \mu^2) = \Delta^2 p_{r_o}^2, \tag{1.3.6a}$$

$$\Theta(\theta_o, E, \Phi, Q, \mu^2) = p_{\theta_o}^2. \tag{1.3.6b}$$

From this set of two equations one can obtain the values of the constants Q and μ^2 as function of the initial coordinates x^μ_o and momenta p_{μ_o}. Explicitly these relations are given by:

$$\mu^2 = \frac{1}{\rho^2}\left\{\frac{P^2}{\Delta} - (aE - \Phi)^2 + a^2E^2\cos^2\theta_o - \frac{\Phi^2}{\tan^2\theta_o} - p_{\theta_o}^2 - \Delta\, p_{r_o}^2\right\}, \tag{1.3.7}$$

and also by[23]:

$$Q = p_{\theta_o}^2 - a^2E^2\cos^2\theta_o + \frac{\Phi^2}{\tan^2\theta_o} + (a^2\cos^2\theta_o)\mu^2, \tag{1.3.8}$$

with $P = E(r_o^2 + a^2) - a\Phi$ and $\Delta = r_o^2 + a^2 - 2mr_o$.

The set of constants of motion α_μ were thus determined by the initial conditions. However, the constants of motions used here are much more strongly linked to physical quantities (such as energy and angular momentum) than the conjugate momenta p_μ. Therefore it can be much more convenient to

---

[23] The value of μ is determined by the previous equation.

express the initial conditions by the constants of motion $\{\mu^2, E, \Phi, Q\}$ and by the initial coordinates $\{t_o, r_o, \theta_o, \varphi_o\}$ instead. Despite this fact, we can equally use the conjugate momenta as part of the initial conditions.

An interesting consequence of the Hamilton-Jacobi formalism is that the derivative of S with respect to the constant α_μ is also a constant of motion, here named β^μ:

$$\frac{\partial S}{\partial \alpha_\mu}(x^\mu; \alpha_\mu; \lambda) = \beta^\mu. \tag{1.3.9}$$

This equation explicitly becomes:

$$\begin{aligned}
\frac{\partial S}{\partial(\mu^2)} &= \beta^1, \\
\frac{\partial S}{\partial E} &= \beta^2, \\
\frac{\partial S}{\partial \Phi} &= \beta^3, \\
\frac{\partial S}{\partial Q} &= \beta^4.
\end{aligned}$$

This leads to [20, 22]:

$$\begin{aligned}
&\lambda = 2\beta^1 + \varepsilon_r \int^r \frac{r^2}{\sqrt{R}} dr + \varepsilon_\theta \int^\theta \frac{a^2 \cos^2\theta}{\sqrt{\Theta}} d\theta, \\
&t + \beta^2 = \varepsilon_r \int^r \frac{r^2(r^2+a^2)E + 2mar(aE - \Phi)}{\sqrt{R}} dr + \varepsilon_\theta \int^\theta \frac{a^2 E \cos^2\theta}{\sqrt{\Theta}} d\theta, \\
&\varphi = \beta^3 + \varepsilon_r \int^r \frac{r^2\Phi + 2mr(aE - \Phi)}{\Delta\sqrt{R}} dr + \varepsilon_\theta \int^\theta \frac{\Phi}{\tan^2\theta\,\sqrt{\Theta}} d\theta, \\
&2\beta^4 + \varepsilon_r \int^r \frac{dr}{\sqrt{R}} = \varepsilon_\theta \int^\theta \frac{d\theta}{\sqrt{\Theta}}.
\end{aligned}$$

It is now possible to determine the values of the constants $\{\beta^1, \beta^2, \beta^3, \beta^4\}$ for the initial conditions $\{t_o, r_o, \theta_o, \varphi_o\}$ at $\lambda = \lambda_o$, assuming that the constants $\{\mu^2, E, \Phi, Q\}$ are already known. These indefinite integrals are defined up to a constant of integration and so there are different possible choices for this functions. All these choices are all equally valid, as long as the constants β^μ are adjusted accordingly. Also, the numbers ε_r and ε_θ only change signal at turning points, namely for $\dot{r} = 0$ and $\dot{\theta} = 0$ respectively.

These integral expressions are a set of four equations with four variables $\{t, r, \theta, \varphi\}$ and so it defines implicitly the geodesic trajectory. It is therefore a solution in integral form [20]. However, the last step in section 1.2.3, which is to “turn the equation inside out” is not trivial in this case, although it could be done in principle. Notice also that each integral does not have mixed coordinates, since each depends either on θ or on r, which eases the use of numerical techniques.

If the choice of constants α_μ was different, the final set of integral equations would also be different due to the differentiation (1.3.9). For instance, in the reference [21] the authors choose $K = Q + (aE - \Phi)^2$ instead of Q and as consequence the final form of the solution is not the same as here. However different choices can describe the same geodesic motion since in that case the constants β^μ would have to be different.

1.4 Spherical photon orbits for Kerr

We now focus on photon geodesics with constant radial coordinate[24]. These are called spherical photon orbits and exhibit some interesting properties. For short, in the following text the **name “orbits” is only assigned to geodesics with constant radial coordinate.**

Photons have zero rest mass ($\mu = 0$) and follow null geodesics. The r and θ equations of motion then become (see (1.3.1)(1.3.2)):

$$\rho^4\dot{\theta}^2 = \Theta(\theta) = Q - \cos^2\theta\left(\frac{\Phi^2}{\sin^2\theta} - a^2E^2\right),$$

$$\rho^4\dot{r}^2 = R(r) = P^2 - \Delta[Q + (aE - \Phi)^2],$$

with $P = E(r^2 + a^2) - a\Phi$. We reduce the number of parameters [22, 23] by defining the impact factors[25]:

$$\boxed{\lambda = \frac{\Phi}{E}} \qquad \text{and} \qquad \boxed{\eta = \frac{Q}{E^2}}, \tag{1.4.1}$$

and dividing each equation of motion by E^2.

For r we have:

$$\left(\frac{\rho^4}{E^2}\right)\dot{r}^2 = \frac{R(r)}{E^2} = \left((r^2 + a^2) - a\lambda\right)^2 - (\eta + (a - \lambda)^2)(r^2 + a^2 - 2mr)$$

---

[24] The discussion below is strongly based on Edward Teo’s article [23].

[25] In this context the symbol λ does not stand for the affine parameter. Unless otherwise mentioned λ is now assumed to be defined by (1.4.1)

$$= (r^2+a^2)^2+a^2\lambda^2-2a\lambda(r^2+a^2)-\eta(r^2+a^2)-(a^2+\lambda^2-2a\lambda)(r^2+a^2)+2mr[\eta+(a-\lambda)^2]$$
$$= r^4+a^4+2r^2a^2+a^2\lambda^2-\eta(r^2+a^2)-(a^2+\lambda^2)r^2-(a^2+\lambda^2)a^2+2mr[\eta+(a-\lambda)^2].$$

So we get:

$$\boxed{\frac{R(r)}{E^2} \equiv \mathcal{R}(r) = r^4 + (a^2-\eta-\lambda^2)r^2 + 2m[\eta+(a-\lambda)^2]r - \eta a^2.} \tag{1.4.2}$$

For the θ equation, defining:

$$u \equiv \cos\theta,$$

we get:

$$\dot{u} = -\dot{\theta}\sin\theta \qquad \text{and} \qquad \sin^2\theta = 1-u^2;$$

so we have:

$$\frac{\Theta}{E^2} = \left(\frac{\rho^4}{E^2\sin^2\theta}\right)\dot{u}^2 = \eta - \cos^2\theta\left(\frac{\lambda^2}{\sin^2\theta} - a^2\right),$$

$$\left(\frac{\rho^4}{E^2}\right)\dot{u}^2 = \eta[1-u^2] - u^2(\lambda^2 - a^2[1-u^2]),$$

which leads to:

$$\boxed{\left(\frac{\rho^4}{E^2}\right)\dot{u}^2 = -a^2u^4 - [\eta+\lambda^2-a^2]u^2 + \eta \equiv \Xi(u).} \tag{1.4.3}$$

Notice that $\Xi(u) \geq 0$ for real values of $\dot{u}$ and also that:

$$\Xi = \frac{\sin^2\theta}{E^2}\Theta.$$

1.4.1 Motion in latitude (θ)

We now consider separately three different cases $\eta > 0$, $\eta < 0$ and $\eta = 0$.

For $\boxed{\eta > 0}$:

The zeros of the equation $\Xi(u) = 0$ are:

$$u_o^2 = \frac{[a^2-\eta-\lambda^2] \pm \sqrt{[a^2-\eta-\lambda^2]^2 + 4a^2\eta}}{2a^2}. \tag{1.4.4}$$

Because $\eta > 0$ we must necessarily have that the discriminant

$$D = [a^2-\eta-\lambda^2]^2 + 4a^2\eta$$

obeys:

$$\sqrt{D} > |a^2 - \eta - \lambda^2|.$$

Therefore, the root associated with the plus sign in (1.4.4) is always positive and the root with minus sign in (1.4.4) is always negative.
Because $u_o^2 \geq 0$ only the positive root is meaningful:

$$\boxed{u_o^2 = \frac{[a^2 - \eta - \lambda^2] + \sqrt{[a^2 - \eta - \lambda^2]^2 + 4a^2\eta}}{2a^2}.} \tag{1.4.5}$$

For the allowed range $0 \leq |u| \leq 1$ the function $\Xi(u)$ has then only one zero. In the limits of this interval:

$$\Xi_{(u=1)} = -\lambda^2,$$

$$\Xi_{(u=0)} = \eta.$$

Because only $\Xi \geq 0$ is physically allowed, we conclude that orbits with $\eta > 0$ cross the equatorial plane repeatedly ($u = 0 \iff \theta = \pi/2$) and are restricted to the interval $0 \leq |u| \leq |u_o|$ (see Fig. 1.4.1). The points of intersection in the equatorial plane are called **nodes**.
For $\boxed{\eta < 0}$:

From (1.4.3) we must have:

$$\eta + \lambda^2 - a^2 < 0, \tag{1.4.6}$$

so there can be a value $u \neq 0$ such that Ξ is non negative. For spherical photon orbits this is an impossible requirement. As it is proven in Appendix A.3, these orbits are always required to have $\eta + \lambda^2 - a^2 > 0$ for $r > r_+$. However condition (1.4.6) can be met for other types of geodesics.

For $\boxed{\eta = 0}$:

The roots of $\Xi(u)$ are now:

$$u_o^2 = \frac{a^2 - \lambda^2 \pm |\lambda^2 - a^2|}{2a^2},$$

this leads to:

$$u_o^2 = 0 \qquad \text{or} \qquad u_o^2 = \frac{a^2 - \lambda^2}{a^2} = 1 - \frac{\lambda^2}{a^2}. \tag{1.4.7}$$

As it is proven in Appendix A.3, for $\eta = 0$ we have $\lambda^2 > a^2$ for spherical orbits and so $1 - \lambda^2/a^2 < 0$. Therefore, of the two roots in (1.4.7) only $u_o^2 = 0$

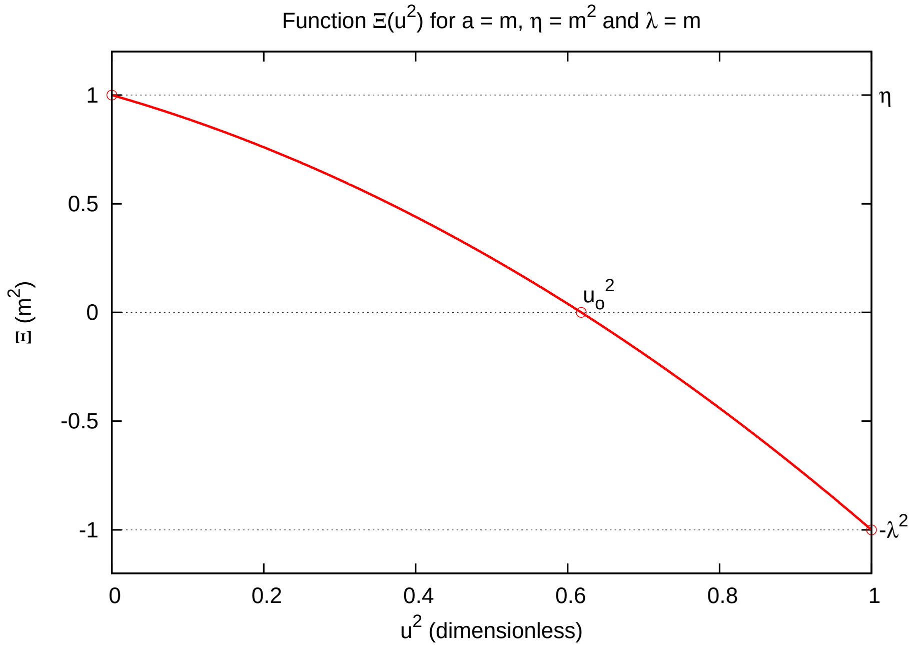

Figure 1.4.1: Graph of $\Xi(u^2)$ for $a = m$, $\eta = m^2$ and $\lambda = m$. The values of Ξ for $u = 0$ and $u^2 = 1$ are respectively η and $-\lambda^2$. The root of Ξ is given by u_o^2 and it is clear from the graph that $\eta > 0$ and $\lambda \neq 0$ implies $0 < u_o^2 < 1$. Notice however that the allowed range for the photon is $0 \leq |u| \leq |u_o|$.

is relevant for orbits. From the Fig. 1.4.1 is clear that $\eta = 0 \implies u_o = 0$ and that the orbit is restricted to the equatorial plane ($u = 0$).

We conclude that for spherical orbits we must have $\eta \geq 0$ and there is only one allowed value $|u| = |u_o|$ in the interval $0 \leq u^2 \leq 1$, such that $\Xi(u) = 0$. The orbits are therefore either restricted to the equatorial plane or cross it repeatedly [17].
Only for the case $\lambda = 0 \implies |u_o| = 1$ and $\eta > 0$ can the photon reach the poles ($\theta = 0$ or $\theta = \pi$), that is when the angular momentum $\Phi = 0$.

1.4.2 Radial motion (r)

The conditions for spherical orbits, which are geodesics with constant radial coordinate r, are:

$$\dot{r} = 0 \qquad \text{and} \qquad \ddot{r} = 0,$$

which only state, in analogy with Newtonian physics, that the "velocity" and "acceleration" are both zero in the radial component. These conditions do not make any assumptions or restrictions regarding the stability of the orbits.

From (1.4.2) is clear the equivalence of the conditions:

$$\dot{r} = 0 \iff \mathcal{R} = 0,$$

as we have:

$$\frac{\rho^4 \dot{r}^2}{E^2} = \mathcal{R}(r).$$

Differentiation with respect to the affine parameter yields:

$$\frac{2\rho^4 \dot{r}}{E^2}\ddot{r} + \frac{4\rho^3 \dot{\rho}}{E^2}\dot{r}^2 = \dot{r}\frac{d\mathcal{R}}{dr}.$$

Dividing by $\dot{r}$:

$$\frac{2\rho^4}{E^2}\ddot{r} + \frac{4\rho^3 \dot{\rho}}{E^2}\dot{r} = \frac{d\mathcal{R}}{dr}.$$

In the limit $\dot{r} \to 0$:

$$\frac{2\rho^4}{E^2}\ddot{r} = \frac{d\mathcal{R}}{dr}.$$

Therefore for $\dot{r} = 0$:

$$\ddot{r} = 0 \iff \frac{d\mathcal{R}}{dr} = 0.$$

The conditions for spherical orbits [17, 22] are therefore also given by :

$$\boxed{\mathcal{R} = 0 \qquad \text{and} \qquad \frac{d\mathcal{R}}{dr} = 0.} \tag{1.4.8}$$

The solution to this set of equations is given by two roots of a quadratic equation (see Appendix A.2 for full calculations). Each of those two roots leads to a different class of solutions, i) and ii) for spherical orbits:

$$\left.\begin{aligned} \lambda &= \frac{r^2 + a^2}{a}, \\ \eta &= -\frac{r^4}{a^2}; \end{aligned}\right\} \quad \text{i)} \tag{1.4.9}$$

$$\left.\begin{aligned} \lambda &= -\frac{r^3 - 3mr^2 + a^2 r + ma^2}{a(r-m)}, \\ \eta &= -\frac{r^3(r^3 - 6mr^2 + 9m^2 r - 4a^2 m)}{a^2(r-m)^2}. \end{aligned}\right\} \quad \text{ii)} \tag{1.4.10}$$

It is important to notice that λ and η are here depicted as functions of the orbital radius r; however, given a photon following a geodesic, $\{\lambda, \eta\}$ are constants of motion and do not depend on the coordinate r. Equations (1.4.9) and (1.4.10) simply state the necessary values of λ and η for the geodesic

motion to be a spherical orbit of radius r. These orbits are all unstable[26], as assured by the "No Bound Theorem" proven in Appendix A.5.
As discussed previously, $\eta < 0$ is impossible for orbits, so class i) is automatically excluded for being unphysical.

For class ii), the condition $\eta \geq 0$ restricts the range of the radial coordinate to $r_1 \leq r \leq r_2$, where r_1 and r_2 are the roots[27] of η (see Appendix A.4 for deduction):

$$r_1 = 2m \left\{ 1 + \cos \left(\frac{2}{3} \arccos \left[-\frac{|a|}{m} \right] \right) \right\}, \tag{1.4.11}$$

$$r_2 = 2m \left\{ 1 + \cos \left(\frac{2}{3} \arccos \left[\frac{|a|}{m} \right] \right) \right\}. \tag{1.4.12}$$

It turns out that r_1 is associated to a prograde orbit and r_2 to a retrograde orbit (see Fig. 1.4.2) [23].
The radius r_3 is also defined as the root of $\lambda(r)$ and corresponds to an orbit with zero angular momentum, $\Phi = 0$ (see (1.4.1)). It can be computed as (see Appendix A.4 and [23]):

$$r_3 = m \left\{ 1 + 2\sqrt{m^2 - \frac{1}{3}a^2} \cos \left(\frac{1}{3} \arccos \frac{m(m^2 - a^2)}{\left(m^2 - \frac{1}{3}a^2\right)^{3/2}} \right) \right\}.$$

Notice that $r_1 \leq r_3 \leq r_2$, as one can observe from Fig. 1.4.2.

For $a = 0$ we obtain $r_1 = r_2 = 3m$ as expected for the Schwarzschild space-time [24] (see Fig. 1.4.2).
For $a = 1$ we have $r_1 = m$ and $r_2 = 4m$. Although r_1 appears in this case to coincide with the event horizon r_+, there is a non-zero proper distance between r_1 and r_+ (see [22]).

For $r = r_1$ or $r = r_2$, we have $\eta = 0$ and so by the previous discussion in subsection (1.4.1) the motion is restricted to the equatorial plane[28].

---

[26] This could also be checked by realizing that $\frac{d^2\mathcal{R}}{dr^2} > 0$ [17].

[27] A curious exception occurs for the extremal case $|a| = m$, since for this case $\eta_{(r_1=m)}$ is not well defined (indeterminate form of type 0/0) and the limit of $\eta(r)$ as $r \to r_1 = m$ is not zero but the constant value $3m^2$.

[28] This orbit is stable to perturbations in θ but never in r as it is show in Appendix A.5.

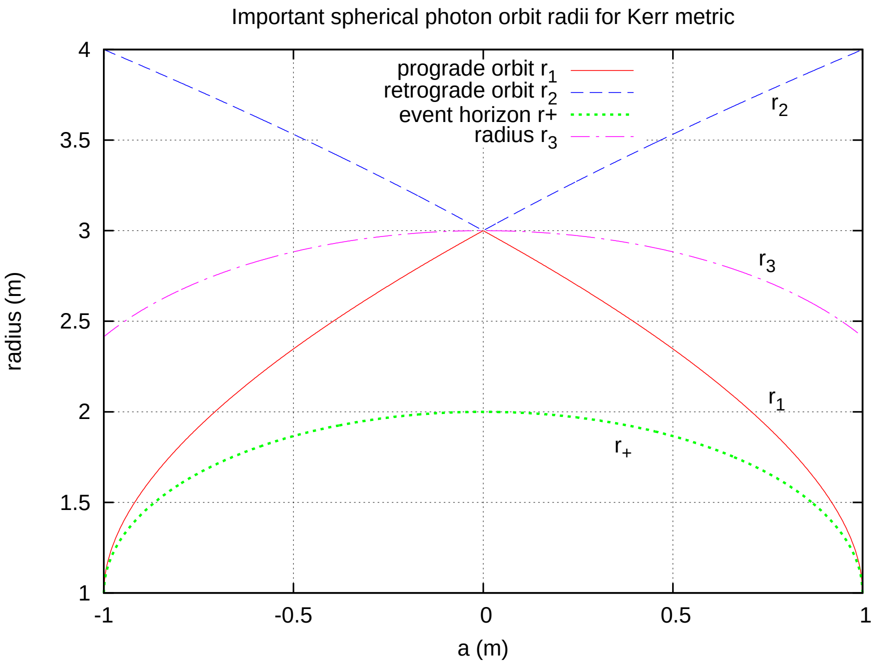

Figure 1.4.2: Plot of the values of the orbital radii r_1, r_2 and r_3 for different values of the rotation parameter a. The radius of the event horizon is also represented for reference. The orbits with $r = r_1$ and $r = r_2$ are respectively associated with prograde and retrograde geodesics and r_3 with zero angular momentum orbits ($\Phi = 0$), which implies $\lambda = 0$ (see Fig. 1.4.3 and equation (1.4.1)). Notice that for $a = 0$ we have the Schwarzschild case $r_1 = r_2 = 3m$ and $r_+ = 2m$. From this plot is easy to realize that we have $r_+ \leq r_1 \leq r_3 \leq r_2$.

1.4.3 Some properties of η and λ

The typical form of the functions $\lambda(r)$ and $\eta(r)$ are depicted in Fig. 1.4.3. The maximum value of η in the range $r_1 \leq r \leq r_2$ is always $27m^2$ at $r = 3m$, independently of the value of $a \neq 0$. In fact we have:

$$\eta_{(r=3m)} = 27m^2\frac{\cancel{4ma^2}}{\cancel{4ma^2}} = 27m^2.$$

The derivative $d\eta/dr$ is easily computed:

$$\frac{d\eta}{dr} = \frac{r^2(-4r^4 + 24r^3 - 48m^2r^2 + 4a^2mr + 36m^3r - 12a^2m^2)}{a^2(r-m)^3}.$$

For $r = 3m$ this yields

$$\frac{d\eta}{dr}(r = 3m) = 0$$

The value of η is closely related to the θ-velocity when the photon crosses

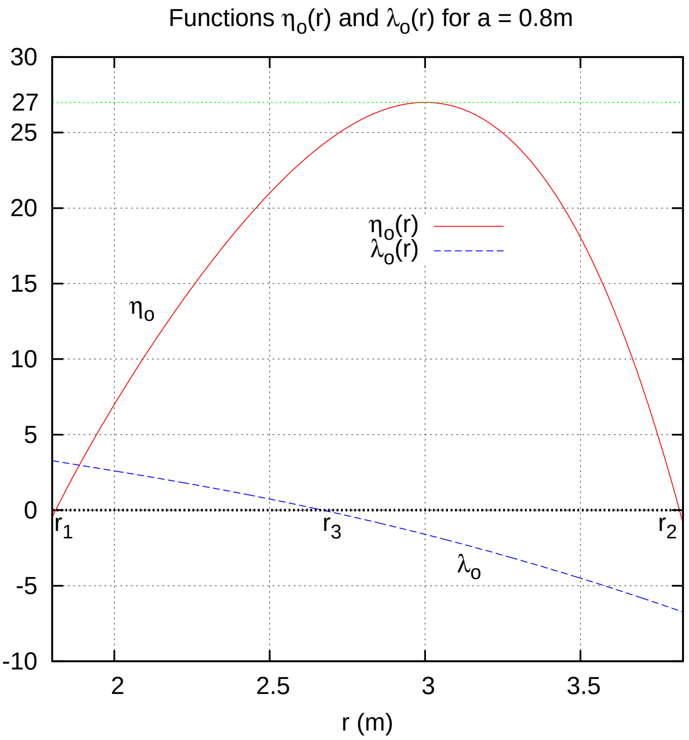

Figure 1.4.3: Plot of the dimensionless functions $\eta_o(r) = \eta(r)/m^2$ and $\lambda_o(r) = \lambda(r)/m$ (see (1.4.10)) as function of the orbital radius r, for the rotation parameter $a = 0.8m$. Notice the maximum of η at $r = 3m$ with value $27m^2$. From this graph it is clear that $\eta(r_1) = \eta(r_2) = \lambda(r_3) = 0$ and also that $\lambda(r_1) > 0$ and $\lambda(r_2) < 0$.

the equatorial plane ($u = 0$) (see (1.4.3)). The value $27m^2$ is the maximum because for $r = 3m$ we have $\dot{\varphi} = 0$ in the equatorial plane (photon crosses the equatorial plane vertically [23]):

$$\lambda_{(r=3m)} = -2a.$$

From (1.3.4):

$$\frac{\Delta\,\rho^2}{E}\dot{\varphi}_{(r=3m)} = 2mar + \lambda(\Delta - a^2) = 0.$$

The value of λ monotonically decreases [23] from a positive value $\lambda_{(r=r_1)}$ to a negative value at $\lambda_{(r=r_2)}$. Because λ is proportional to Φ (see (1.4.1)) we conclude that r_1 and r_2 are associated with a prograde and retrograde orbit respectively.

1.4.4 Connection between θ and φ motions

The analysis of the relation between θ and φ motions have some interesting features (see also [25]). The equation (1.3.4) is repeated for convenience:

$$\Delta\,\rho^2\dot{\varphi} = 2mrEa + \frac{\Phi(\Delta - a^2\sin^2\theta)}{\sin^2\theta}.$$

Defining the new variable:

$$z \equiv u^2 = \cos^2\theta,$$

with derivative $\dot{z} = 2u\dot{u}$, we obtain:

$$\dot{\varphi} = \frac{2mraE}{\Delta\,\rho^2} + \frac{\Phi\,(\Delta - a^2(1-z))}{\Delta\rho^2(1-z)} = \frac{2mraE - a^2\Phi}{\Delta\,\rho^2} + \frac{\Phi}{\rho^2(1-z)}.$$

In the new variable, the latitude equation (1.4.3) becomes:

$$\frac{\rho^4\dot{u}^2}{E^2} = \Xi(u) \longrightarrow \frac{\rho^4}{E^2}\frac{\dot{z}^2}{4z} = \Xi(u).$$

We get an equation[29] for $\dot{z}$:

$$\dot{z} = \frac{2E}{\rho^2}\underbrace{\sqrt{z\,\Xi}}_{Y(z)},$$

which combined with the expression for $\dot{\varphi}$ leads to the derivative:

$$\frac{d\varphi}{dz} = \frac{1}{2}\frac{(2mra - a^2\lambda)}{\Delta\,Y(z)} + \frac{\lambda/2}{Y(z)(1-z)}. \tag{1.4.13}$$

The expression for $Y^2(z)$ is:

$$Y^2(z) = z\Xi = z\left(-a^2z^2 - (\eta + \lambda^2 - a^2)z + \eta\right) = -a^2z^3 - (\eta+\lambda^2-a^2)z^2 + \eta z.$$

The roots of $Y^2(z)$ are then[30]:

$$z = 0 \qquad \text{or} \qquad z_\pm = \frac{(a^2 - \eta - \lambda^2) \pm \sqrt{(a^2 - \eta - \lambda^2)^2 + 4a^2\eta}}{2a^2}.$$

Therefore $Y^2(z)$ can be factorized in the following form:

$$\boxed{Y^2(z) = a^2z(z_+ - z)(z - z_-).} \tag{1.4.14}$$

For spherical photon orbits we have $a^2 - \eta - \lambda^2 < 0$ (see Appendix A.3) and $\eta \geq 0$ (for $\dot{\theta}$ to be real). As such, z_- is always negative and z_+ is always positive or zero. From its definition $z \geq 0$, and so the root z_- is excluded for spherical orbits.

---

[29] A positive root for the square root is assumed, however this does not affect our conclusions.

[30] Observation: $z_+ = u_o^2$ (see page 26)

Because $\Xi = 0$ gives the turning points in latitude, we conclude that the range of z is:

$$0 \leq z \leq z_+.$$

For 1/4 oscillation in latitude, the azimuthal variation[31] is $\Delta\varphi'$:

$$\Delta\varphi' = \frac{1}{2}\frac{2mra - a^2\lambda}{\Delta}\int_0^{z_+}\frac{dz}{Y(z)} + \frac{1}{2}\lambda\int_0^{z_+}\frac{dz}{Y(z)(1-z)}. \tag{1.4.15}$$

For a full oscillation in latitude the azimuthal variation is simply $\Delta\varphi = 4\Delta\varphi'$, as the equation (1.3.4) is invariant by the transformations:

$$\dot{\theta} \to -\dot{\theta} \qquad \text{and} \qquad \theta \to \pi - \theta,$$

and so we get the same change $\Delta\varphi'$ in each 1/4 latitude oscillation [17].

Changing the integration variable by the transformation:

$$z = z_+\cos^2 x \qquad \text{with} \qquad dz = -2z_+\cos x\sin x\, dx,$$

one of the relevant integrals in (1.4.15) becomes:

$$\begin{aligned}
\int_0^{z_+}\frac{dz}{Y(z)} &= \int_{\frac{\pi}{2}}^{0}\left(\frac{-2z_+\cos x\sin x}{a\cos x\sqrt{z_+}\sqrt{(z_+ - z_+\cos^2 x)}\sqrt{(z_+\cos^2 x - z_-)}}\right)dx \\
&= \int_0^{\frac{\pi}{2}}\left(\frac{2\sin x}{a\sin x\sqrt{(z_+ - z_- - z_+\sin^2 x)}}\right)dx \\
&= \int_0^{\frac{\pi}{2}}\left(\frac{2}{a\sqrt{z_+ - z_-}\sqrt{\frac{z_+ - z_- - z_+\sin^2 x}{z_+ - z_-}}}\right)dx \\
&= \frac{2}{a\sqrt{z_+ - z_-}}\int_0^{\frac{\pi}{2}}\frac{dx}{\sqrt{1-k^2\sin^2 x}},
\end{aligned}$$

where $k = \sqrt{\frac{z_+}{z_+ - z_-}}$. This expression can be rewritten as:

$$\int_0^{z_+}\frac{dz}{Y(z)} = \frac{2\,\mathcal{K}(k)}{a\sqrt{z_+ - z_-}}, \tag{1.4.16}$$

where $\mathcal{K}(k)$ is the complete elliptic integral of the first kind [26].
For the second integral in (1.4.15):

$$\int_0^{z_+}\frac{dz}{Y(z)(1-z)} = \frac{2}{a\sqrt{z_+ - z_-}}\int_0^{\frac{\pi}{2}}\frac{dx}{(1 - z_+\cos^2 x)\sqrt{1-k^2\sin^2 x}}.$$

---

[31] In this context $\Delta\varphi$ stands for variation in the coordinate φ.

The term $1 - z_+^2 \cos^2 x$ can be rewritten as:

$$1 - z_+^2 \cos^2 x = 1 - z_+ + z_+ \sin^2 x = (1 - z_+) \left(1 - \underbrace{\left(\frac{z_+}{z_+ - 1} \right)}_{n} \sin^2 x \right).$$

So we have:

$$\int_0^{z_+} \frac{dz}{Y(z)(1-z)} = \frac{2}{a(1-z_+)\sqrt{z_+ - z_-}} \int_0^{\frac{\pi}{2}} \frac{dx}{(1 - n\sin^2 x)\sqrt{1 - k^2 \sin^2 x}}.$$

This expression can be rewritten as:

$$\int_0^{z_+} \frac{dz}{Y(z)(1-z)} = \frac{2\,\Pi(n,k)}{a(1-z_+)\sqrt{z_+ - z_-}}, \qquad (1.4.17)$$

where a complete elliptic integral of the third kind $\Pi(n,k)$ was used[32] in the last equation [26].

Combining equations (1.4.15 - 1.4.16) we obtain the azimuthal change over a complete[33] oscillation in θ:

$$\Delta\varphi = \frac{4}{\sqrt{z_+ - z_-}} \left(\frac{(2mr - a\lambda)\mathcal{K}(k)}{\Delta} + \frac{\lambda\,\Pi(n,k)}{a(1-z_+)} \right), \qquad (1.4.18)$$

with $n = \frac{z_+}{z_+ - 1}$ and $k^2 = \frac{z_+}{z_+ - z_-}$.

The graph of $\Delta\varphi$ as function of the orbit radius is given in Fig. 1.4.4. Notice the discontinuity at $r = r_3$, where by definition $\lambda = 0$ (see [17, 23]). The value of $\Delta\varphi$ at exactly $r = r_3$ is only due to frame dragging, as for that case $\Phi = 0$. That value is defined to be:

$$\Delta\varphi_{(r=r_3)} \equiv \Delta\varphi^0.$$

The following limits are also defined as:

$$\lim_{r \to r_3^-} \Delta\varphi \equiv \Delta\varphi^+,$$

---

[32] Sometimes a different convention for $\Pi(n,k)$ is used, corresponding to a transformation $n \to -n$.

[33] If the oscillation is not complete but between z_+ and z, the expression (1.4.18) can be written in a similar way but with incomplete elliptic integrals rather than complete ones: the x integration variable would be in that case between 0 and an angle ψ such that $\cos^2\psi = z/z_+$. Only for a complete oscillation in θ where the photon reaches the equator ($z = 0$) is $\psi = \pi/2$.

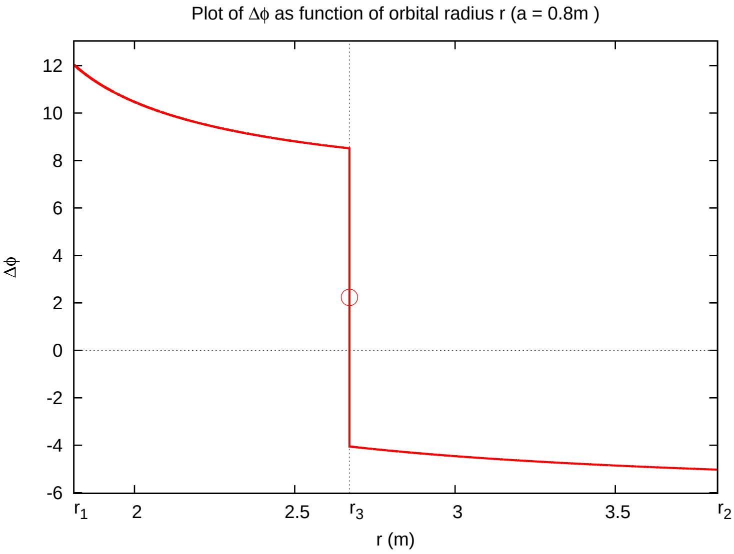

Figure 1.4.4: Plot of the azimuthal change $\Delta\varphi$ over a complete oscillation in θ, as function of the orbital radius r and for the rotation parameter $a = 0.8m$. Notice the discontinuity at $r = r_3$, point for which $\lambda = \Phi = 0$. The value of $\Delta\varphi$ at exactly $r = r_3$ is given by the circular point in the figure, which is exactly half-way between the upper and lower limits by a value of 2π.

$$\lim_{r\to r_3^+} \Delta\varphi \equiv \Delta\varphi^- .$$

As one can observe from Fig. 1.4.4, we have $\Delta\varphi^+ > 0$, $\Delta\varphi^0 > 0$ and $\Delta\varphi^- < 0$. The azimuthal variation $\Delta\varphi$ has therefore always the same sign of the angular momentum Φ (see [17]) (except for exactly $\Phi = 0$).
Defining the ratio f of frequencies of oscillation[34] in θ and φ as:

$$f \equiv \frac{\nu_\varphi}{\nu_\theta} = \frac{|\Delta\varphi|}{2\pi},$$

we have in the limit $r \to r_3$:

$$\Delta\varphi > 0 \longrightarrow 2\pi f^+ \equiv \Delta\varphi^+ ,$$

$$\Delta\varphi < 0 \longrightarrow 2\pi f^- \equiv -\Delta\varphi^- .$$

The angle of advance of the nodes for $\Phi \neq 0$, after each full oscillation in θ, is given by:

$$\Delta\Omega = 2\pi |f - 1| .$$

---

[34] This frequency f is also not continuous in r.

This angle is a continuous function of the orbit radius, as one can see from Fig. 1.4.5. For $\Phi = 0$ we must have $\Delta\varphi^0 = \Delta\Omega$ as for that case only frame-dragging is responsible for a change in the azimuthal coordinate φ. Since $\Delta\Omega$ is a continuous function we conclude that in the limit $r \to r_3$:

$$\begin{aligned} \Delta\varphi^0 &= \lim_{r\to r_3} \Delta\Omega \tag{1.4.19}\\ &= 2\pi(f^+ - 1) \tag{1.4.20}\\ &= 2\pi(1 - f^-), \tag{1.4.21} \end{aligned}$$

which leads to:

$$\Delta\varphi^+ - \Delta\varphi^- = 4\pi,$$

$$\Delta\varphi^0 = \Delta\varphi^+ - 2\pi \qquad \text{and} \qquad \Delta\varphi^0 = \Delta\varphi^- + 2\pi.$$

At the discontinuity in $\Delta\varphi$, the difference between the left and right limits

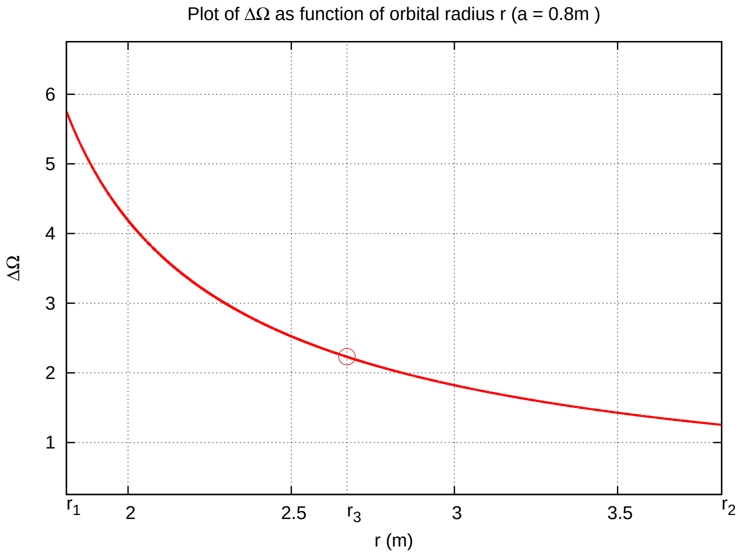

Figure 1.4.5: Plot of the angle of advance of the nodes $\Delta\Omega$ as function of the coordinate radius r and for the rotation parameter $a = 0.8m$. Notice that $\Delta\Omega$ is continuous at $r = r_3$ and that the circular point is the same as in Fig. 1.4.4.

(Fig. 1.4.5) is therefore always equal to 4π and the value $\Delta\varphi_{(r=r_3)}$ is always half-way between those two values [23].

1.4.5 Examples of spherical orbits

In this subsection a few interesting examples of spherical photon orbits[35] are presented. The orbits were obtained by numerical integration of the first-order differential equations of motion (1.3.1 - 1.3.4). A standard fourth-order Runge-Kutta algorithm was used for this purpose [27], implemented in a C++ code. The integration step used for the affine parameter was small enough such that the numerical value of u_o (see (1.4.5)) was correct up to five decimal places.

Orbits were analysed for special cases of the radial coordinate r around a BH with spin $a_o = 0.8$ and $a_o = 0.01$ (see Fig. 1.4.6 up to Fig. 1.4.9). For each set $\{r, \theta, \varphi\}$ of Boyer-Lindquist coordinates it was assigned a point in Cartesian space as if they were spherical coordinates. The impact parameters λ and η used (see (1.4.1)) are given by (1.4.10), as required for spherical photon orbits. For simplicity the value of E/m was set to one; this is hardly very significant since according to the equations of motion (1.3.1 - 1.3.4) a different value of E would just lead to a rescaling of the affine parameter. The variation of the latter along the orbit was either 150 or 300; notice that the affine parameter is a dimensionless quantity (see page 10). The initial position was always set at $\theta = \pi/2$ and $\varphi = 0$ (r was constant for each numerical simulation).

---

[35] See Teo's article [23] for a more complete discussion.

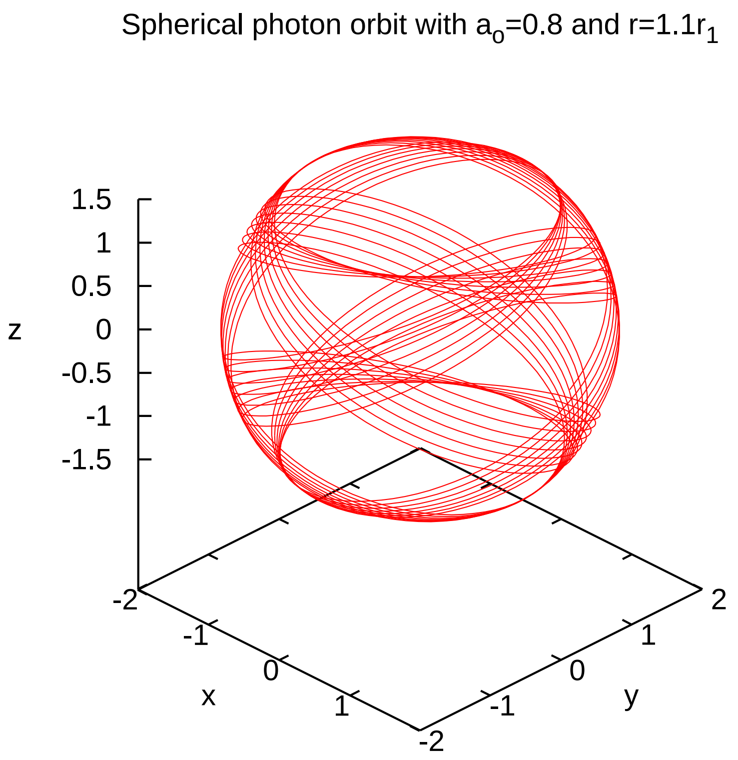
Spherical photon orbit with a_o=0.8 and r=1.1r_1

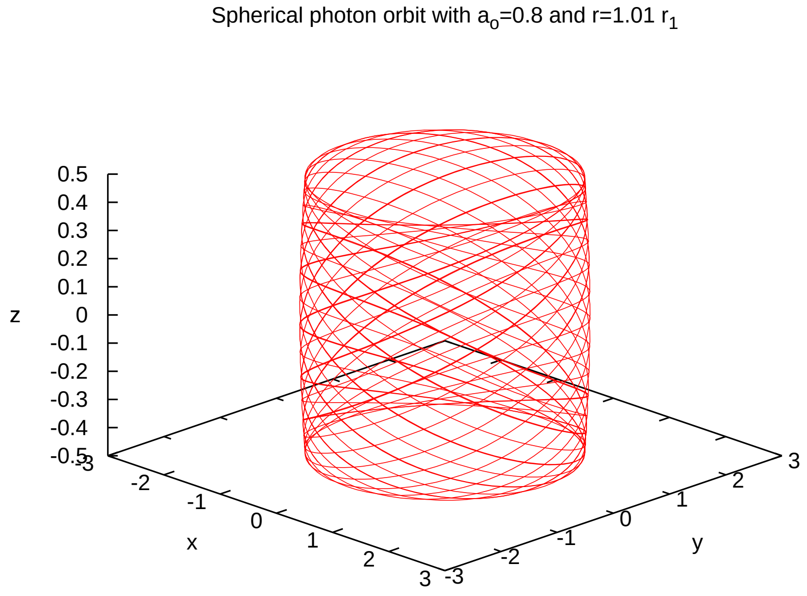
Spherical photon orbit with a_o=0.8 and r=1.01 r_1

Figure 1.4.6: Representations in Cartesian space of a single spherical photon orbit. All BHs have $a = 0.8m$; the variation of the affine parameter along the orbit was 150. (*Top*): $r = 1.1\, r_1$ (*Bottom*): $r = 1.01\, r_1$; notice that because $r \simeq r_1$ the orbit is almost in the BH equatorial plane, as the scale in the z axis suggests.

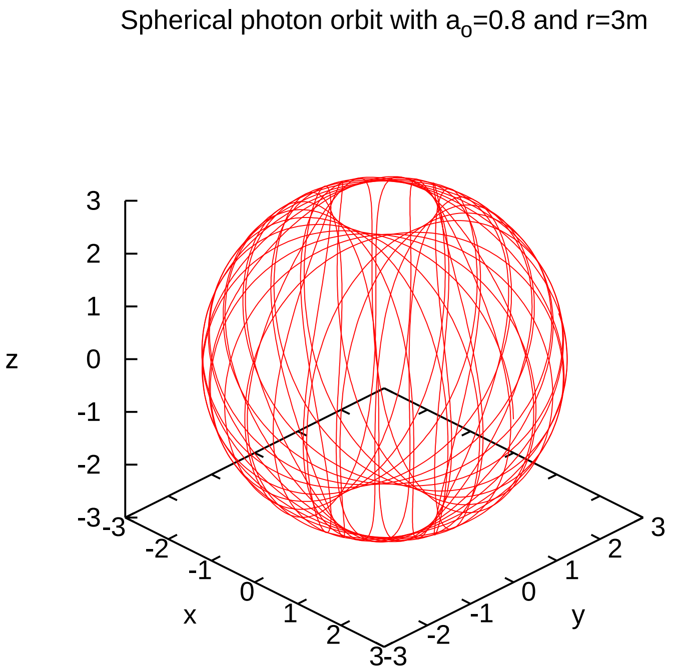

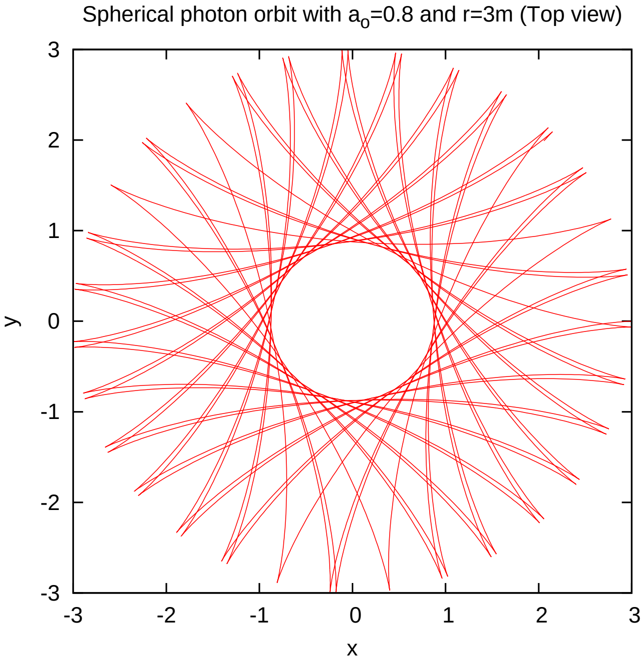

Figure 1.4.7: Representations in Cartesian space of a single spherical photon orbit with $a = 0.8m$ and $r = 3m$ for both images; the variation of the affine parameter along the orbit was 300 also for both. (*Top*): For $r = 3m$ the constant Q is a maximum and the photon crosses the equatorial plane perpendicularly (in the equatorial plane $\dot{\varphi} = 0$). Notice that there is a latitude range which cannot be reached by the photon. (*Bottom*): Top view (z axis) of the orbit in the top figure. The sharp edges are a consequence of $\dot{\varphi} = 0$ in the equatorial plane.

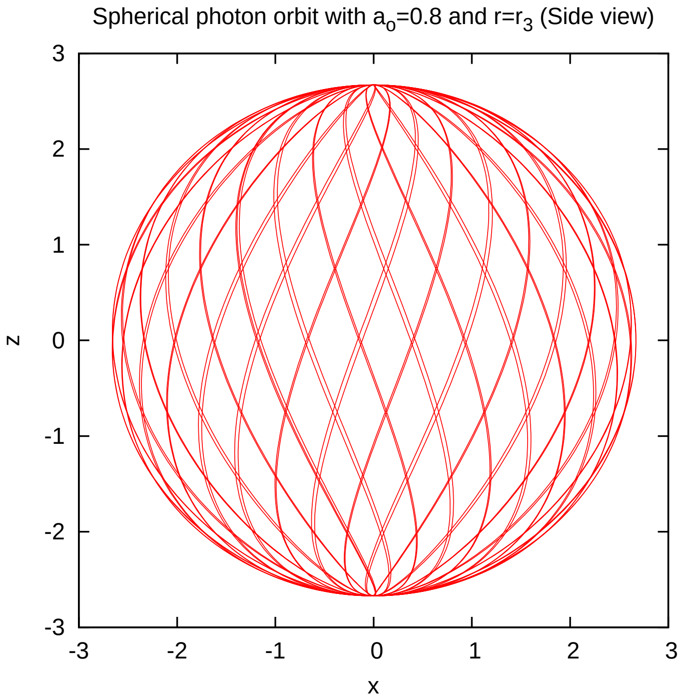

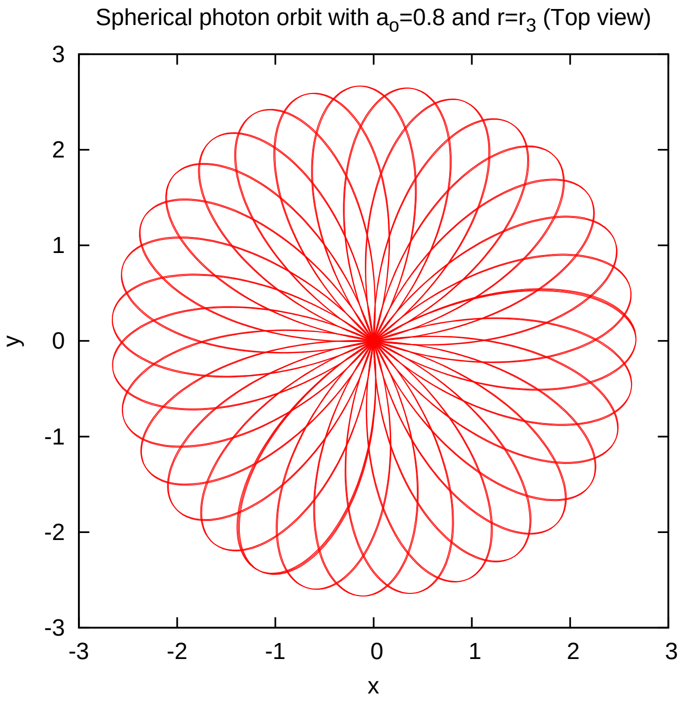

Figure 1.4.8: Representations in Cartesian space of a single spherical photon orbit with $a = 0.8m$ and $r = r_3$ for both images; the variation of the affine parameter along the orbit was 300 also for both. (*Top*): A side view (y axis) of the orbit is here used. For $r = r_3$ the axial angular momentum Φ is zero. Notice that the photon crosses the equatorial plane with $\dot{\varphi} \neq 0$ due to frame dragging. (*Bottom*): Top view (z axis) of the orbit in the top figure. Due to the fact that $\Phi = 0$ for $r = r_3$ the photon can reach the poles (compare with Fig. 1.4.7 bottom).

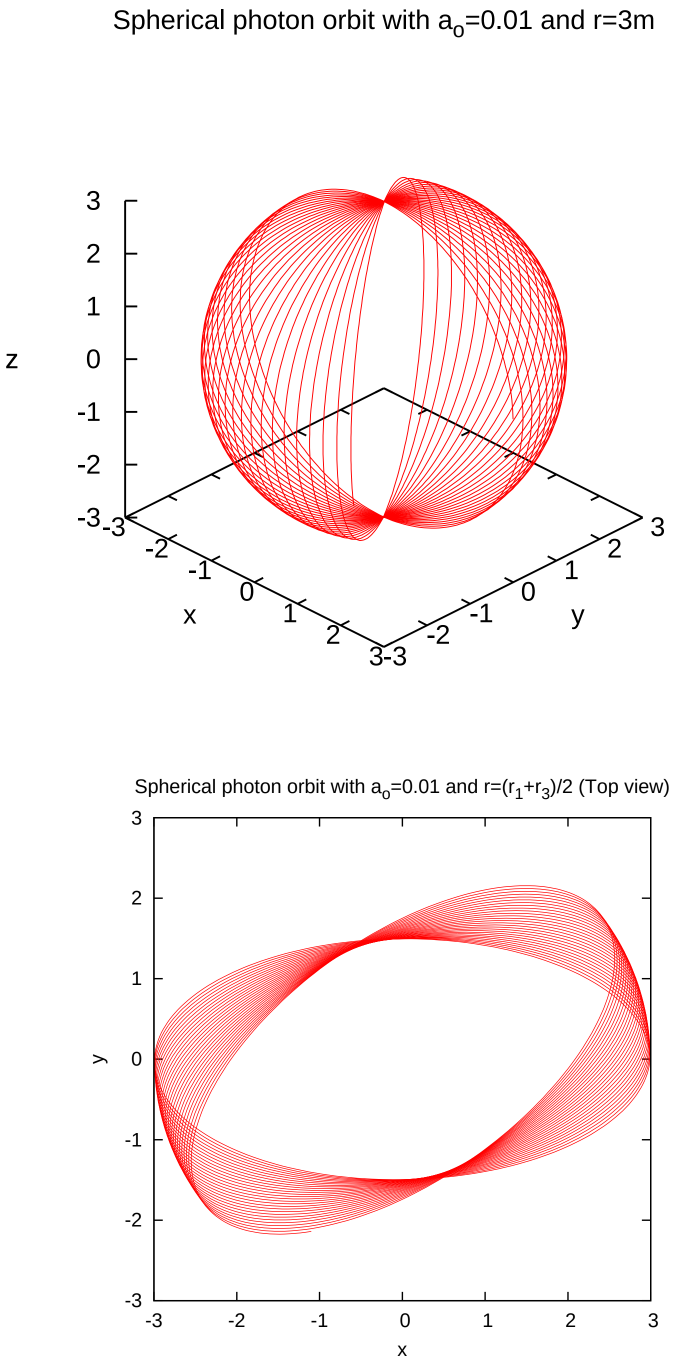

Spherical photon orbit with a_o=0.01 and r=3m

Spherical photon orbit with a_o=0.01 and r=$(r_1+r_3)/2$ (Top view)

Figure 1.4.9: Representations in Cartesian space of a single spherical photon orbit with $a = 0.01m$; the variation of the affine parameter along the orbit was 300 also for both. Because $a_o \simeq 0$ the orbit is almost in a plane. However because $a \neq 0$ there is a small frame dragging effect (when compared with $a_o = 0.8$) that shifts the orbital plane in the sense of the BH spin. (*Top*): $r = 3m$, which implies the orbital "plane" crosses the equator perpendicularly. (*Bottom*): In this case $r = (r_1 + r_3)/2$, and so the orbital "plane" crosses the equator diagonally; its projection on the xy plane is therefore an ellipse. A top view (z axis) is here used.

1.5 BH Shadows

The observational perspective of a BH is in itself an interesting subject, with potentially practical astronomical utility. We now develop the tools necessary to discuss this topic.

1.5.1 Local observer basis

For each point in space-time is possible to find a orthonormal basis associated with an observer in that point [22, 28]. This basis can be expanded in the coordinate basis $\{\partial_t, \partial_r, \partial_\theta, \partial_\varphi\}$, associated with Boyer-Lindquist coordinates (see (1.1.1)). It is clear that ∂_r and ∂_θ are each already orthogonal to the rest of the basis vectors (just not normalized), since $g^{\mu r} = 0$ for $\mu \neq r$ and $g^{\mu\theta} = 0$ for $\mu \neq \theta$.

Therefore our vector orthonormal basis $\{\hat{e}_{(t)}, \hat{e}_{(r)}, \hat{e}_{(\theta)}, \hat{e}_{(\varphi)}\}$ should have the form[36]:

$$\begin{aligned}
\hat{e}_{(\theta)} &= A^\theta \partial_\theta, && (1.5.1)\\
\hat{e}_{(r)} &= A^r \partial_r, && (1.5.2)\\
\hat{e}_{(\varphi)} &= A\partial_\varphi + B\partial_t, && (1.5.3)\\
\hat{e}_{(t)} &= \zeta\, \partial_t + \gamma\, \partial_\varphi, && (1.5.4)
\end{aligned}$$

where $\{A, B, \zeta, \gamma, A^\theta, A^\varphi\}$ are real coefficients. The normalization of these vectors are defined by the scalar products[37]:

$$\begin{aligned}
1 &= \hat{e}_{(\theta)} .\, \hat{e}_{(\theta)}, && (1.5.5)\\
1 &= \hat{e}_{(\varphi)} .\, \hat{e}_{(\varphi)}, && (1.5.6)\\
1 &= \hat{e}_{(r)} .\, \hat{e}_{(r)}, && (1.5.7)\\
-1 &= \hat{e}_{(t)} .\, \hat{e}_{(t)}, && (1.5.8)
\end{aligned}$$

The $\hat{e}_{(t)}$ vector has a time-like normalization and the rest of the basis vectors a space-like one, as locally the observer perceives Minkowski space-time.

We also require that

$$0 = \hat{e}_{(t)} .\, \hat{e}_{(\varphi)}.$$

So we obtain:

$$\begin{aligned}
1 &= g_{\theta\theta} \left(A^\theta\right)^2, && (1.5.9)\\
1 &= g_{rr} \left(A^r\right)^2, && (1.5.10)\\
1 &= g_{\varphi\varphi} A^2 + g_{tt} B^2 + 2 g_{t\varphi} A B, && (1.5.11)\\
-1 &= g_{tt} \zeta^2 + g_{\varphi\varphi} \gamma^2 + 2 g_{t\varphi} \zeta \gamma, && (1.5.12)\\
0 &= g_{t\varphi} A \zeta + g_{\varphi\varphi} A \gamma + g_{tt} B \zeta + g_{t\varphi} B \gamma. && (1.5.13)
\end{aligned}$$

---

[36] However many other, less simple combinations are also possible, allowing for spatial rotations and Lorentz boosts.

[37] The scalar product between the 4-vectors $\underline{a}$ and $\underline{b}$ is given by $\underline{a} \,.\, \underline{b} = g_{\mu\nu}\, a^\mu b^\nu$.

We have three equations (1.5.11 - 1.5.13) for the four unknowns $\{A, B, \zeta, \gamma\}$. We have in fact one extra degree of freedom associated with rotations in the (t, φ) plane, each configuration being an orthogonal set. The analogy in Cartesian 3-space is rotations along the z axis, as each new configuration of the x, y axis in the (x, y) plane is of course orthonormal.
Therefore, we can choose

$$B = 0,$$

without loss of generality, in order to have a more familiar vector $\hat{e}_{(\varphi)}$ with no t component. This particular choice is connected to a reference frame with zero axial angular momentum in relation to infinity, and hence it is sometimes called the ZAMO reference frame[38] [1]. However an observer at rest in this frame moves with respect to the Boyer-Lindquist coordinate system, as a consequence of frame-dragging (see page 8).
With this new condition we have

$$A^\theta = \frac{1}{\sqrt{g_{\theta\theta}}}, \tag{1.5.14}$$

$$A^r = \frac{1}{\sqrt{g_{rr}}}, \tag{1.5.15}$$

$$A = \frac{1}{\sqrt{g_{\varphi\varphi}}}, \tag{1.5.16}$$

where the sign of the square roots were chosen positive so that at infinity we have the standard orthogonal basis in spherical coordinates.
We also have

$$-1 = g_{tt}\zeta^2 + g_{\varphi\varphi}\gamma^2 + 2g_{t\varphi}\zeta\gamma,$$

and

$$\zeta = -\frac{g_{\varphi\varphi}}{g_{t\varphi}}\gamma, \tag{1.5.17}$$

which combined lead to

$$-1 = g_{tt}\frac{g_{\varphi\varphi}^2}{g_{t\varphi}^2}\gamma^2 + g_{\varphi\varphi}\gamma^2 - 2\frac{g_{t\varphi}g_{\varphi\varphi}}{g_{t\varphi}}\gamma^2,$$

$$\gamma^2 = \frac{g_{t\varphi}^2}{g_{\varphi\varphi}g_{t\varphi}^2 - g_{tt}g_{\varphi\varphi}^2}.$$

So we obtain

$$\gamma = \pm\frac{g_{t\varphi}}{g_{\varphi\varphi}}\sqrt{\frac{g_{\varphi\varphi}}{g_{t\varphi}^2 - g_{tt}g_{\varphi\varphi}}}.$$

---

[38] ZAMO stands for *zero angular momentum observers.*

We choose the negative root for γ in order to have at spatial infinity $\hat{e}_{(t)} \to \partial_t$ (see below).
Using this choice and also (1.5.17) we obtain [28]:

$$\boxed{\gamma = -\frac{g_{t\varphi}}{g_{\varphi\varphi}}\sqrt{\frac{g_{\varphi\varphi}}{g_{t\varphi}^2 - g_{tt}g_{\varphi\varphi}}},} \tag{1.5.18}$$

$$\boxed{\zeta = \sqrt{\frac{g_{\varphi\varphi}}{g_{t\varphi}^2 - g_{tt}g_{\varphi\varphi}}}.} \tag{1.5.19}$$

As one can easily check in the limit $r \to \infty$,

$$g_{\varphi\varphi} \to r^2 \sin^2\theta, \qquad g_{t\varphi} \to 0, \qquad g_{tt} \to -1,$$

so we have

$$\gamma \to 0, \quad \zeta \to 1,$$

and

$$\hat{e}_{(t)} \to \partial_t$$

as intended.

The locally[39] measured energy $p^{(t)}$ of a particle is given by the projection[40] of its 4-momentum[41] $\underline{p}$ onto $\hat{e}_{(t)}$ [22]:

$$p^{(t)} = -(\hat{e}_{(t)} \cdot \underline{p}) = -(\hat{e}^{\mu}_{(t)}\, p_\mu) = -(\zeta p_t + \gamma p_\varphi).$$

As was previously mentioned, $E = -p_t$ and $p_\varphi = \Phi$ are respectively the particle's energy and angular momentum relative to a static observer at infinity[42] [22] (in units $c = 1$, $G = 1$, see footnote 22 on page 17).
We have therefore

$$\boxed{p^{(t)} = E\zeta - \gamma\Phi.} \tag{1.5.20}$$

We also have for the locally measured linear momentum in the $\hat{e}_{(\theta)}$, $\hat{e}_{(\varphi)}$ and $\hat{e}_{(r)}$ directions:

$$\boxed{p^{(\theta)} = \hat{e}^{\mu}_{(\theta)}\, p_\mu = \frac{1}{\sqrt{g_{\theta\theta}}} p_\theta,} \tag{1.5.21}$$

---

[39] A local measurement of a particle's property is performed by an observer at a given frame in the same position as the particle.

[40] Notice that the projection of the 4-momentum $\underline{p}$ onto $\hat{e}_{(t)}$ must be multiplied by a minus sign to yield the locally measured energy. This is a consequence of the time-like normalization $\hat{e}_{(t)} \cdot \hat{e}_{(t)} = -1$.

[41] The 4-vector $\underline{p}$ is only the 4-momentum in units $c = 1$, $G = 1$. Otherwise $\underline{p} = G\,\underline{p^*}/c^3$ (see page 12).

[42] This statement can be justified by setting $r \to \infty$, which leads to $p^{(t)} = E$ and to $p^{(\varphi)} r \sin\theta = \Phi$.

$$\boxed{p^{(\varphi)} = \hat{e}^{\mu}_{(\varphi)}\, p_\mu = \frac{1}{\sqrt{g_{\varphi\varphi}}}\Phi,} \tag{1.5.22}$$

$$\boxed{p^{(r)} = \hat{e}^{\mu}_{(r)}\, p_\mu = \frac{1}{\sqrt{g_{rr}}}p_r.} \tag{1.5.23}$$

Notice than a photon with zero angular momentum[43] ($\Phi = 0$), or any other type of particle for that matter, is observed in the ZAMO frame with no momentum component in the $\hat{e}_{(\varphi)}$ direction. This is due to the fact that an observer at rest at ZAMO also has zero angular momentum with respect to infinity, as was previously stated.

1.5.2 Impact parameters x' and y'

The photons detected can be projected in an image plane, according to the observer's perspective. The Cartesian coordinates (x', y') assigned to each photon in this image plane are defined as its impact parameters [28] and are proportional to the respective observation angles (α, β) (see Fig. 1.5.1).

The solid angle or angular size that a given object (such as a BH) occupies in the observer's sky depends strongly on the distance between the two. However this "distance" is a very subtle concept in a curved space-time: for instance, the proper distance to a Kerr BH diverges in some cases [22]. For this reason a different quantity is used. Given a circumference at the equator ($\theta = \pi/2$) with constant radial coordinate r, its perimeter $\mathcal{P}$ is given by

$$\mathcal{P} = \int_0^{2\pi} \sqrt{g_{\varphi\varphi}}\, d\varphi = 2\pi\sqrt{g_{\varphi\varphi}}.$$

Since $g_{\varphi\varphi}$ does not have a dependence on the coordinate φ the integration is trivial. The perimetral or circumferential radius $\tilde{r}$ is then defined as

$$\tilde{r} \equiv \frac{\mathcal{P}}{2\pi} = \sqrt{g_{\varphi\varphi}}. \tag{1.5.24}$$

This quantity is a possible choice[44] to measure the distance to a BH (the radial coordinate r would itself be a very naive option). We expect the angles α, β to have typically a $1/\tilde{r}$ dependence, at least for large distances to the BH and so the impact parameters are more naturally defined as [22, 28]:

$$x' = -\tilde{r}\beta \qquad \text{and} \qquad y' = \tilde{r}\alpha, \tag{1.5.25}$$

---

[43] This angular momentum is only orbital, it is not related to the photon's Quantum Mechanical spin!

[44] Other choices are of course equally possible, such as the radius defined by a topological spherical surface area.

where the perimetral radius $\tilde{r}$ is computed at the position of the observer. The minus sign in the x' equation comes from the fact that a detection with $\beta > 0$ corresponds to a point in the left side of the image plane (if observer is looking at the BH), and therefore to a negative x' (see Fig. 1.5.1). The associated vectors $\hat{e}_{x'}$ and $\hat{e}_{y'}$ are defined by

$$\hat{e}_{x'} = \hat{e}_{(\varphi)} \qquad \text{and} \qquad \hat{e}_{y'} = -\hat{e}_{(\theta)}.$$

The observation angles (α, β) are both defined to be zero in the direction pointing to the center of the BH, in the observer's frame.

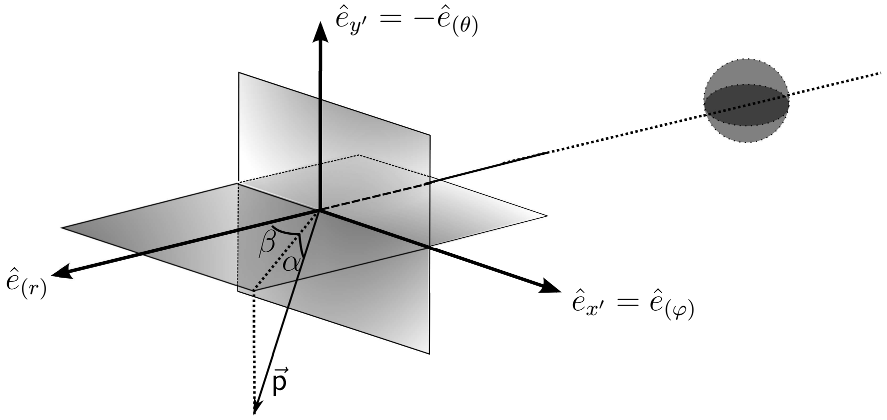

Figure 1.5.1: Perspective drawing of the geometric projection of the photon's linear momentum $\vec{\mathsf{p}}$ in the observer's frame $\{\hat{e}_{(r)}, \hat{e}_{(\theta)}, \hat{e}_{(\varphi)}\}$. The observation angles α, β were drawn as positive. The planes associated with the angles α and β are perpendicular between themselves and the 3-vector $\vec{\mathsf{p}}$ is in the same plane as α. The vectors $\hat{e}_{x'}$ and $\hat{e}_{(r)}$ and the β angle are also all in the same plane. The BH is represented by the grey sphere in the image.

In the following steps $|\vec{\mathsf{p}}| = \mathsf{p}$ is the modulus of the classic 3-vector linear momentum[45], with components $p^{(r)}, p^{(\theta)}$ and $p^{(\varphi)}$ in a Cartesian 3-space with a spherical orthonormal basis. We then have

$$\mathsf{p}^2 = \left[p^{(r)}\right]^2 + \left[p^{(\theta)}\right]^2 + \left[p^{(\varphi)}\right]^2.$$

Attending to the geometry of the photon detection angles α, β (see Fig. 1.5.1), we also have

$$p^{(\varphi)} = \mathsf{p} \sin\beta \, \cos\alpha, \tag{1.5.26a}$$

$$p^{(\theta)} = \mathsf{p} \sin\alpha, \tag{1.5.26b}$$

$$p^{(r)} = \mathsf{p} \cos\beta \, \cos\alpha. \tag{1.5.26c}$$

---

[45] This 3-vector momentum is in $c = 1$ and $G = 1$ units like the corresponding 4-momentum $\underline{p}$.

In the following calculations the observer will be assigned a radial coordinate r_o and a latitude angle θ_o. The distance between the observer and the BH will be assumed to be very large ($r \gg m$) and so in this limit we have $\tilde{r} \to r_o$ (the full calculation without this approximation can be found in Appendix A.6). The observation angles $\alpha, \beta \ll 1$ will also be very small and so

$$p^{(\varphi)} \simeq \mathsf{p}\,\beta,$$
$$p^{(\theta)} \simeq \mathsf{p}\,\alpha.$$

The locally measured energy ε of a photon is $\varepsilon = \mathsf{p}c$ (in S.I. units). We have therefore, in units $c = 1$, that

$$\beta \simeq \frac{p^{(\varphi)}}{\varepsilon}, \qquad \text{and} \qquad \alpha \simeq \frac{p^{(\theta)}}{\varepsilon}.$$

Because the locally measured energy is $p^{(t)}$ then we have

$$\varepsilon = p^{(t)}.$$

The impact parameters are then given by

$$\boxed{x' = -r_o \frac{p^{(\varphi)}}{p^{(t)}},} \tag{1.5.27}$$

and by

$$\boxed{y' = r_o \frac{p^{(\theta)}}{p^{(t)}}.} \tag{1.5.28}$$

Using (1.5.20), (1.5.21), (1.5.22) and from (1.3.2) the fact that

$$p_\theta = g_{\theta\theta}\, p^\theta = \rho^2 \dot{\theta} = \pm\sqrt{\Theta},$$

we obtain for the impact parameters

$$x' = -\, r_o \frac{\Phi}{(E\zeta - \gamma\Phi)\sqrt{g_{\varphi\varphi}}},$$

$$y' = \pm r_o \frac{\sqrt{\Theta}}{(E\zeta - \gamma\Phi)\sqrt{g_{\theta\theta}}}.$$

In the limit $r_o \to \infty$ for very far observers, like for instance one set on planet Earth, we have

$$g_{\varphi\varphi} \to r_o^2 \sin^2\theta_o, \qquad (E\zeta - \gamma\Phi) \to E \qquad \text{and} \qquad g_{\theta\theta} \to r_o^2.$$

So we get [20]

$$\boxed{x' = -\frac{\Phi/E}{\sin\theta_o} = -\frac{\lambda}{\sin\theta_o},} \tag{1.5.29}$$

and

$$\boxed{y' = \pm\frac{\sqrt{\Theta}}{E} = \pm\sqrt{\eta + a^2\cos^2\theta_o - \lambda^2/\tan^2\theta_o},} \tag{1.5.30}$$

where (1.3.2) and (1.4.1) were used. Notice that these last equations are only valid in the limit for very far observers ($r \gg m$).

1.5.3 Shadow of a BH

Imagine there is a light source in the background, behind a Kerr BH relatively to the observer, and which angular size is large when compared with the mentioned BH (for instance background stars) [22].
The optical perception for a distant observer will be a silhouette over the background light (for illustrative purposes see Fig. 1.5.2). This region in the image plane for which no light is detected is called the BH's shadow [28]. The "rim" of this shadow depends only on the space-time metric around the BH [28] . This outer rim, also called photon ring, is connected with the photons that can get closest to the BH and still escape to infinity.

Due to the "No Bound Theorem" (see Appendix A.5) there can be at most two turning points[46] outside the event horizon. Given $\{Q, \Phi\}$, the energy E can be chosen in order to have two, one or no turning points (this is easiest to see through the effective potential V_+ in Appendix A.5). The unstable spherical orbits are the limit between two turning points and none, at a specific value of E (given Q, Φ). Spherical orbits are therefore the closest photons can get to the BH and still be able to escape. Photon rings are thus created by photons that almost follow spherical orbits and, because these are unstable, they are on the verge of either being captured or escaping.

From (1.4.10) it is known the values of $\lambda(r)$ and $\eta(r)$ for each orbital radius r. Using (1.5.29) and (1.5.30), the photon rings can be parametrically described in the image plane $\Big(x'(r), y'(r)\Big)$ as function of the orbital radius r of each photon, within the range $r_1 \leq r \leq r_2$ (condition for $\eta \geq 0$). These rings are represented in Fig. 1.5.3 and Fig. 1.5.4 for different values of a and observation angles θ_o.

---

[46] A turning point occurs when $R = 0$

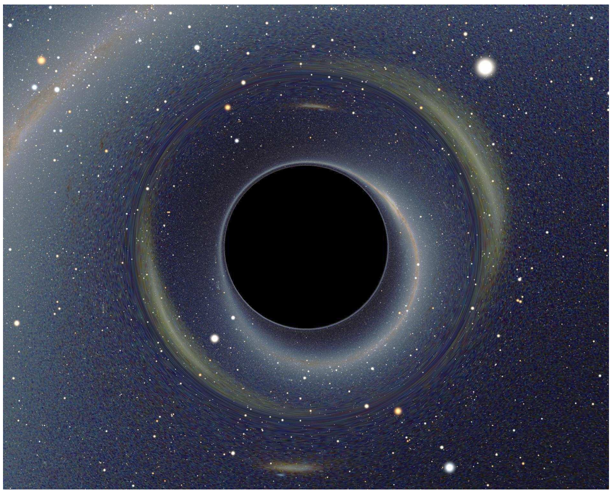

Figure 1.5.2: Computer simulation of gravitational lensing produced by a BH passing in front of the Magellanic Clouds in the Southern Hemisphere (simulation by A. Riazuelo) [29–31]. The dark region in the picture is the BH's shadow and its edge is the photon ring.

To continue the analysis and investigate other interesting features, such as gravitational lensing near the shadow's rim, it is adequate to conduct a numerical simulation of light rays from a given source to a "camera" (our observer). The information carried by each ray (such as intensity, color) would be respectively assigned to a pixel in a final image, which embodies the optical perception of the observer[47].

Numerically this could be done by integrating the equations of motion for null geodesics. The most naive approach would be to evolve the light rays directly from the source and detect which ones reach the camera. However this procedure is very inefficient since most rays would not reach it and thus spend unnecessary computation time.

A better approach is to evolve the light rays from the camera backwards in time and identify its origin [32–34], a method named *backward ray-tracing*, also used in video-game engines. The angular coordinates (α, β) (see Fig. 1.5.1) of a point in the camera's local sky[48] define the direction of the associated light ray and establishes its initial conditions. A very interesting problem however is to obtain the constants of motion of the photon $\{E, \Phi, Q\}$ given the coordinates (α, β).

---

[47] The human eye in this sense is also considered a "camera".

[48] The local sky is the apparent projection of stellar objects in a sphere centered on the observer.

The 4-momentum $\underline{p}$ squared is given by

$$\underline{p}\cdot\underline{p} = -\mu^2 = -\left(p^{(t)}\right)^2 + \mathsf{p}^2.$$

Therefore for photons with rest mass $\mu = 0$ we have

$$p^{(t)} = \mathsf{p}.$$

Combining the equations of motion (1.3.1 - 1.3.4) and the 4-momentum projections (1.5.20 - 1.5.26), we obtain:

$$p_\theta = \mathsf{p}\,\sqrt{g_{\theta\theta}}\,\sin\alpha, \tag{1.5.31a}$$
$$\Phi = \mathsf{p}\,\sqrt{g_{\varphi\varphi}}\,\sin\beta\,\cos\alpha, \tag{1.5.31b}$$
$$p_r = \mathsf{p}\,\sqrt{g_{rr}}\,\cos\beta\,\cos\alpha, \tag{1.5.31c}$$
$$E = \mathsf{p}\,\left(\frac{1+\gamma\sqrt{g_{\varphi\varphi}}\,\sin\beta\,\cos\alpha}{\zeta}\right). \tag{1.5.31d}$$

Notice that by using equations (1.5.20 - 1.5.23) we are implicitly assuming that our observer (or camera) is a ZAMO frame. Also, curiously the value of p is redundant[49] for the geodesic trajectory since its variation leads to a simple rescaling of the affine parameter. For this reason the value of p can be set to unity for simplicity.
The relations (1.3.7) and (1.3.8) are now useful to obtain the values of Q and μ given $\{p_r, p_\theta, E, \Phi\}$. Naturally for a photon we have $\mu = 0$ but this procedure can be implemented numerically as a cross-check.

In practice the camera's local sky is divided into small solid angles, each corresponding to a pixel in the camera's final image (see Fig. 1.5.5). For each pixel the constants of motion $\{E, \Phi, Q\}$ are determined from the pixel's coordinates (α, β). The equations of motion (1.3.1 - 1.3.4) are then integrated numerically backwards, which can be achieved by setting the affine parameter's numerical differential negative. If the photon reaches a light source or a BH then the integration stops, there is optical information assigned to the respective pixel and the process is repeated.
The field of view of the observer is related to the range of α, β. For instance, if the range of α is $[-\psi, \psi]$, where ψ is some bound, then the field of view angle is 2ψ; also for short one can say that the range is $\pm\psi$.

A simple and interesting paradigm is a source placed at infinity, very far from both the observer and the BH. For numerical reasons however, it was considered a different but similar configuration, with a finite spherical light

---

[49] The value of p only establishes the photon's frequency and does not influence the trajectory itself.

source, which will be named "celestial sphere", englobing and enclosing both the BH and the observer, but concentric with the first (see Fig. 1.5.6). The ray tracing algorithm is thus a mapping between a point in the camera's local sky and a point in the celestial sphere. If a pattern is "imprinted" on the celestial sphere (see Fig. 1.5.7 for instance), then a ray that reaches a given point on that surface retrieves the pattern information at that point back to the initial pixel, in the local sky. The pattern could for instance be grey levels of an image, related to light intensity of the source. On the other hand, a ray that has its origins from a point on the event horizon[50] of the BH corresponds naturally to a black pixel (no light came from that direction).

Although two BHs with different values of a are each still a member of the Kerr family, they have distinct space-time geometries; the coordinate r is not even directly comparable between such solutions. At this point it is important to establish a criteria for similar observation conditions in different space-times: two observers are in similar observation conditions if the perimetral radius $\tilde{r}$ is the same for both observers (see (1.5.24)). This implies

$$\sqrt{g_{\varphi\varphi}{}^{(1)}} = \sqrt{g_{\varphi\varphi}{}^{(2)}},$$

where each superscript (1) and (2) labels the respective space-time. Of course some reference distance must still be provided to make the final link; for the moment, the distance[51] defined by the parameter m will be used for such a purpose.

An interesting point is that for flat space (which is an endpoint of the Kerr family) we have

$$\tilde{r} = \sqrt{g_{\varphi\varphi}{}^{(\text{flat})}} = r^{(\text{flat})}.$$

Comparing observations in flat space with observations for a Kerr BH at a radial coordinate r yields then

$$\tilde{r} = \sqrt{r^2 + a^2 + \frac{2ma^2}{r}}.$$

The inversion of this equation leads to (see Appendix A.4)

$$r = 2\sqrt{\frac{\tilde{r}^2 - a^2}{3}} \cos\left(\frac{1}{3}\arccos\left[\frac{3a^2 m}{a^2 - \tilde{r}^2}\sqrt{\frac{3}{\tilde{r}^2 - a^2}}\right]\right). \qquad (1.5.32)$$

So, given a radius $\tilde{r}$ in flat space, we can compute the equivalent radial coordinate r in Kerr space-time that leads to similar observation conditions. In

---

[50] This condition is obtained if either $r \leq r_1$ or $\Delta \leq 0.01m$.

[51] The mass M is fixed for all cases. The distance m is thus a well defined quantity, even for flat space (where there is no BH).

practice however, the difference $(\tilde{r} - r)$ is quite small compared with $\tilde{r}$, unless the Kerr observer is very close to the BH. For example, for $a = 0.999m$ we have $\tilde{r} = 15m \implies r \simeq 14.96m$.
Continuing the current reasoning we can also define the celestial sphere to be at a given perimetral radius[52] (different from the observer) and compute the respective Kerr radial coordinate using (1.5.32).

For the numerical integration an embedded Runge-Kutta method with Dormand-Prince 5(4) parameters was used [27]. This method has an adaptive step size and was implemented in a C++ code. The data from the numerical simulations was then processed by MatLab and saved into images[53], from Fig. 1.5.7 to Fig. 1.5.13. No gravitational or Doppler frequency shifts were considered and neither was the Liouville's[54] brightness shift. Also, no optical aberrations were taken into account [32].

---

[52] For simplicity the perimetral radius $\tilde{r}$ is computed at the equator ($\theta = \pi/2$) but set constant on the surface $r = Const.$.

[53] These images are all new. They are either completely original or are modifications of pictures which originally did not display a BH.

[54] By Liouville's theorem the specific intensity $I_\nu \propto \nu^3$ [32].

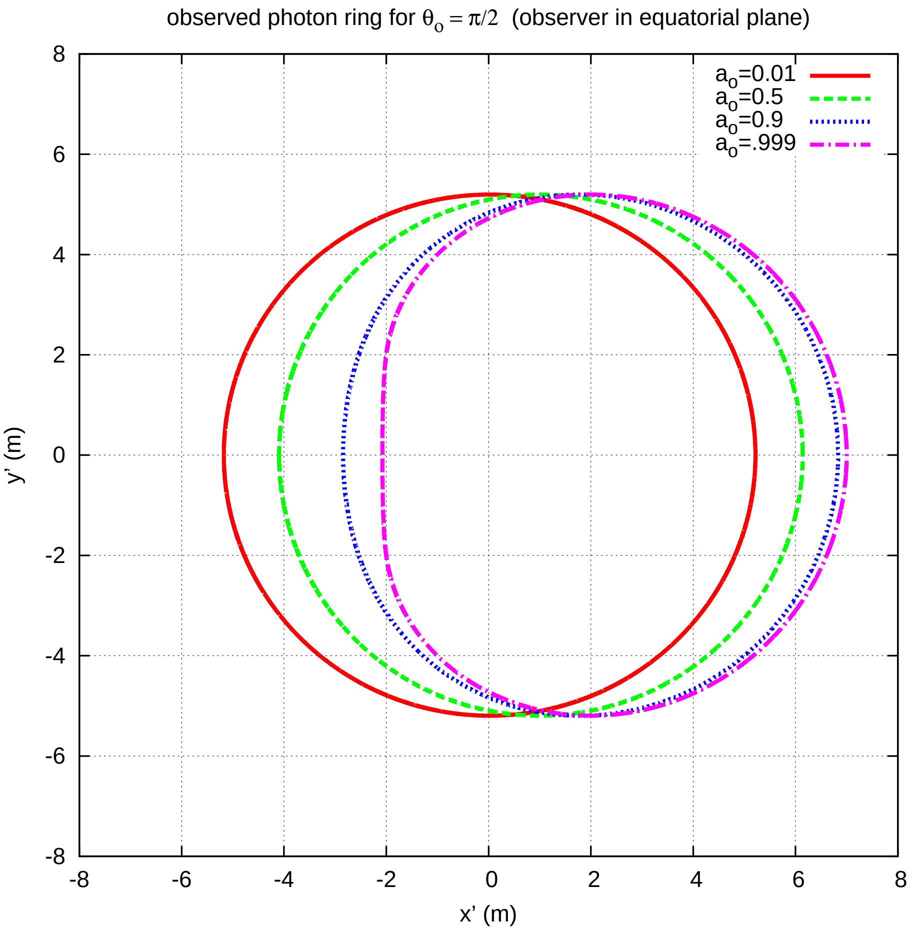

Figure 1.5.3: Graphic representation of the photon ring, as observed from very large distances ($r \gg m$) in the equatorial plane of the BH ($\theta_o = \pi/2$) (see (1.5.29) and (1.5.30)). Different values of the dimensionless rotation parameter $a_o = a/m$ are displayed. Notice that for $a_o \simeq 0$ we have almost a circle due to the symmetry of the Schwarzschild solution and for $a_o \simeq 1$ we have a highly asymmetric geometric shape due to the symmetry violation in the latitude coordinate θ for the Kerr metric. Notice that the shadow (region inside photon ring) is larger than the event horizon's angular size, as we must have $r_+ \leq 2m$.

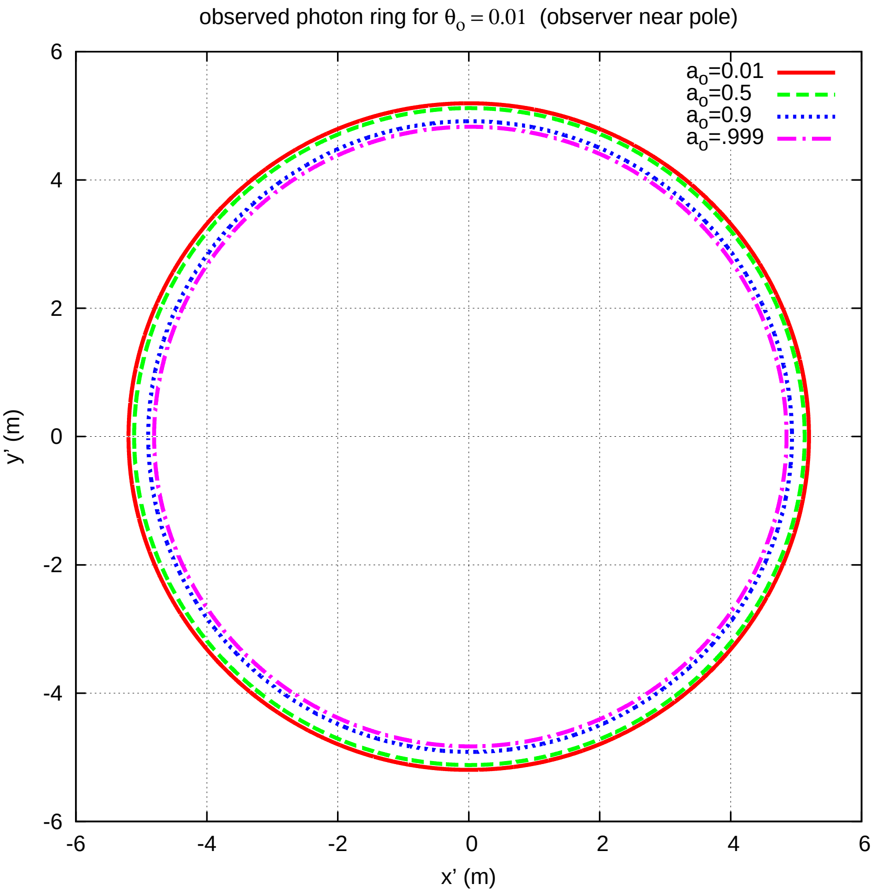

Figure 1.5.4: Graphic representation of the photon ring as observed from very large distances ($r \gg m$) in the z axis ($\theta_o = 0$) of the BH (see (1.5.29) and (1.5.30)). Different values of the dimensionless rotation parameter $a_o = a/m$ are displayed. From this observation perspective the photon rings are circles for all values of a, due to the symmetry in the azimuthal φ coordinate. Notice that the shadow (region inside photon ring) is larger than the event horizon's angular size, as we must have $r_+ \leq 2m$.

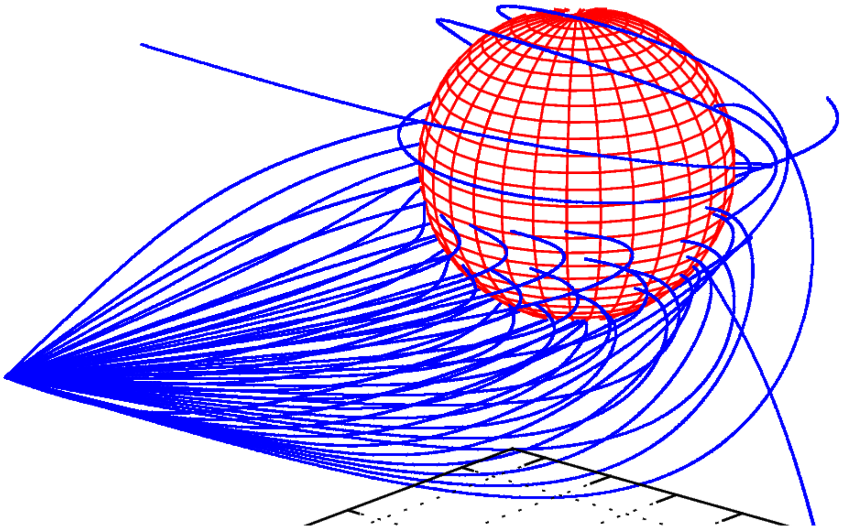

Figure 1.5.5: Graphical representation of the light rays (blue lines) and a BH (red sphere) with spin $a = 0.8m$. The numerical data is displayed as if the Boyer-Lindquist coordinates were spherical. The rays branching point in the figure corresponds to the position of the observer, which is at the equatorial plane with $\tilde{r} = 15m$.

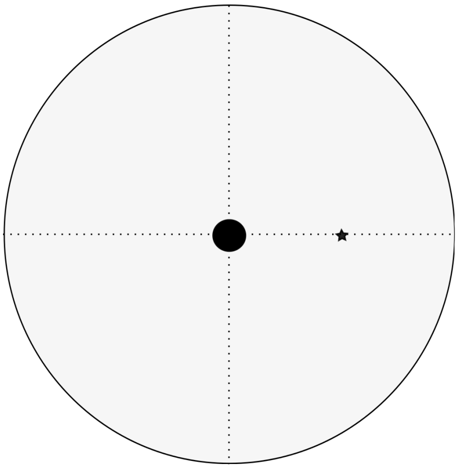

Figure 1.5.6: Schematic drawing of the spherical light source paradigm. The celestial sphere is represented as the larger circle, the BH as the black circle in the center of the image and the observer as the small star. Notice that both the observer and the BH are inside the celestial sphere. The observer is at a perimetral radius $\tilde{r} = 15m$ and the celestial sphere is on the surface $\tilde{r} = 30m$. Because the observer is not centered within the celestial sphere then the projection of the latter on the local sky has parallax distortions (see Fig. 1.5.9).

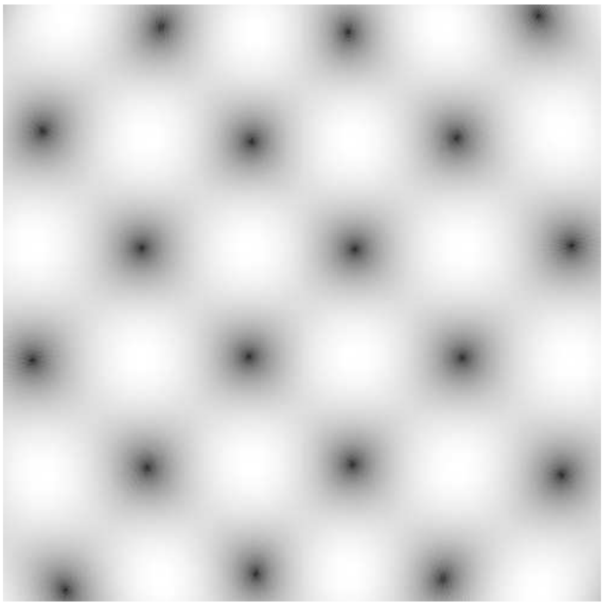

Figure 1.5.7: A possible pattern on the celestial sphere. This figure corresponds to the optical perception of an observer at coordinates $\theta = \pi/2$, $\varphi = 0$ and perimetral radius $\tilde{r} = 15m$ but without a BH (it is flat space) (compare with Fig. 1.5.8). The grey level pattern of the image is given by $[(1 + \sin(10\,\varphi)\sin(10\,\theta))/2]^{1/5}$, normalized into the range $[0, 1]$; the coordinates (θ, φ) are the respective Boyer-Lindquist coordinates on the celestial sphere (surface at $\tilde{r} = 30m$). The range of (α, β) (field of view) is $\pm \arctan(10/15)$ for both angles. The horizontal axis is connected to β and the vertical axis to α.

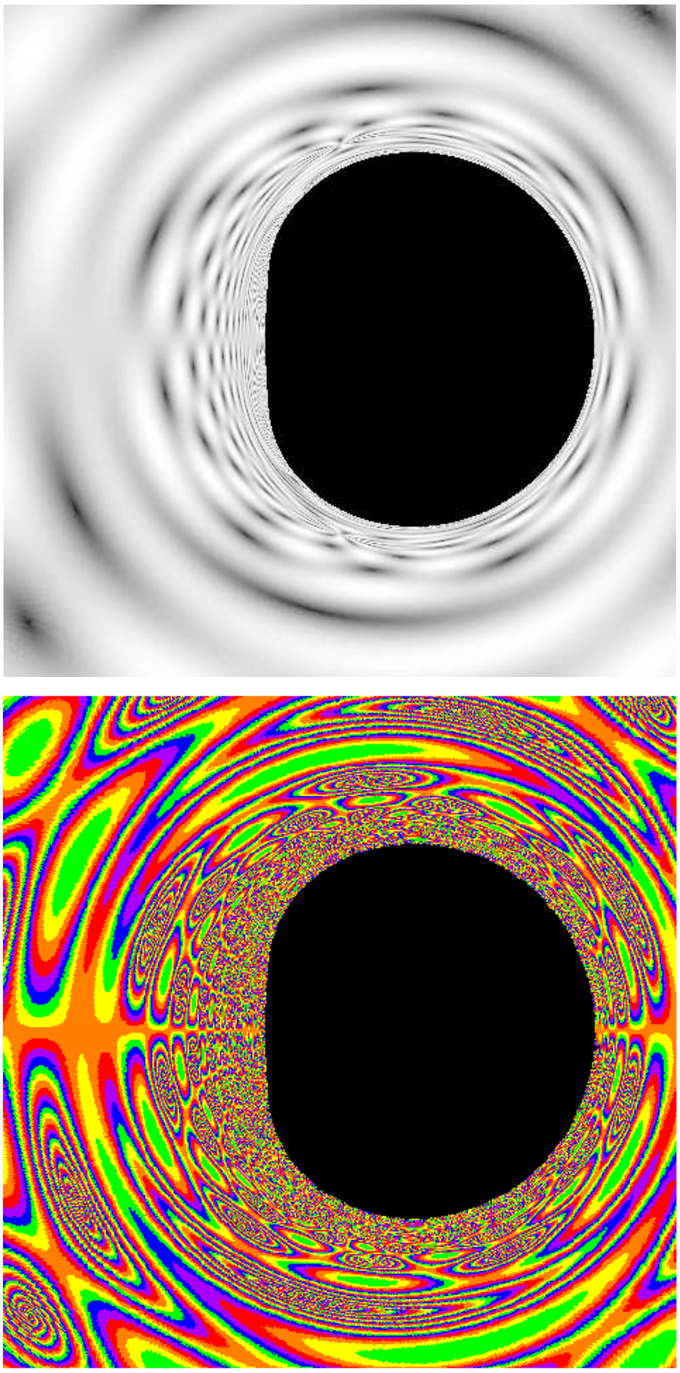

Figure 1.5.8: (*Top*): This figure corresponds to the optical perception of an observer in the same conditions as in Fig. 1.5.7 but with an extremal BH ($a = m$). The strong lensing effect over the background pattern is very clear. It is also interesting to compare the edge of the shadow (the dark region) with Fig. 1.5.3. The range of (α, β) (field of view) is $\pm \arctan(10/15)$ for both angles. This image was generated by ray-tracing of 500×500 photon trajectories. (*Bottom*): Image on top with a periodic pseudo color scale from MatLab that enhances the local differences in the grey level. With this curious representation is easier to perceive the fractal-like recurrence pattern near the shadow's edge.

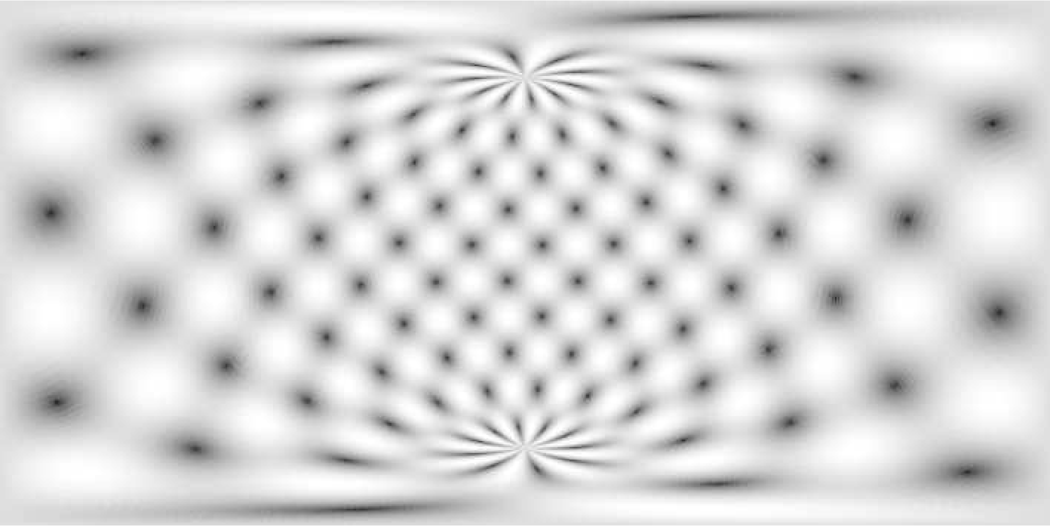

Figure 1.5.9: This figure corresponds to the optical perception of an observer in the same conditions as in Fig. 1.5.7 (thus without a BH) but with a larger field of view that spans all the local sky: $\alpha \in [-\pi/2, \pi/2]$ and $\beta \in [-\pi, \pi]$. The horizontal axis is connected to β and the vertical axis to α. The distortion in the pattern is only due in this case to parallax, since the observer is not centered within the celestial sphere and it is at a finite distance from it. The two star like structures are each one a pole on the celestial sphere.

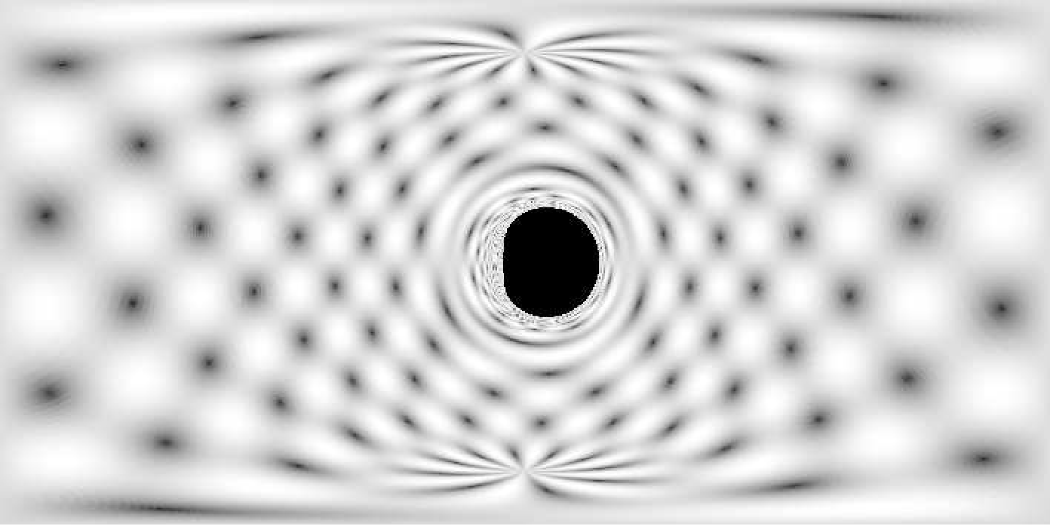

Figure 1.5.10: This figure corresponds to the optical perception of an observer in the same conditions as in Fig. 1.5.9 but with an extremal BH ($a = m$). The image surrounding the shadow is the same as in Fig. 1.5.8.

Figure 1.5.11: This image is similar to Fig. 1.5.10 but with a different pattern in the celestial sphere, just for fun. The projection on the celestial sphere was also corrected for the parallax distortion (see Appendix A.7). The background image shown is the campus of Santiago at the University of Aveiro, Portugal. The Einstein ring, an important feature of gravitational lensing, is here easily discernible as a sharp circle: notice that inside it objects are inverted/upside down, like the blue sky for instance. [35]

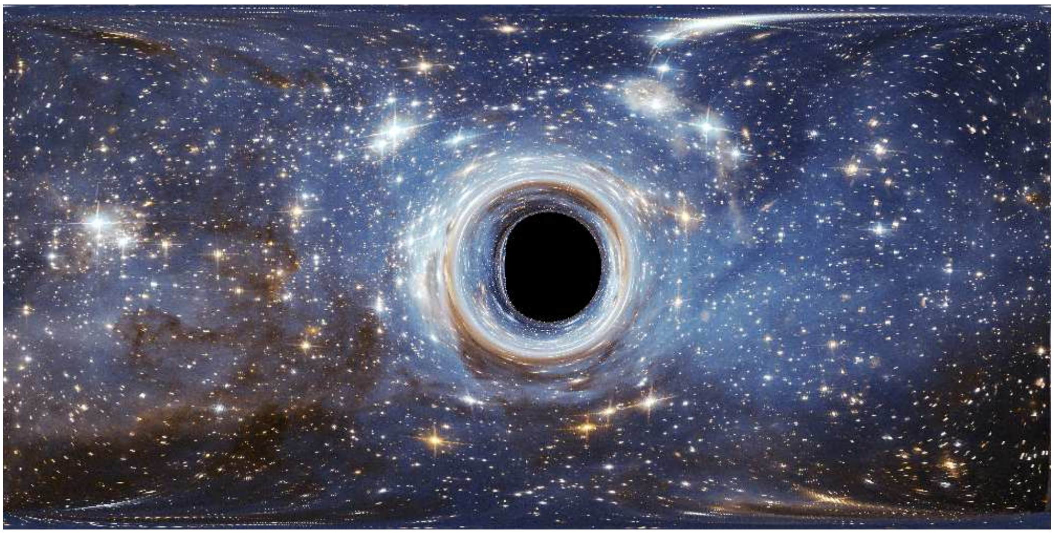

Figure 1.5.12: Similar as in Fig. 1.5.11 but with a star field in the background. The original image is from the European Space Agency and taken with the Hubble Space Telescope. It is listed as the LH 95 star forming region of the Large Magellanic Cloud. [36]

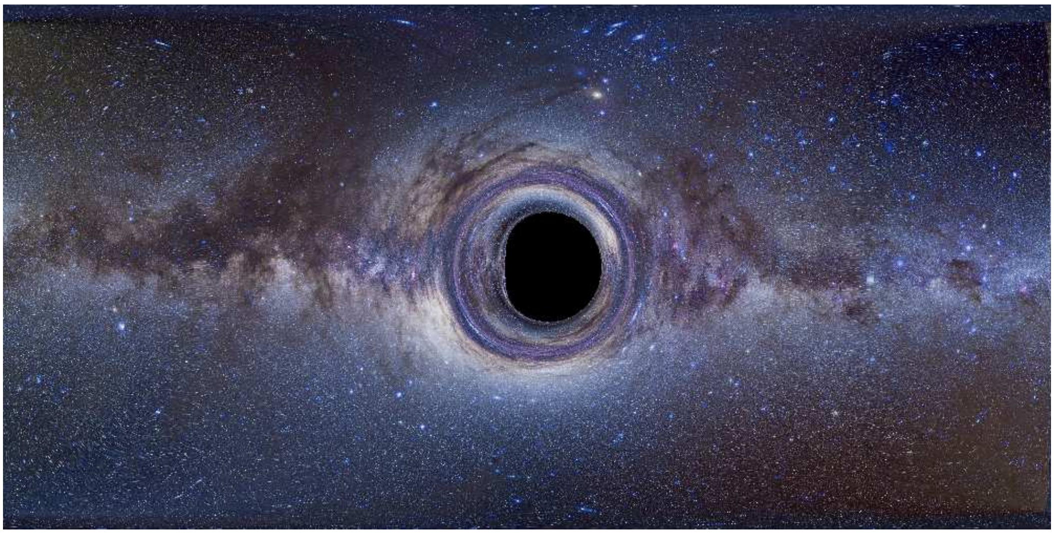

Figure 1.5.13: Different variation of Fig. 1.5.12 and 1.5.11. The star field is from real images of the Milky Way. [37]. Notice the halo around the shadow, produced by the Einstein ring.

1.5.4 Shadow of a BH with accretion disk

In the previous section we considered shadows with a large light source in the background (e.g. stars). However a luminous accretion disk orbiting a BH is also astrophysically relevant to analyse. For this case was used the free software GYOTO, or General relativitY Orbit Tracer of Observatoire de Paris, for the ray tracing algorithm [34, 38], which is not unlike the one used in the previous section. This software has several astrophysical structures already included, one of which is an infinite optically thick thin accretion disk, theoretically developed by Page and Thorne [39].

Using GYOTO several images of shadows of a BH with a Page-Thorn accretion disk were obtained, from Fig. 1.5.14 up to Fig. 1.5.15. These images are as perceived by a static observer at $r = 100m$, $\varphi = 0$ but for different values of coordinate θ and spin a. In this case the gravitational, Doppler and Liouville shifts were taken into consideration. As a consequence the original images obtained were very dim and difficult to read. For this reason was applied a common tool from image processing techniques named gamma correction, which aims to enhance hidden features in the grey levels without producing image artifacts. This operation is a transformation function of the original grey level $\mathcal{P}_o$ to a new level $\mathcal{P}'$ according to the expression

$$\mathcal{P}' = \mathcal{P}_o^{1/\gamma}$$

where the parameter γ is a positive real number and the grey levels are normalized into the interval $[0, 1]$.

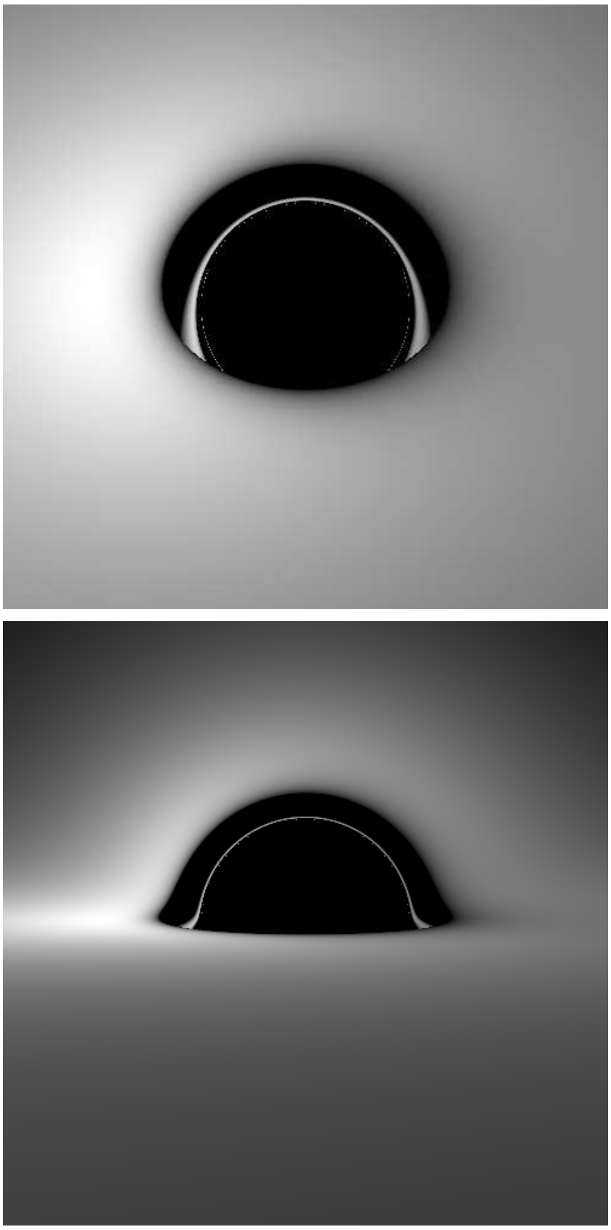

Figure 1.5.14: Images of the optical perception of a Schwarzschild BH ($a = 0$) with a Page-Thorne accretion disk. The field of view angle is 0.3 (full range α, β). The images were subjected to a gamma correction of $\gamma = 3.6$. (*Top*): The observer is at $\theta = 50\pi/180$ (or 50°). The inner structure of the dark region is actually inside the Einstein ring (but outside the shadow) and is a secondary image of the entire disk. The shadow of the BH, which is a circle for Schwarzschild, is partially covered by a portion of the accretion disk, from the observer's perspective. (*Bottom*): observer at $\theta = 85\pi/180$ (or 85°) Although the observer is almost at the equatorial plane it is possible to recognize the section of the disk "behind" the BH in an apparent position above it, as consequence of gravitational lensing (see [32]). Also due to the rotation of the disk, the brightness is larger from the left side than from the right side of the disk (Doppler and Liouville's shift).

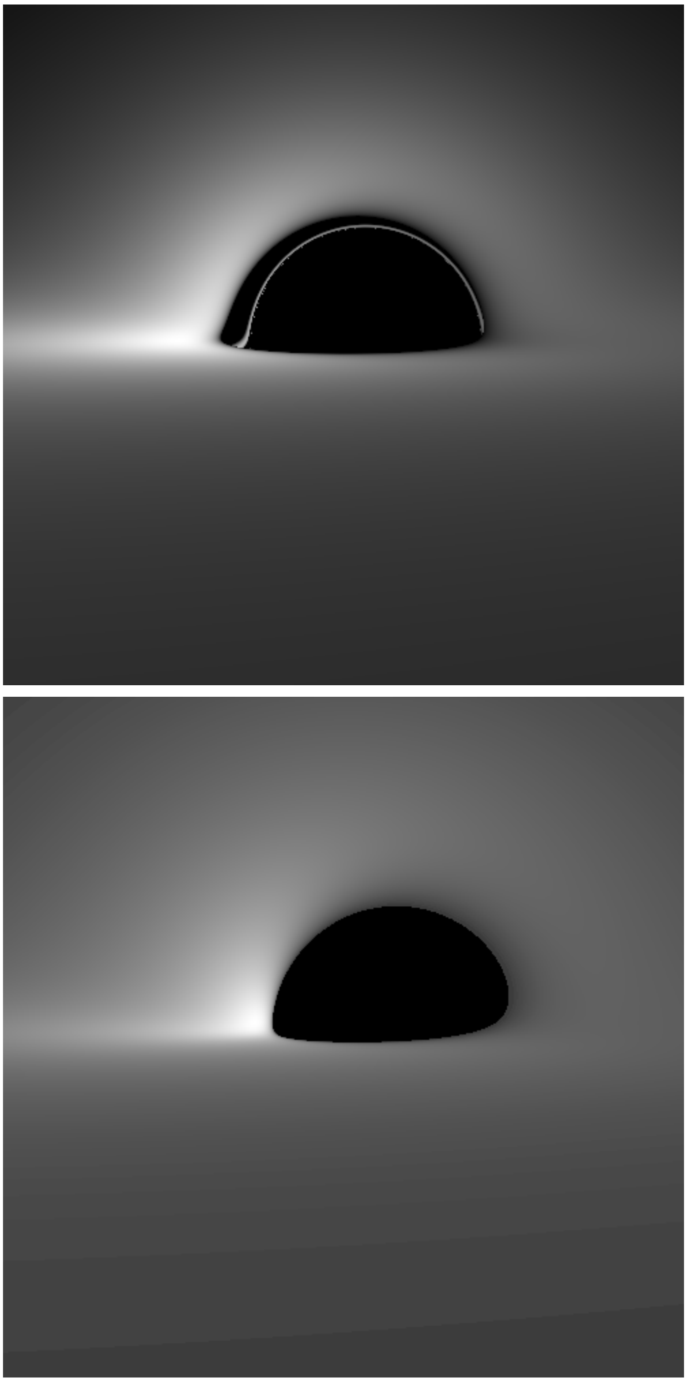

Figure 1.5.15: In both images the observer is at $\theta = 85\pi/180$ (or 85°), but the values of a are different. (*Top*): $a = 0.5m$; notice the asymmetry in the inner structure of the Einstein ring and the increased difference in light intensity due to frame-dragging. The field of view angle is 0.3 and the image was subjected to a gamma correction of $\gamma = 3.6$. (*Bottom*): $a = 0.999m$ (almost a maximally spinning BH). The inner structure of the Einstein ring is now not discernible and the shadow is highly asymmetric. The field of view angle is 0.2 and the gamma correction parameter is $\gamma = 7.7$.

Chapter 2

Hairy Black Holes

2.1 Event Horizon Telescope and GRAVITY

Despite the considerable amount of astronomical data that supports the existence of BHs, there is still no absolute proof that the observed BH candidates are indeed BHs. The unequivocal smoking gun of a BH is its shadow and one is yet to be detected. The BH candidates might be a compact configuration without an event horizon, made of some type of exotic matter, although such an hypothesis is rather unlikely. For instance, there are indirect tests which suggest that BH candidates do not have a "normal" surface [3]. Also, signatures of a very compact synchroton-emitting region with size $\sim GM/c^2$, consistent with the BH scenario, have been reported for some cases [3, 40]. Still these are by no means a direct evidence for the existence of a BH.

The most promising candidates for a shadow observation are by far the supermassive BHs at the centers of the Milky Way (Sgr A*) and the giant elliptical galaxy M87 [40, 41]. The Sgr A* has a mass of $4.3 \times 10^6\, M_\odot$ and is at a distance of 8.3 kpc from Earth. The M87's BH (or M87 for short) is considerably further away, almost 17.9 Mpc from Earth, but is also much more massive, with a mass of about $6.6 \times 10^9 M_\odot$ [41]. So both shadows have an expected angular diameter[1] of the same order of magnitude, about $\simeq 50\mu$as for Sgr A* and $\simeq 40\mu$as for M87 (as seen from Earth) [40]. These angular scales are already accessible within existing techniques, namely the Very Long Baseline Interferometry (VLBI) operating at millimeter and sub-millimeter wavelengths (0.8 mm - 1.3 mm). This frequency range is favored due to synchroton radiation, which peaks at this interval in Sgr A* and is expected not to be self-absorbed, allowing the horizon scales to be resolved [42, 43]. Moreover, longer wavelengths are dominated by interstellar scattering, which

---

[1] A Kerr shadow's angular diameter is of the order $\simeq 10GM/(lc^2)$, where l is the distance to the BH (for very distant observers!).

overcomes the source structure.

At the moment, with VLBI it is possible to have angular resolutions of the order $\sim 20-30\mu$as, already within the scale necessary to examine phenomena in the accretion disk [41]. Since 2003 sporadic flares in Sgr A* have been detected with a quasi-periodic structure in a typical time scale of 20 min, each lasting $\sim$ 2h [44]. These flares can potentially be explained within the hot spot model, in which density inhomogeneities in the accretion disk orbit the BH at horizon scales [45]. It has been suggested that the fastest periodicity can be used to constrain the possible value of the BH spin, since the period of the Innermost Stale Circular Orbit[2] (ISCO) is rather dependent on that quantity [46]. For instance, for Sgr A* the period timescale of the ISCO ranges from 30 min up to 4 min (in prograde orbits), as the spin is increased from zero to its maximum.

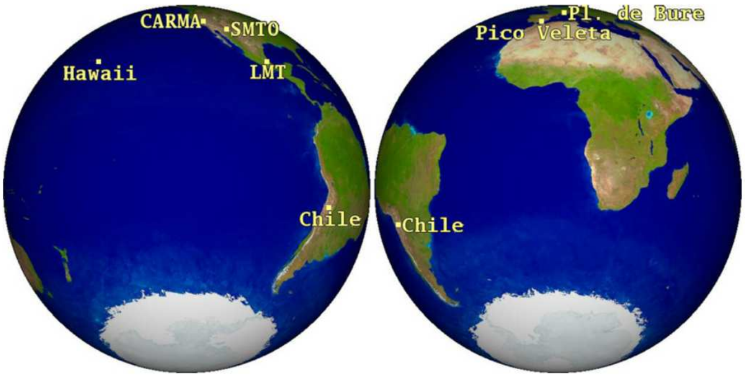

Figure 2.1.1: Location of possible VLBI telescopes of the EHT project as observed from Sgr A*. Adapted from [46].

Despite these recent advances, the detection of a BH shadow is still one of the main goals of VLBI observations. To meet this end, an international project named Event Horizon Telescope (EHT) is being developed [41,42,46]. It aims to produce high quality images of shadows using an array of VLBI telescopes scattered across planet Earth. In addition to upgrading existing telescopes in Hawaii, Chile, Greenland, Spain, France, USA, and the South Pole it has also been considered the possibility of including new ones in Mexico, South Africa, Kenya and New Zealand (see Fig. 2.1.1) [42, 46]. In clear contrast with centimeter wavelength astronomy, (sub)millimeter observations are limited by the requirement that the operating station must be above most of the water vapor in the atmosphere. Therefore possible sites

---

[2] ISCO is the closest stable orbit around a BH for time-like particles.

suitable for mm VLBI astronomy are quite sparse [46].

In addition to the EHT, there are plans for another international project, still in the preliminary design phase, designated GRAVITY [44]. It is “specifically designed to observe relativistic motions of matter” and aims to test General Relativity (GR) in the strong field regime for an extremely heavy mass [44, 47]. Near-infrared light from four telescopes of ESO’s Very Large Telescope will be interferometrically combined, measuring angular distances between a reference star and a target object up to an accuracy of 10μas [44]. Such a high precision tool will allow direct measurement of on-sky motion of objects, such as stars very close to Sgr A* and the previously mentioned flares at horizon scales. The analysis of relativistic effects and the testing of possible deviations from GR predictions makes the name GRAVITY a certainly suitable name for the project.

It is important to mention that GRAVITY will not actually resolve shadows. It is much more focused on a more dynamical picture of gravitational phenomena. This comes in clear contrast with the EHT, since for the latter are also expected much longer exposure times than the typical orbital periods in Sgr A* at horizon scales [41, 44].
Besides the galactic center, GRAVITY might also play a role in the search for Intermediate Mass BHs, with mass ranging between stellar BHs and supermassive BHs. Although they are expected to be found in dense star clusters, none has been confirmed to this date [3, 47]. GRAVITY also promises to be an ideal tool to investigate young stellar objects, namely forming planets in circumstellar disks [47].

2.2 Brief introduction to “hair”

Up to this point only Kerr BHs were considered in the discussion and so it is reasonable to ask if other types of BHs might exist in the cosmos. For the remainder of this chapter units $G = 1$ and $c = 1$ will be used.

2.2.1 Uniqueness Theorems and the No-hair conjecture

A set of influential theorems by Israel, Carter and Wald that became known as the *uniqueness theorems* establish that all stationary BHs in **vacuum**[3] which are regular and asymptotically flat are given by the Kerr metric (Kerr-Newman if electric charge exists) [48, 49]. The underlying assumptions are

---

[3] Of course many other solutions are possible for BHs which are not in vacuum.

fairly reasonable, namely that the cosmic censorship conjecture holds and the space-time outside the event horizon is free of closed time-like loops, which would violate causality [50]. A direct consequence of the uniqueness theorems is that BHs in vacuum are totally described by their total mass M and angular momentum J (and electric charge if present, which will not be considered). This implies that two BHs with the same M and J are *identical*, which comes in clear contrast with other celestial bodies such as stars that cannot be fully characterised by only two quantities. During the formation of a BH, any residual information other than the mass and spin of the original system must then be radiated away, namely through gravitational radiation [51].

The uniqueness theorems inspired the conjecture that the dynamical endpoint of gravitational collapse in the presence of any type of matter-energy configuration is given by the Kerr metric [52], described only by the final mass and angular momentum. This extrapolation was captured in John Wheeler's[4] mantra "BHs have no hair", where *hair* is a metaphor for other BH parameters needed to fully describe the BH. This is the *no-hair conjecture*, immensely influential in BH physics and often regarded as a theorem, although it is not proven [48, 52]. Notice that the no-hair conjecture is a much stronger statement than the uniqueness theorems since it concerns the outcome of gravitational collapse and not just the existence of BH solutions in equilibrium with a matter-energy field.

The Einstein equations are highly nonlinear and therefore it is not always possible to solve them using an expansion of orthonormal polynomials. However, it has been shown that a multipole expansion of curved space-time does exist [50].

The first two multipole moments of a BH can be identified as the mass M and the angular momentum J. If the no-hair conjecture holds, then all higher multipole moments, namely the quadropole moment, must be exclusively dependent on those two quantities. Possible observations that could test this conjecture have already been designed, namely in a series of papers by Johannsen et al. [28, 45, 50, 51, 54, 55]. In these papers a perturbed version of Kerr with an independent quadropole moment, dubbed "quasi-Kerr" metric, is considered. This quasi-Kerr metric is only a solution to the Einstein equations up to quadropole order and reduces smoothly to Kerr [50]. Using this approach one concludes that even moderate deviations from the Kerr metric lead to measurable deformations of the BH shadow, which could potentially be observed by the EHT.

---

[4] John Wheeler is also credited for coining the names "black hole" and "wormhole". He would allegedly lay "in a warm bath for hours on end, letting his mind soar in a search for just the right word or phrase". [1, 53].

With the advent of high resolution VLBI techniques and international projects such as the EHT and GRAVITY, researchers hope to discover within the next few decades if BH candidates in the cosmos are really the paradigmatic Kerr BHs suggested by the no-hair conjecture. It is therefore timely to explore alternative BH solutions from which templates can be built for the upcoming astronomical data [56].

In physics, scalar[5] fields are probably one of the simplest descriptions of matter and so it should come as no surprise that one might search for BH solutions coupled with scalar fields. The discovery in 2012 of a scalar particle in the Large Hadron Collider (at CERN), identified as the Higgs boson, suggests that fundamental scalar fields do exist in Nature. Furthermore, these fields can also be used as a toy model for realistic matter, such as dark matter [52]. Moreover, scalar fields are motivated as well from high energy theories beyond the standard model, namely from string theory [56].

A *no-scalar-hair theorem* by Chase established that a BH cannot support in equilibrium a static, regular and massless scalar field. Bekenstein also proved a (different) no-hair-theorem that became influential, which could be extended to massive scalar fields as well [52]. A generalization of the original proof can be found in Appendix B.1 for a stationary and axi-symmetric BH interacting with a scalar field ϕ. This theorem makes three crucial assumptions:

- The scalar field is minimally coupled to Einstein's gravity, or in other words, the field equation for ϕ does not involve the curvature of spacetime. This assumption excludes non-minimally coupled interactions, such as scalar-tensor theories of gravity. The non-linearity of these exotic matter fields produces resistance to the collapse of the field into the BH. However they have probably little astrophysical relevance, at least at macroscopic scales. Nevertheless the existence of such solutions show there are limitations to the no-hair conjecture [52].

- The scalar potential $V(\phi)$, defined in Appendix B.1, satisfies $V'\phi \geq 0$, where the derivative is taken with respect to the field ϕ. A non-self interacting massive scalar field, probably the simplest case, satisfies this condition. However, there are physical potentials that can violate it, namely the Higgs potential. Nonetheless other types of no-scalar-hair theorems exist in similar circumstances, although they rely on the

---

[5] Scalar fields are defined by a single value at each point in space-time and are invariant by a local coordinate transformation [57].

(strong) weak energy condition, which state that the (potential) energy density is non-negative. Still, if the (strong) weak energy condition is itself broken, then hairy BH solutions are possible, albeit unphysical [52].

- The scalar field ϕ has the same symmetries as the space-time, namely $\partial_t\phi$ and $\partial_\varphi\phi$ are both zero. The coordinates t, φ are chosen such that the vectors ∂_t and ∂_φ are the two Killing vectors related respectively to the space-time stationary symmetry and to axial symmetry. This assumption appears quite obvious at first, but it is not compulsory. What is mandatory is that the energy-momentum tensor $T_{\mu\nu}$ of the scalar field has the same symmetries as the space-time, which is not equivalent. If the scalar field ϕ is complex, it can have a harmonic time dependence of the form $\sim e^{-iwt}$ that cancels out in the energy-momentum tensor. This loophole will be explored in the next sections.

2.2.2 Superradiance

Naively, one might expect that a wave scattered by a BH should always have a smaller (at most equal) amplitude than the incident wave. However surprisingly, it is possible in fact for the scattered wave to have a larger amplitude than the incident one, if certain conditions are met. This physical phenomenon called *superradiance* is the wave scattering analogue of the Penrose process. Indeed, the additional energy of the scattered wave is only possible at the expense of the BH rotational energy [1, 58].

It is interesting to reproduce here an impressive thermodynamic argument, that can be found in Novikov's book [1], which leads to the superradiance condition. The formulation of BH thermodynamics has curiously quite a familiar form. For instance the 1^{st} law of BH thermodynamics is given by [1]:

$$dM = \frac{\kappa}{8\pi}dA + \Omega_H dJ,$$

where M, A, J, κ are respectively the mass, area, angular momentum and surface gravity of the BH [5] (there is a small discussion about the event horizon's angular velocity Ω_H for Kerr in Appendix A.1). The thermodynamic analog of this expression is

$$dE = TdS - PdV,$$

where E, T, S, P, V are respectively the energy, temperature, entropy, pressure and volume of a given thermodynamic system. The similarity between both expressions is closer than one might think, since the area of the horizon

A is indeed proportional to the entropy of the BH and the surface gravity κ is proportional to a temperature, related to the famous Hawking radiation. It follows naturally that the BH analog for the 2^{nd} law of thermodynamics is given by

$$dA \geq 0.$$

This relation, proven by Hawking in 1971, implies that in any process the area of the BH cannot decrease [5].

Consider now a bosonic field $\phi \sim e^{-i(wt-m\varphi)}$ with quantum numbers[6] w, m that could describe a scalar, electromagnetic or gravitational wave [1]. Far from a BH, each quanta has an energy $\delta E = \hbar w$ and an axial angular momentum $\delta J = \hbar m$, where $h = 2\pi\hbar$ is the Planck constant. Thus the flux ratio of the angular momentum and energy of the field ϕ across a large sphere surrounding the BH is given by $\delta J/\delta E = m/w$ (this argument can be made precise [1]). An interaction of the scalar wave with the BH will then lead to a change of mass δM and angular momentum δJ of the latter:

$$\delta J = \frac{m}{w}\delta M.$$

By the 1^{st} and 2^{nd} law of BH thermodynamics (and since $\kappa \geq 0$), we must have

$$\delta M - \Omega_H \delta J \geq 0,$$

which combined with the previous equation leads to

$$\left(1 - \Omega_H \frac{m}{w}\right) \delta M \geq 0.$$

For superradiance to occur, energy must be extracted from the BH. Thus $\delta M < 0$ and one must have

$$\boxed{w < m\Omega_H.}$$

An interesting situation happens for exactly $w = m\Omega_H$, since it will lead to bound states between the BH and a scalar field (this topic will be continued ahead).

It can be found that the maximum amplification of an incoming wave due to superradiance is $0.3\%, 4.4\%$ and 138% respectively for scalar, electromagnetic and gravitational waves (the main reason for this difference is the quantum spin of the field) [1]. Superradiance has also been equally predicted for other types of fields, such as massive vector fields defined by the Proca equation [59, 60]. With this in mind, one can conceive an interesting

---

[6] Until the end of this chapter a different notation is used: M is the BH mass, m is the azimuthal harmonic index and w is the field frequency.

academic paradigm, namely a reflecting mirror surrounding a BH. The wave would then bounce back and forth between the mirror and the BH, with the wave's amplitude being exponentially augmented in each iteration. Such a device is called a *"BH bomb"* [58, 59, 61].

Although the construction of such an apparatus is very unlikely, nature sometimes provides its own mirrors [58]. For instance, a proposed mechanism for astrophysical gamma-ray bursts involve magnetosonic plasma waves suffering multiple reflections on the inner boundary of an accretion disk, which is orbiting a BH. The enormous amount of energy released by supperradiance amplification is then collimated into an outburst of gamma radiation. The mass μ of a scalar field also works effectively as a mirror, as long as the condition $w < \mu$ is fulfilled [58].
See [62] for a (much more complete) review on superradiance.

2.2.3 Massive scalar clouds

We will now focus on a massive scalar field ϕ on the background space-time of a Kerr BH. This means that ϕ is a probe field, not massive enough to "back-react" on the geometry. For this reason, the field ϕ is usually dubbed a "scalar could", since it does not truly qualifies as "hair" [63].

Considering the massive Klein-Gordon equation on the Kerr space-time, we have

$$\nabla_\nu \nabla^\nu \phi - \mu^2 \phi = 0,$$

where μ is the mass of the scalar particle[7], if units $G = c = \hbar = 1$ are used. Notice that $1/\mu$ has dimensions of a distance, defined by the Compton wavelength of the particle [64] . Also, the metric information of the space-time is contained on the covariant derivative operator $\nabla^\nu = g^{\mu\nu}\nabla_\mu$.

To solve the Klein-Gordon equation, the field ϕ is decomposed in its modes $\phi = \sum_{l,m} \phi_{lm}$, and separation of variables are used:

$$\phi_{lm} = R_{lm}(r) S_{lm}(\theta) e^{-iwt} e^{im\varphi}.$$

In the previous expression $\{t, r, \theta, \varphi\}$ are the Boyer-Lindquist coordinates and S_{lm} are the spheroidal harmonics, which satisfy the equation (see [63, 65])

$$\frac{1}{\sin\theta}\frac{d}{d\theta}\left(\sin\theta\frac{dS_{lm}}{d\theta}\right) + \left(K_{lm} + a^2(\mu^2 - w^2)\sin^2\theta - \frac{m^2}{\sin^2\theta}\right) S_{lm} = 0.$$

---

[7] In S.I. units we have $\mu = c\mu^*/\hbar$, where μ^* is the particle mass [64].

The spheroidal harmonic index l has the range $-l \leq m \leq l$, where m is the azimuthal harmonic index; both l and m are integers [63]. The term K_{lm} is simply a separation constant. The radial functions R_{lm} are given by the Teukolsky equation [49, 63, 65]:

$$\frac{d}{dr}\left(\Delta \frac{dR_{lm}}{dr}\right) - \left(a^2 w^2 - 2maw + \mu^2 r^2 + K_{lm} - \frac{\left[(r^2+a^2)w - am\right]^2}{\Delta}\right) R_{lm} = 0,$$

where $\Delta = r^2 + a^2 - 2Mr$ and a is the spin of the Kerr BH, as before. Notice that in this chapter a different notation is used for the BH mass M, which is not to be confused with m, which is now the azimuthal harmonic index. Also, an non-negative integer index n can be introduced, which counts the number of nodes of the radial function R_{lm}. Curiously enough, the mathematical structure of this solution does resemble the familiar analysis on atomic orbitals. However it does not share the probabilistic character of the latter [65].

In the search for bound states one must impose physical boundary conditions, namely purely ingoing scalar waves at the BH horizon (as measured by a comoving observer) and an exponentially decaying profile at spatial infinity [63,65]. Applying these conditions, a set of possible ressonance frequencies $\widetilde{w}$ can be obtained, resembling an eigenvalue problem [63]. However, it turns out that $\widetilde{w}$ are *complex* numbers, which means they generally correspond to quasi-bound states. Decomposition on the real and imaginary parts of $\widetilde{w}$ yields

$$\widetilde{w} = \mathcal{R}(\widetilde{w}) + i\,\mathcal{I}(\widetilde{w}).$$

So for ϕ_{lm} we obtain a harmonic time dependence of the form

$$\phi_{lm} \sim e^{-i\,\mathcal{R}(\widetilde{w})t}\, e^{\mathcal{I}(\widetilde{w})t}.$$

We have then three different scenarios. From a more detailed analysis (see [58, 63, 65]) it is possible to conclude that:

- $\mathcal{I}(\widetilde{w}) < 0$, for $\mathcal{R}(\widetilde{w}) > m\Omega_H$. In this regime the field decays exponentially with time, and thus it is infalling into the BH. This case is the only one present for Schwarzschild BHs (no rotation), which is in agreement with well known no-scalar-hair theorems for static hair [63].

- $\mathcal{I}(\widetilde{w}) > 0$, for $\mathcal{R}(\widetilde{w}) < m\Omega_H$. This is the superradiant regime, in which the field amplitude increases exponentially with time. Notice however, that this situation cannot be sustained indefinitely, since Ω_H also decreases as the BH's rotational energy is extracted due to superradiance. Moreover, above a certain energy level, the field starts to back-react on the space-time geometry and the initial assumption is no longer valid.

- $\mathcal{I}(\widetilde{w}) = 0, \quad$ for $\widetilde{w} = m\Omega_H$. This limit of the superradiant regime yields the true bound states of scalar clouds, for a (infinitely) long-lived solution [66].

Fixing the values of l, m, n, the possible scalar cloud solutions with $w = m\Omega_H$ follow an *existence line* in the (M, J) parameter space of Kerr BHs. For instance, in Fig. 2.2.1 are displayed several existence lines for different values of m in a $M(\Omega_H)$ diagram, fixing $l = m$ and $n = 0$ (fundamental modes). Since scalar clouds lie at the threshold of the superradiant regime, points to the right of each existence line in the $M(\Omega_H)$ diagram correspond to Kerr space-times which exhibit superradiant instabilities against those clouds [49, 65]. In other words, if a given scalar cloud configuration in an existence line is "relocated" to a Kerr space-time to the right of its initial position in the diagram, the cloud would be come unstable due superradiance. Moreover, since existence lines with $l > m$, $n = 0$ lie to the right of the fundamental mode $(l = m,\ n = 0)$, the latter also defines the threshold of instability for a given m [65]. This means that although each mode in its existence line is stable *per se* with respect to superradiance, a combination of different modes is not. For this reason only scalar clouds with $l = m$ will be promoted to hair in the next section, in the full Einstein-Klein-Gordon system [49].

As a final remark, since scalar clouds in equilibrium can only lie along existence lines, one might expect that these solutions are unstable with respect to perturbations. However it is plausible that clouds are in fact dynamical attractors [65]. For instance, given a BH with a scalar field, if $w > m\Omega_H$ then the field will transfer mass and angular momentum to the BH, resulting respectively in an increase and decrease of the values of Ω_H and w. The opposite situation occurs for $w < m\Omega_H$, in which the field retrieves energy and angular momentum from the BH due to superradiance, leading to an increase of w and to a decrease of the angular velocity Ω_H of the BH. The bound state $w = m\Omega_H$ can then be regarded as the situation in which the field and the BH are in a synchronous rotation state.

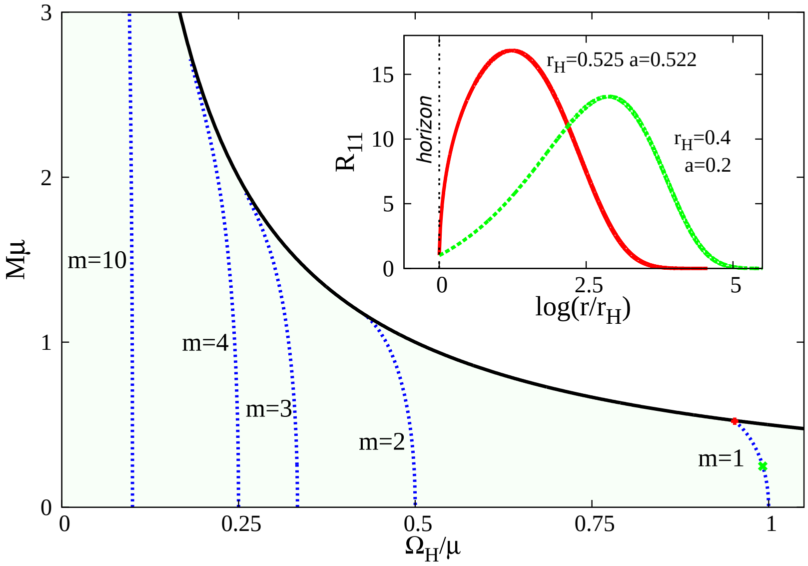

Figure 2.2.1: Graph of the Kerr parameter space of solutions in a M versus Ω_H diagram. Examples of existence lines of scalar clouds are displayed for different values of m ($l = m$ and $n = 0$). The solid black curve corresponds to extremal BHs and all Kerr BHs solutions exist below it (shaded region). *Inset*: The function $R_{11}(r)$ is displayed for two different clouds, identified in the right of the $M(\Omega_H)$ diagram as the green and red dots. The r scale starts at $r = r_H \equiv r_+$ and the function R_{11} is normalized such that $R_{11}(r_H) = 1$ for both clouds. The values of a and r_H are in units of $1/\mu$. Figure adapted from [49].

2.3 Hairy BHs with scalar hair

The well known no-scalar-hair theorems previously discussed led to the widespread belief that regular BH solutions with scalar hair were not possible, unless the "hair" was anchored to non-linear interactions, for which case solutions have been shown to exist. However these have questionable astrophysical relevance.

Nevertheless, a novel family of BH solutions was recently found [49], dubbed *Kerr BHs with Scalar Hair* (KBHsSH), which can potentially be more relevant in astrophysics. In these solutions, the massive scalar hair does not rely either on non-linear matter effects or self-interactions as means to sustain itself against gravitational collapse into the BH. Instead, these Hairy BHs (HBHs) are the non-linear generalization of scalar clouds for a back-reacting scalar field, and hence made possible by superradiant instabilities. Also, the harmonic dependence makes it possible for these solutions to be outside the scope of the mentioned no-hair theorems. A detailed review for these solutions can be found in [56], which will also be strongly followed in this section.

Consider a complex massive scalar field ϕ minimally coupled to Einstein's gravity. Instead of a complex field, it is also equivalent to consider two real fields in opposite phases. Both the Einstein equations and the field equation for ϕ can be obtained from the Hilbert functional $\mathcal{S}[g_{\mu\nu}, \phi]$ by the variational principle:

$$\mathcal{S}[g_{\mu\nu}, \phi] = \int d^4x\sqrt{-g}\left[\frac{R}{16\pi} - \frac{1}{2}\nabla_\mu\phi\nabla^\mu\phi^* - \mu^2\phi^*\phi\right],$$

where g is the determinant of the metric, R is the Ricci scalar, μ is the mass of the scalar particle (not to be confused with the index) and ϕ^* is the complex conjugate of the field ϕ. One can then obtain the Einstein equations and the massive Klein-Gordon equation for the field ϕ:

$$R_{\mu\nu} - \frac{1}{2}g_{\mu\nu}R - 8\pi T_{\mu\nu} = 0,$$

$$\nabla_\mu\nabla^\mu\phi = \mu^2\phi,$$

where the expression for energy-momentum tensor is given by [56]:

$$T_{\mu\nu} = \nabla_\mu\phi^*\nabla_\nu\phi + \nabla_\nu\phi^*\nabla_\mu\phi - g_{\mu\nu}\left[\frac{1}{2}\nabla_\alpha\phi\nabla^\alpha\phi^* + \mu^2\phi^*\phi\right].$$

The action is invariant by a global $U(1)$ transformation $\phi \to e^{i\beta}\phi$, where β is a constant. This symmetry yields a conserved quantity, a *Noether charge* Q, consequence of the conservation of the scalar 4-current [56]. Thus, the charge[8] Q, which counts the number of particles in the scalar field, follows a continuity equation. This does not forbid however charge flux into a BH. Moreover, charge loss would leave no signature on the BH exterior since Q does not follow a Gauss law.

The following ansatz for a stationary and axial-symmetric metric is now made:

$$ds^2 = e^{2F_1}\left(\frac{dr^2}{N} + r^2d\theta^2\right) + e^{2F_2}r^2\sin^2\theta(d\varphi - Wdt)^2 - e^{2F_0}Ndt^2, \quad (2.3.1)$$

where $N = 1 - r_H/r$ and r_H is the radial coordinate of the BH event horizon. The ansatz for the scalar field is given by

$$\phi = \widetilde{\phi}(r,\theta)e^{i(m\varphi - wt)},$$

---

[8] Q has absolutely no relation with the electric charge!

where w is the field frequency and m is an integer named azimuthal harmonic index. Notice that the coordinates used $\{t, r, \theta, \varphi\}$ are **not** Boyer-Lindquist coordinates, although there is a close connection between the two sets (see Appendix A of reference [56]). The physical interpretation however is still the same for each coordinate, as the notation suggests. Also, $\widetilde{\phi}$ and the metric functions F_0, F_1, F_2, W only depend on r and θ due to the assumed symmetries for the space-time. Moreover, all the solutions analysed in reference [56] are symmetric with respect to a reflection on the equatorial plane, so it is enough to consider the range $\theta \in [0, \pi/2]$. Furthermore, since this is a non-linear setup, it is not clear that the function $\widetilde{\phi}$ can be decomposed in a product of radial and angular functions, as was done in the analysis for scalar clouds.

Although the metric has two Killing vectors, namely ∂_t and ∂_φ, the full solution (space-time plus scalar field) does not. The latter has only one Killing vector, expressed by the helicoidal vector field

$$\chi = \partial_t + \frac{w}{m}\partial_\varphi.$$

It is important to clarify that (remarkably) the space-time is still stationary and axial-symmetric, since the harmonic dependence in the field cancels out in the energy-momentum tensor. The latter will depend however on m and w, and so will the space-time geometry.

The Einstein-Klein-Gordon system yields an impressive set of five non-linear coupled partial differential equations for the functions F_0, F_1, F_2, W and $\widetilde{\phi}$, which was solved numerically (see [56] for details). Two remaining Einstein equations were also used both as constrains and as a numerical accuracy check. The relative error of the solutions found was estimated to be less than 10^{-3}.

For the boundary conditions, it was required that on the axis of rotation ($\theta = \{0, \pi\}$):

$$\partial_\theta F_i = \partial_\theta W = \widetilde{\phi} = 0, \quad \text{and} \quad F_1 = F_2,$$

where the last equality prevents conical singularities. Due to reflection symmetry on the equatorial plane ($\theta = \pi/2$), one should also have

$$\partial_\theta F_i = \partial_\theta W = \partial_\theta \widetilde{\phi} = 0.$$

In addition to these boundary conditions, the solution was also required to be asymptotically flat:

$$\lim_{r\to\infty} F_i = \lim_{r\to\infty} W = \lim_{r\to\infty} \widetilde{\phi} = 0.$$

The boundary conditions for F_i and $\widetilde{\phi}$ at the event horizon are not so clear; they can be obtained by a series expansion near the horizon $(r = r_H)$, using a new radial coordinate $x = \sqrt{r^2 - r_H^2}$:

$$\partial_x F_i = \partial_x \widetilde{\phi} = 0.$$

Still at the horizon, the boundary condition for the function W is given by:

$$\Omega_H = W_{(r=r_H)} = \left(\frac{w}{m}\right),$$

which comes naturally as a generalization of the synchronous rotation condition discussed for scalar clouds, and it is thus related to superradiance. Also, this guarantees that the horizon surface is a Killing horizon, since the normal to that surface is a combination of the Killing vector fields, which in this case is only χ [1]. This further implies that the flux of the scalar field into the BH is zero, a necessary result for an equilibrium configuration:

$$\chi^\mu \partial_\mu \phi = \chi^t \, \partial_t \phi + \chi^\varphi \, \partial_\varphi \phi, \tag{2.3.2a}$$

$$= - iw\phi + \left(\frac{w}{m}\right)(im)\phi = 0. \tag{2.3.2b}$$

For the numerical integration itself, the input parameters used in reference [56] were $\{w, m, r_H\}$, where with no loss of generality was set $w > 0$. Quantities of physical relevance are then infered posterioreley from the solution, namely M, J, Q and n, where the latter is the number of nodes in the equatorial plane for the function $\widetilde{\phi}$, reminiscent of the integer n defined for scalar clouds. A reasonable and covariant definition of the mass M and angular momentum J of the system is actually not obvious. When considering asymptotically flat space-time, which is the case, the mass M and angular momentum J of the solution are read from the asymptotic expansion of the metric at spatial infinity:

$$g_{tt} = e^{2F_2} \, W^2 r^2 \sin^2\theta - N e^{2F_o} \simeq -1 + \frac{2M}{r} + \cdots ,$$

$$g_{t\varphi} = -e^{2F_2} \, W r^2 \sin^2\theta \simeq -\frac{2J}{r} \sin^2\theta + \cdots .$$

The quantities M and J are then referred to as *ADM quantities*, after Arnowitt-Deser-Misner [1,65]. It is worth mentioning that, up to this point, the mass and angular momentum of a BH system were always ADM values, and that the ADM definition also includes mass and angular momentum contained in possible fields around the BH (if present). For instance, in Kerr, which is a solution in vacuum, all the mass/energy is contained in the BH itself. However for HBHs this is no longer the case, since M also contains the mass/energy of the field. Thus, the ADM mass M can be interpreted as the total mass of the system, with all its components. Nevertheless, the intrinsic mass and angular momentum of a BH, excluding contributions from an exterior field, can still be computed using the Komar integrals over the horizon [56]; these will be referred to as *horizon quantities*.

A very interesting feature of these HBH solutions is that they make a continuous connection between Kerr BHs (plus scalar clouds) and another well known class of objects known as *Boson Stars* (BSs). A Boson Star (BS) is a self-gravitating configuration of a complex scalar field in equilibrium. It is a “macroscopic quantum state” since the gravitational collapse is prevented by Heisenberg’s uncertainty principle and also by the dispersive wave character of the scalar field [56, 66]. Moreover, BSs have been considered as possible alternatives when considering either BH or dark matter candidates, since BSs are also extremely compact objects. Is interesting that the metric ansatz for BSs is almost identical as the one used for HBHs, only this time with $r_H = 0$, since BSs do not have an event horizon. It is also intriguing that although both spherical and rotating BSs solutions are known in literature, only the latter can be continuously connected to HBH solutions. Part of the reason for this is that Schwarzschild BHs cannot support a scalar field in equilibrium [66]. A review on BSs can be found on [67, 68].

To better translate this continuous connection, it is useful to introduce a normalized Noether charge q, defined in [56] as

$$q = \frac{mQ}{J},$$

where q has simply the range $q \in [0, 1]$. For instance, when $q = 0$ the HBH solution corresponds to a scalar cloud in Kerr space-time, whether for $q = 1$ we obtain a BS, since for the latter $J = mQ$. This leads to the perspective that a HBH is in fact a BS in equilibrium with a BH in its center, with the configuration being more BS like or BH like depending on the value of q.

At this point it is interesting to analyse the solution space of HBHs in a diagram $M(\Omega_H)$, similar to the one in Fig. 2.2.1. In Fig. 2.3.1 there is such a representation for $m = 1$ and $n = 0$, which has an interesting spiral fashion. The red line in this figure corresponds to BSs, the blue line to scalar clouds (which is the same as the $m = 1$ blue line in Fig. 2.2.1) and the green line to extreme[9] HBHs. The latter is still poorly understood, since the center of the spiral is numerically challenging to explore. As a consequence, a more sophisticated picture in the center of the diagram is not yet excluded [56]. Also, the black line in the figure establishes the upper boundary of Kerr BH

---

[9] Extreme HBHs are defined to have zero Hawking temperature, or equivalently zero surface gravity.

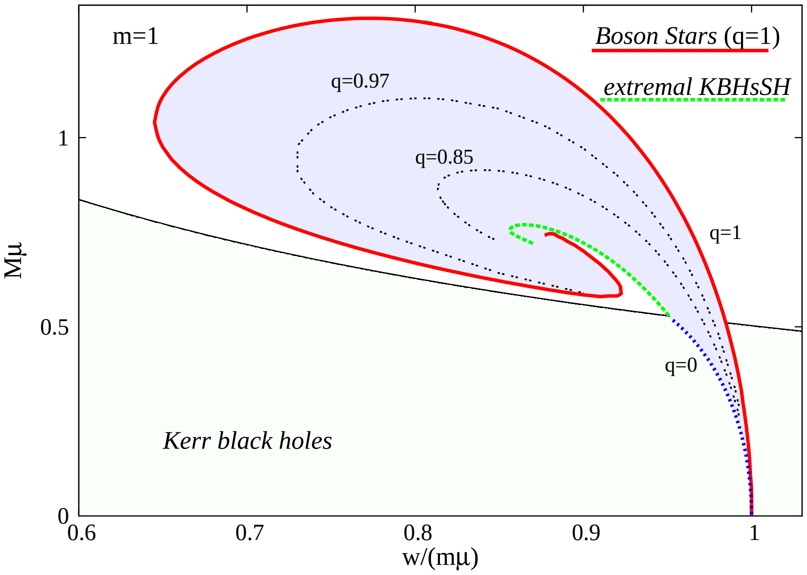

Figure 2.3.1: Domain of existence of the HBH family of solutions (bluish region) in a M versus $\Omega_H = w/m$ diagram, for $m = 1$ and $n = 0$. The solid black line sets the upper boundary of Kerr space-time solutions and corresponds to extremal Kerr BHs. Also, it is the same black line as in Fig 2.2.1. Additionally, the blue curve in this figure is the same as the $m = 1$ existence line in Fig 2.2.1 for scalar clouds. Adapted from [56].

solutions and it is the same black line as in Fig. 2.2.1. From this diagram one can then have a better understanding of the space of solutions of HBHs, which is given by the bluish region.

From reference [56] it is clear that HBHs can violate the Kerr bound ($M^4 \geq J^2$). Moreover, it turns out that some solutions can also violate this bound in terms of horizon quantities, rather than ADM [69]. In addition to this, there can be an overlap of HBH and Kerr BH solutions in parameter space. In other words, there exist HBHs and Kerr BHs with the same ADM quantities M and J. Since these are the only asymptotic parameters, as Q does not follow a Gauss law, there is non-uniqueness. Thus, as seen by a far observer, a HBH and a Kerr BH cannot be distinguished from one another just from the ADM quantities. To raise the degeneracy one must also specify q, since in reference [56] no distinct solutions with the same three parameters (M, J, q) were found.
In the region of non-uniqueness it is also interesting to compare the horizon surface area of HBHs and Kerr BHs with the same M and J (ADM). The intriguing conclusion is that the surface area, and thus the entropy, is always larger for HBHs that the corresponding Kerr BHs, and so, remarkably, this

implies that HBHs cannot decay adiabatically to the latter.

Notably, HBHs have appealing phenomenological properties, some of which are significantly different from those of Kerr BHs, which is an uncommon feature in alternative theories of gravity [56]. For instance, the quadropole moment, which can potentially be measured, can have deviations of more than one order of magnitude compared with Kerr. Likewise, the orbital frequency at the ISCO can suffer some moderate deviations, and the ergoregion of these HBHs also has some new features such as toroidal and Saturn like profiles (see [70]). For these reasons, the shadows of HBHs promise to reveal significant discrepancies with respect to Kerr, which will prove to be correct (see next section).

We will end this section with some remarks considering the particle mass μ of the scalar field. Consider a HBH configuration such that

$$M\mu = \eta .$$

The dimensionless quantity η makes the physical connection between the two length scales defined either by the gravitational radius or by the Compton wavelength of the scalar field.
Converting the last expression to S.I. units yields

$$\mathcal{M}\left(\frac{GM_{\odot}}{c^2}\right)\left(\frac{\mu\, c}{\hbar}\right) = \eta ,$$

where the dimensionless number $\mathcal{M}$ expresses the ADM mass in solar masses. Thus:

$$\mu = \frac{\eta}{\mathcal{M}} \times 1.32 \times 10^{-10}\, \mathrm{eV}/c^2 .$$

Since for the previously discussed solutions we have $\eta \sim 1$, then for a HBH with three solar masses ($\mathcal{M} = 3$) we obtain:

$$\mu \sim 10^{-11}\, \mathrm{eV}/c^2 ,$$

whereas if we choose the Sgr A* mass ($\mathcal{M} = 4 \times 10^6$):

$$\mu \sim 10^{-17}\, \mathrm{eV}/c^2 .$$

Scalar particles in this mass range are not known, or predicted within the context of the standard model of particle physics. However such extremely light particles have been suggested within more exotic theories, such as the string axiverse [49]. Nevertheless, these HBHs solutions can still be dynamically important for microscopic BHs, such as primordial BHs, although the laws of physics are still poorly understood on such scales.

2.4 Shadows of HBHs

This section contains a novel discussion, to the knowledge of the author, about the gravitational lensing produced by BSs and the shadows of HBHs (e.g. Kerr BHs with scalar hair). This recent family of solutions provides qualitatively and quantitatively new shadow templates that could be used by future VLBI observations and by the EHT. The content of this section and its main results were already submitted for publication [71].

2.4.1 Ray-tracing without Carter's constant

The general form of the geodesic equations is given by [8]:

$$\ddot{x}^\mu + \Gamma^\mu_{\alpha\beta}\,\dot{x}^\alpha \dot{x}^\beta = 0,$$

where the derivative is taken with respect to the affine parameter and $\Gamma^\mu_{\alpha\beta}$ are the Christoffell symbols. This set of second order differential equations does not assume any type of symmetries for the space-time. For Kerr, the geodesic equations (1.3.1 - 1.3.4) are first order, since symmetry integration constants $\{E, \Phi, Q, \tilde{\mu}\}$ are used. The constant E is related to the space-time stationary property, Φ to the axial symmetry and $\tilde{\mu}$ (here the mass of the moving particle) is connected to the normalization of the 4-momentum $\dot{x}^\nu$ (which is constant).

All these last symmetries are still valid for the previously discussed HBH space-times. However the Carter constant Q is specific for Kerr, consequence of an hidden symmetry[10], and generally does not exist. Thus, the geodesic equations for a HBH space-time are given by:

$$\ddot{r} + \Gamma^r_{tt}\,\dot{t}^2 + \Gamma^r_{rr}\,\dot{r}^2 + \Gamma^r_{\theta\theta}\,\dot{\theta}^2 + \Gamma^r_{\varphi\varphi}\,\dot{\varphi}^2 + 2\,\Gamma^r_{t\varphi}\,\dot{t}\,\dot{\varphi} + 2\,\Gamma^r_{r\theta}\,\dot{r}\,\dot{\theta} = 0, \qquad (2.4.1a)$$

$$\ddot{\theta} + \Gamma^\theta_{tt}\,\dot{t}^2 + \Gamma^\theta_{rr}\,\dot{r}^2 + \Gamma^\theta_{\theta\theta}\,\dot{\theta}^2 + \Gamma^\theta_{\varphi\varphi}\,\dot{\varphi}^2 + 2\,\Gamma^\theta_{t\varphi}\,\dot{t}\,\dot{\varphi} + 2\,\Gamma^\theta_{r\theta}\,\dot{r}\,\dot{\theta} = 0, \qquad (2.4.1b)$$

$$\dot{t} = -Eg^{tt} + \Phi g^{t\varphi}, \qquad (2.4.1c)$$

$$\dot{\varphi} = -Eg^{t\varphi} + \Phi g^{\varphi\varphi}, \qquad (2.4.1d)$$

where the last two equations are repeated for convenience. Defining the integration variables $z_r \equiv \dot{r}$ and $z_\theta \equiv \dot{\theta}$, one can then solve a system of six first order differential equations with a standard numerical method, such as Runge-Kutta. Interestingly, the initial conditions (1.5.31) are still valid for

---

[10] In fact, both E and Φ can be computed by multiplying the respective Killing vectors by the 4-momentum, which always yields a constant. The Carter constant is due to the existence of a Killing tensor, which yields Q after multiplication with the 4-momentum twice [8, 16, 21].

HBHs, given that the coordinate notation is re-interpreted as the one used in the HBH metric (2.3.1).

Usually, the normalization condition for the 4-momentum could be used to further reduce the number of second order differential equations from two to just one. For photons, $\dot{x}^\mu \dot{x}^\nu g_{\mu\nu} = 0$, which explicitly yields

$$\dot{t}^2 g_{tt} + \dot{\theta}^2 g_{\theta\theta} + \dot{r}^2 g_{rr} + \dot{\varphi}^2 g_{\varphi\varphi} + 2\,\dot{t}\,\dot{\varphi}\,g_{t\varphi} = 0.$$

However, solving this equation for either $\dot{r}$ or $\dot{\theta}$ would only supply information for the modulus of that respective component. Since the sign only changes at turning points, this approach could still be implemented in principle. Nevertheless, it is still easier numerically to solve instead the set of equations (2.4.1) (see also [72]).

The Christoffel symbols can be computed directly from the metric:

$$\Gamma^\mu_{\alpha\beta} = \frac{1}{2} g^{\mu\gamma} \left(\partial_\beta\, g_{\gamma\alpha} + \partial_\alpha\, g_{\gamma\beta} - \partial_\gamma\, g_{\alpha\beta} \right).$$

Using an algebra manipulation software such as *Maxima*, it is straight forward to obtain the Christoffel symbols from the metric (2.3.1), as function of F_0, F_1, F_2, W. The explicit expressions can be found in Appendix B.2.

The numerical values of the functions F_0, F_1, F_2, W are provided on a rectangular[11] grid in the (r, θ) plane (see [56] for details). In order to evaluate the Christoffel symbols at every point, one must be able to assign an approximate value for the functions F_i, W everywhere, and not only at the grid points. As a first approach, an engineered function was fitted to the data points using the least mean squared algorithm. The r and θ dependence was modulated respectively with a log-normal type function $h(x)$ and with a cosine function, within a good approximation.
The log-normal function $h(x)$ is given by

$$h(x) = \frac{A}{x-\gamma} \exp\left\{ -\frac{\left[\ln(x-\gamma) - q\right]^2}{2\sigma^2} \right\} + \varepsilon,$$

where $\{A, \gamma, q, \sigma, \varepsilon\}$ are fit parameters. The possibility to organize these parameters in a table (~ 70 for all 4 functions) is an advantage of this method. Although this approach was successfully implemented, interpolation is easier and more practical.

---

[11] Actually, the rectangular grid is not regular on the (r, θ) coordinates but rather on (x, θ), where x is the compactified radial coordinate: $x = \sqrt{r^2 - r_H^2} / \left(1 + \sqrt{r^2 - r_H^2}\right)$.

Two local interpolation methods were tested, namely bilinear and bicubic, which are standard in two dimensional problems [27]. A single function estimate requires information from 4 grid points for the bilinear method, or 16 points for the bicubic, in order to obtain local interpolation parameters. Since these parameters are different between rectangular grid elements, and a typical grid size is 250×29, the total number of interpolation parameters is clearly too large to tabulate. After some tests, it was concluded that the bilinear method was considerably faster than the bicubic, without suffering much accuracy loss. However, the partial derivatives are known to have discontinuities for a bilinear interpolated function. Thus, a smoothing algorithm for the derivative was also applied.

The ray-tracing paradigm which will be now considered is quite similar to the one in section 1.5.3, namely a celestial sphere concentric with a HBH and a non-centered observer inside the sphere (the observer is also in the equatorial plane). Similarly, the celestial sphere has twice the perimetral radius of the observer. However, the pattern chosen is different: a colored code is assigned to each quadrant of the celestial sphere. Additionally, a square grid is combined with the latter, with its lines uniformly spaced by 10^o both in the latitude and longitude (see Fig. 2.4.1). Moreover, a white spot (which center is dubbed point F) was added directly in front of the observer's line of sight. For this pattern configuration we closely follow an interesting paper on binary BH mergers [73]. Additionally, an image smoothing thecnique, also discussed on that paper, was applied to produce some high definition images. This thecnique envolves the construction of a 2000×2000 pixels image and then applying an averaging algorithm on the latter to build a smooth 500×500 image. However, due to reflection symmetry on the equatorial plane, $1000 \times 2000 = 2 \times 10^6$ photon trajectories need to be integrated in practice.

The analogous of Fig. 1.5.7, now with the new pattern, is given by Fig. 2.4.2. The apparent curvature of the grid lines is only related to the geometry of the projection.

It will be informative to compare observations in Minkowski, Kerr, and HBH space-times and so a similar observation criteria is necessary. Thus, recalling the discussion in section 1.5.3, different radial coordinates are equivalent if the perimetral radius $\tilde{r}$ is the same:

$$\tilde{r} = \sqrt{r_k^2 + a^2 + \frac{2ma^2}{r_k}} = r_h\, e^{F_2(r_h)},$$

where r_k and r_h are respectively the radial coordinates for Kerr and hairy BHs. The inversion relation $r_k(\tilde{r})$ has already been discussed in (1.5.32),

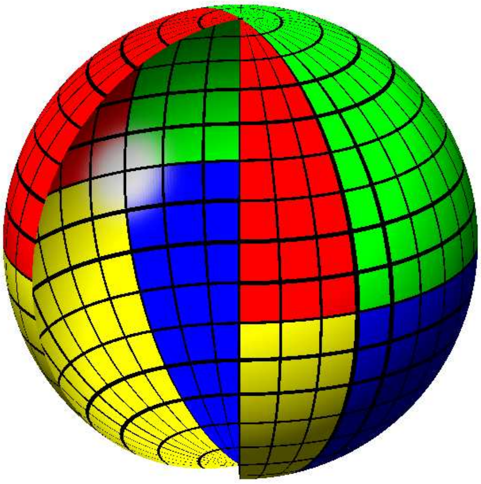

Figure 2.4.1: Graphical representation of the celestial sphere with a section removed in order to display its interior. The white spot on the inner surface is centered with the observer's line of sight. The perimetral radius of the celestial sphere is double the observer's, which is located on the equatorial plane.

whereas the relation $r_h(\tilde{r})$ is not known analytically and so it must be determined numerically. To meet this end, the bissection method was used [27]. Hence, given a value of $\tilde{r}$, one can obtain the equivalent radial coordinates between a Kerr BH and a HBH.

Still, as in section 1.5.3, a length scale must be provided to make the final link. When considering HBHs there are two distinct length scales available to serve as a unit of measurement, namely the Compton wavelength of the particle and the gravitational radius of the HBH. Thus, there are two different, and equally valid options, depending on which length scale is set constant throughout the analysis. One might for instance, compare HBH configurations with the same ADM mass M with the cost of changing μ, since the dimensionless product $M\mu$ typically varies between solutions. Changing μ only means that the type of particle is distinct, and hence we are comparing different *theories*. The other option is to fix the particle type and set μ constant, which implies that distinct solutions might have different ADM masses. This last option will be chosen when comparing BSs, whereas the previous is favored for configurations with an event horizon. Fixing M is indeed more appropriate to construct an observational template, since one wishes to compare different shadow predictions given a celestial object with a fixed ADM mass. Either case, the link between a HBH and a Kerr BH is only possible through the ADM mass of the latter, which has to be compared with a similar scale of the HBH. The most natural choice for this scale is the

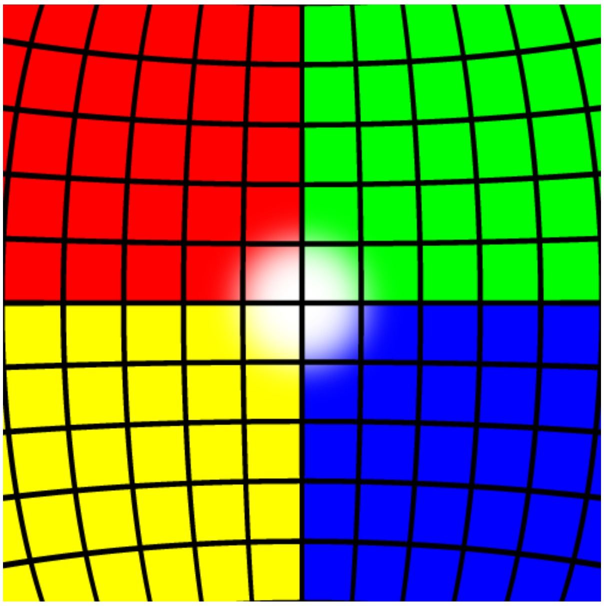

Figure 2.4.2: Observed pattern of Fig. 2.4.1 by an observer in flat space (Minkowski space-time). The apparent curvature of the grid lines is only related to the geometry. Notice the white spot, which is centered within the field of view. The range of the observation angles (α, β) (field of view) is $\pm \arctan(10/15)$.

HBH ADM mass, although the usage of horizon quantities is also possible.

2.4.2 Gravitational lensing of BSs

In this subsection, the pattern in Fig. 2.4.2 is gravitationally lensed by BSs. Since BSs do not possess an event horizon, no shadow will be observed. Spherically symmetric BS (SBS) are first addressed in Fig. 2.4.4, followed by Rotating BS (RBS) in Fig. 2.4.5. Although SBS are not continuously connected to the HBH family of solutions, they are important to understand the lensing structure of RBS. All BS solutions are labeled from 1 to 12 in Fig. 2.4.3, according to their position on the BS spiral curve in the solution diagram. These numbers will be displayed as indices of w [71]. Due to the spiral character of the BS curve, a single value of w does not define a solution unambiguously. Then, the curve is also divided into *branches*, each being bounded by spiral backbending points [56]. The branch number is represented as the superscript of w. For example, "$w_2^{(b1)}$" stands for the frequency of the BS solution 2, which also belongs to the first branch ($b1$).

We first look at the lensing due to SBSs (see Fig. 2.4.3, $m = 0$). We set the observer at the equator and always at the perimetral radius $\tilde{r} = 22.5/\mu$, with μ fixed for the different BS solutions. Moving along the SBS spiral and starting from vacuum (i.e. $w = 1\,\mu$), we find a set of "weak gravity" solutions: *non-compact* BSs, which have a size larger than the corresponding gravitational radius, regardless of any reasonable choice for the SBS effective radius. The BS with $w_1^{(b1)} = 0.95\,\mu$ in Fig. 2.4.4 illustrates such a case, where only a small distortion of the background is observed.

Moving further along the spiral, an Einstein ring appears at $w^{(b1)} \simeq 0.94\,\mu$, consequence of the lensing of F. Interestingly, a small region on the celestial sphere around F is duplicated and inverted inside the Einstein ring. This detail can be observed in Fig. 2.4.4 for a BS with $w_2^{(b1)} = 0.9\,\mu$. The appearance of the first Einstein ring defines the transition from non-compact to *compact* BSs.

Moving even further along the spiral, the region in the celestial sphere which is duplicated inside the Einstein ring becomes increasingly larger, as is illustrated for the BS with $w_3^{(b1)} = 0.8\,\mu$ in Fig. 2.4.4. Shortly after the spiral's first backbending (from the 1^{st} to the 2^{nd} branch), at $w \simeq 0.767\,\mu$, the full celestial sphere becomes duplicated, starting at the BS with $w^{(b2)} \simeq 0.77\,\mu$. Then, due to the lensing of the point immediately behind the observer (dubbed B), two further Einstein rings emerge, which can be observed in the bottom left panel in Fig. 2.4.4, for a BS with $w_4^{(b2)} = 0.8\,\mu$.

Progressing inside the spiral, additional pairs appear in between the previous two (new) Einstein rings. This can be seen in Fig. 2.4.4 for $w_5^{(b2)} = 0.84\,\mu$. Each new pair of Einstein rings is related to the alternate projection of either F or B in the image plane, and to a additional copy of the full celestial sphere.

Then, if spherical photon orbits and light rings are formed, one expects to obtain an infinite number of these copies, and a corresponding self-similar structure, marking the transition from compact to *ultra-compact* BSs. Indeed, photon orbits occur well inside the spiral, on the third branch (after the second backbending), starting at the BS solution with $w^{(b3)} = 0.842\,\mu$, marked as the blue star "LR" point on the $m = 0$ spiral of Fig. 2.4.3 [71].

We now analyse RBSs. Again starting from vacuum and following the BS spiral curve (this time with $m = 1$, see Fig. 2.4.3), we also find a region of non-compact BSs, i.e without multiple images. There are however important differences with respect to SBS, namely an asymmetric lensing, with an amplification of the side rotating away from the observer and a shift of the point F to the left, due to frame dragging. These effects are well illustrated in Fig. 2.4.5 for a BS with $w_6^{(b1)} = 0.95\,\mu$.

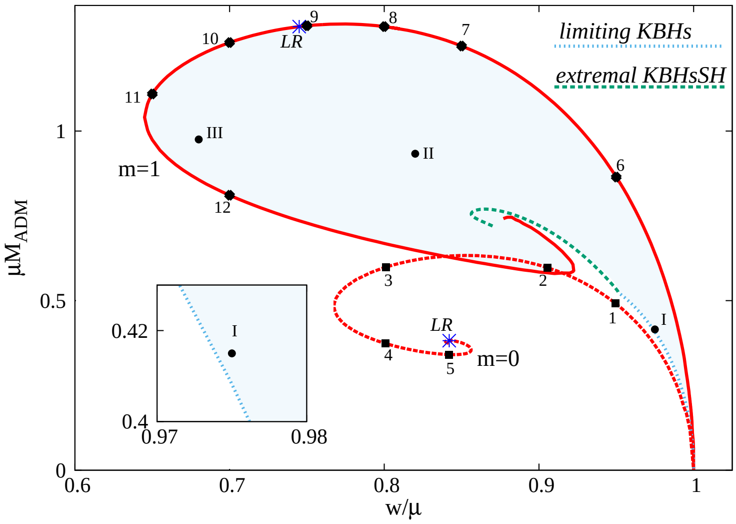

Figure 2.4.3: Location of some of the discussed solutions in parameter space. The red spiral with $m = 0$ and $m = 1$ are respectively the solution curve of SBS and RBS. BS are labeled with Arabic numerals, whereas configurations with event horizons are labeled with Roman numerals.

The set of compact rotating BS begins at $w^{(b1)} \simeq 0.92\,\mu$, since an Einstein ring appears for that configuration. In Fig. 2.4.5, this is also the case for the RBSs with $w^{(b1)}_{7,8}/\mu = \{0.85, 0.8\}$. The ring encloses again two inverted copies of part of the celestial sphere, but its shape is now elliptic-like. Additionally, the inversion shifts the image of point F inside the Einstein ring to the right.

Further following the spiral, new Einstein rings appear, just as in the case of SBSs, but instead of being circular they have a squashed "D-shape". An interesting example is the BS with $w^{(b1)}_{9} = 0.75\,\mu$, which is shown in Fig. 2.4.5. Then, at $w^{(b1)} \simeq 0.747$ a light ring emerges on the equatorial plane (see symbol "LR" in Fig. 2.4.3) [71]. Progressing even further through the spiral, multiple images of the celestial sphere are formed, presumably into a fractal structure, one might conjecture [71]. This point is illustrated by the BSs with $w^{(b1)}_{10,11}/\mu = \{0.7; 0.65\}$ and $w^{(b2)}_{12} = 0.7\,\mu$ in Fig. 2.4.5.

2.4.3 Examples of HBH shadows

We now analyse in this subsection shadows of HBHs. Since the Kerr bound can be violated both in terms of the ADM and horizon quantities, it is expectable that some HBH shadows will be significantly different from the Kerr ones. This expectation is indeed confirmed in Fig. 2.4.6, where the

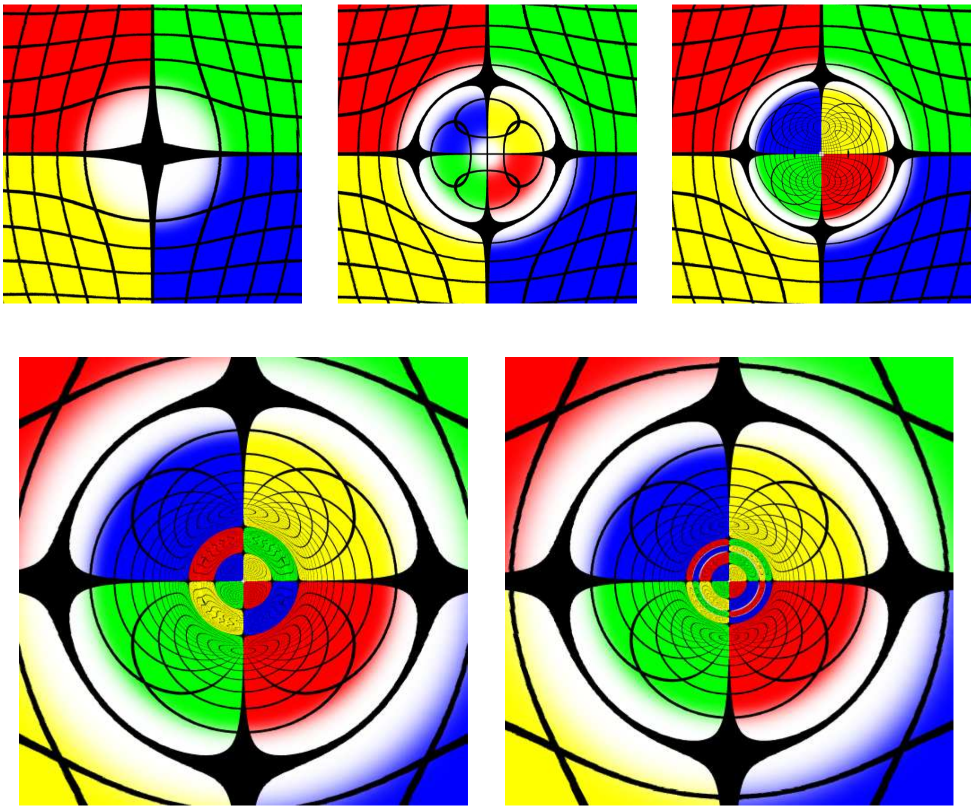

Figure 2.4.4: Examples of gravitational lensing of SBS. From left to right: (*first row*) $w^{(b1)}_{1,2,3}/\mu = \{0.95, 0.9, 0.8\}$; (*second row*) $w^{(b2)}_{4,5}/\mu = \{0.8, 0.84\}$. The field of view is $\pm\arctan(10/15)$ for the first row and $\pm 0.493\arctan(10/15)$ for the second row (the latter is zoomed). Notice that there is no shadow in the images.

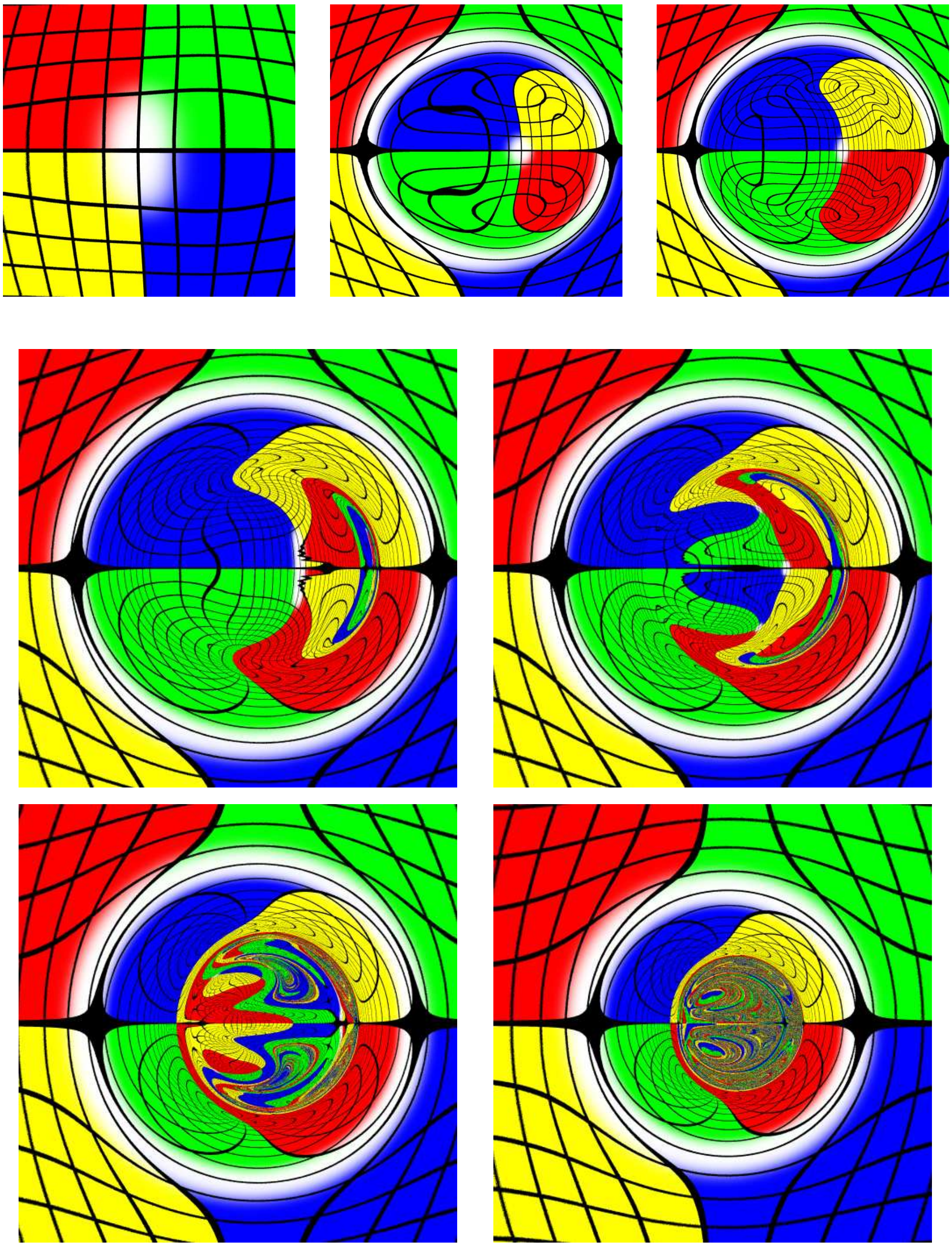

Figure 2.4.5: Examples of RBS. The rotation axis is given by the "up" direction in the paper surface. From left to right: (*first row*) $w^{(b1)}_{6,7,8}/\mu = \{0.95, 0.85, 0.8\}$; (*second row*) $w^{(b1)}_{9,10}/\mu = \{0.75, 0.7\}$; (*third row*) $w^{(b1)}_{11}/\mu = \{0.65\}$ and $w^{(b2)}_{12}/\mu = \{0.7\}$. The field of view is always $\pm\arctan(10/15)$. Notice that there is no shadow in the images.

shadows[12] and lensing effects of three HBHs are exhibited, together with comparable Kerr configurations. These three main examples are labeled by the Roman numerals I to III, and their position on the solution space can be found in Fig. 2.4.3. The physical quantities of the HBHs I – III are summarised as follows, where the labels ADM and H concern respectively ADM quantities and horizon quantities:

	$\mu\, M_{ADM}$	$\mu\, M_H$	$\mu^2\, J_{ADM}$	$\mu^2\, J_H$	$\frac{M_H}{M_{ADM}}$	$\frac{J_H}{J_{ADM}}$	$\frac{J_{ADM}}{M^2_{ADM}}$	$\frac{J_H}{M^2_H}$
I	0.415	0.393	0.172	0.150	95%	38%	0.999	0.971
II	0.933	0.234	0.739	0.114	25%	15%	0.849	2.08
III	0.975	0.018	0.85	0.849	1.8%	99.9%	0.894	2620

In this subsection the observer is always set at the perimetral radius $\tilde{r} = 15M$, in the equatorial plane, with the ADM mass M fixed, and at the equatorial plane. Also, the displayed Kerr shadows were computed using the full symmetries of Kerr space-time.
In Fig. 2.4.6 it is shown the shadow of configuration I (or shadow I for short). For this HBH only 5% of the total mass is contained in the scalar hair, and neither the ADM or the horizon quantities violate the Kerr bound, since $J_{ADM}/M^2_{ADM} < 1$ and $J_H/M^2_H < 1$. The similarity between shadow I and the shadow of a Kerr BH with the same ADM mass and angular momentum (Kerr$_{ADM}$ for short) is striking; but they are nevertheless distinguishable (see Fig.2.4.6). The shadow of the latter is in fact more D-like, since it is almost an extremal Kerr BH. However, shadow I is much more similar to the shadow of a Kerr BH with the same horizon quantities for the mass and angular momentum (Kerr$_H$ for short), as one can observe in Fig. 2.4.6, which is an interesting result.

Fascinatingly, shadows II and III in Fig. 2.4.6 yield novel shapes, with clear deviations from the corresponding Kerr$_{ADM}$ BHs. It is worth mentioning that for both cases $J_H/M^2_H > 1$, which means that the central BH is non-Kerr like. This is most apparent for configuration III, for which $J_H/M^2_H \sim 2 \times 10^3$, consequence of “heavy hair” dragging. Interestingly, the gravitational lensing of configuration III closely resembles the ultra-compact BS in Fig. 2.4.5 with $w^{(b1)}_{11} = 0.65\,\mu$. Moreover, shadow III is actually consisted by multiple disconnected regions, most of which much smaller that the largest “hammer-like” part, which points to a self-similar structure. Two “eyebrows” can indeed be easily observed above and below this main region at symmetric positions in Fig. 2.4.7. It is also interesting to understand the

---

[12] A light ray is considered to intersect with the event horizon when g^{tt} is ~ 1000 larger that its “typical” value.

transition from shadow II to shadow III, illustrated in Fig. 2.4.8.

As a final remark for this subsection, HBH shadows can be made arbitrarily small, since HBHs are continuously connected to BSs, which have no shadow. Also, the redshift, which depends only on the position of both the celestial sphere and observer, is constant throughout the images and has not been considered.

2.4.4 Shadow parameters

There are at least six possible parameters that could be used to distinguish and classify shadows, to be defined below. For the definition of these parameters we strongly follow a paper by Johannsen [28].
Consider a possible[13] shadow in Fig. 2.4.9, represented in the image plane of the observer and parametrized by the Cartesian coordinates (x', y'). The origin $(0, 0)$ of this coordinate system is defined as point O and corresponds to the direction pointing towards the center of the BH (local observation angles $\{\alpha, \beta\} = 0$), from the reader into the paper.

The point C in the figure, taken to be the center of the shadow, is such that its abscissa is given by:

$$x'_C = \frac{1}{2}(x'_{\rm max} + x'_{\rm min}),$$

where $x'_{\rm max}$ and $x'_{\rm min}$ are respectively the maximum and minimum abscissae of the shadow's edge. Since the observer is assumed to be in the equatorial plane, and due to reflection symmetry, C must be in the x' axis, which implies $y'_C = 0$. Since the points C and O need not to coincide, a specific feature of a shadow is the **displacement** $D_C = |x'_C|$ between the shadow and the center of the image plane O.

Other particular characteristics are both the **width** $D_{x'}$ and **height** $D_{y'}$ of the shadow, defined by:

$$D_{x'} = x'_{\rm max} - x'_{\rm min},$$

$$D_{y'} = y'_{\rm max} - y'_{\rm min},$$

where $y'_{\rm max}$ and $y'_{\rm min}$ are respectively the maximum and minimum ordinates of the shadow's rim.

---

[13] The shadow region is assumed to be simply connected.

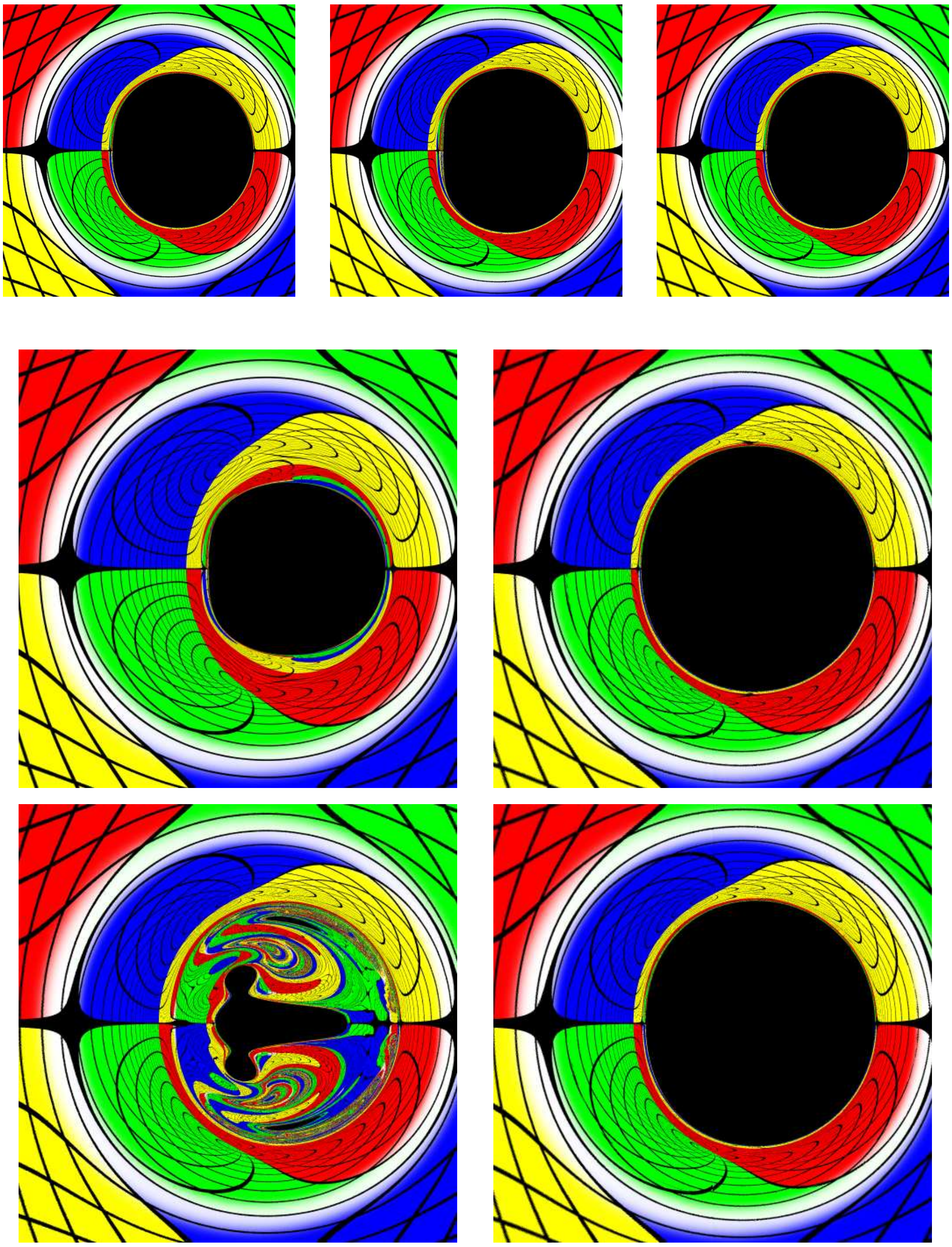

Figure 2.4.6: Examples of shadows and gravitational lensing of HBHs. From left to right: *(first row)* configuration I and respective Kerr$_{ADM}$ and Kerr$_{H}$; *(second row)* configuration II and the respective Kerr$_{ADM}$; *(third row)* configuration III and respective Kerr$_{ADM}$. The ray-tracing algorithm for the Kerr shadows uses all the symmetries of that space-time.

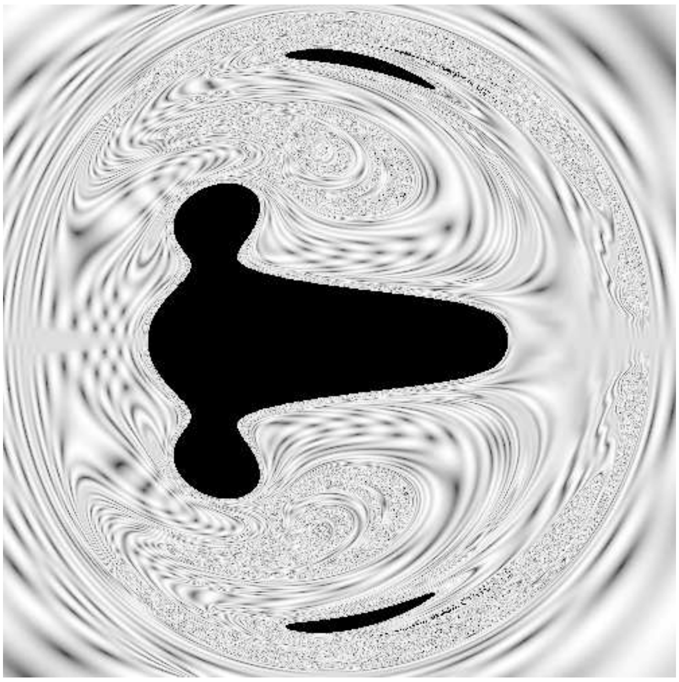

Figure 2.4.7: Representation of shadow III, now with the background pattern of Fig. 1.5.7. Two large eyebrows are clearly visible at symmetric positions, together with much smaller regions. This image is zoomed (the field of view is ± ≃ 0.33).

A generic point P at the shadow's edge is at a distance r from C:

$$r \equiv \sqrt{{y'_P}^2 + (x'_P - x'_C)^2}.$$

Introducing the angle α between the line $\overline{CP}$ and the x' axis, such that

$$\tan\alpha = \frac{y'_P}{x'_P - x'_C},$$

we can define the **average radius** $\bar{r}$ of the shadow as:

$$\bar{r} \equiv \frac{\int_0^{2\pi} r(\alpha)\, d\alpha}{\int_0^{2\pi} d\alpha} = \frac{1}{2\pi}\int_0^{2\pi} r(\alpha)\, d\alpha.$$

A parameter σ_r that measures the **deviation from sphericity** can also be defined, based on the standard deviation:

$$\sigma_r = \sqrt{\frac{1}{2\pi}\int_0^{2\pi} \Big(r(\alpha) - \bar{r}\Big)^2 d\alpha}.$$

For instance, due to spherical symmetry the shadow of a Schwarzschild BH is a circle (with radius r_o for example), and so we have $\bar{r} = r_o$ and $\sigma_r = 0$.

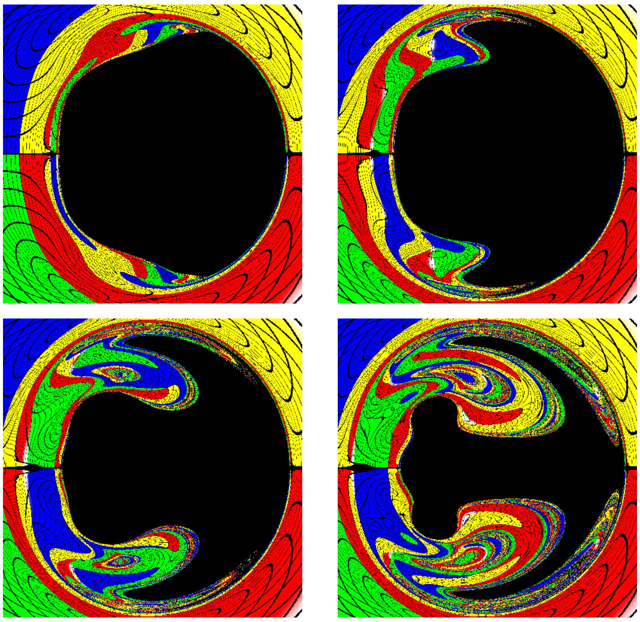

Figure 2.4.8: Examples of shadows which illustrate the transition between shadow II and III.

Another example, albeit purely academic, is a square shadow of side $2\,\ell$; this leads to $\bar{r} = \frac{4\ell}{\pi} \ln \left[\frac{1+\tan\pi/8}{1-\tan\pi/8}\right] \simeq 1.12\,\ell$ and $\sigma_r = \sqrt{\frac{4\ell^2}{\pi} - \bar{r}^2} \simeq 0.12\,\ell$

A final parameter that could be defined is the **relative deviation to a Kerr BH** with the same ADM mass and angular momentum as the BH under consideration (as long as the Kerr bound is not violated for the ADM quantities). By making the central points C coincide for both BHs we can compute a parameter $\sigma_{\rm Kerr}$:

$$\sigma_{\rm Kerr} = \sqrt{\frac{1}{2\pi}\int_0^{2\pi} \left(\frac{r(\alpha) - r_{\rm Kerr}(\alpha)}{r_{\rm Kerr}(\alpha)}\right)^2 d\alpha}.$$

If $r = r_{\rm Kerr}$ for all $\alpha \in [0, 2\pi]$ then $\sigma_{\rm Kerr} = 0$. Also, if $r = 2\,r_{\rm Kerr}$ for all $\alpha \in [0, 2\pi]$ then $\sigma_{\rm Kerr} = 1$ (a 100% deviation from Kerr). Therefore, given a shadow, we have at least six parameters $\{D_C, D_{x'}, D_{y'}, \bar{r}, \sigma_r, \sigma_{\rm Kerr}\}$ that could be used to describe it.

In the next table are displayed some of the discussed parameters for shadows I – III (in units of ADM mass M), together with the corresponding Kerr configurations with the same ADM quantities. The Kerr BH with $a_o = 0.971$ in the table is an exception, since it has the same horizon parameters, not ADM, as the HBH in configuration I (see Fig. 2.4.6, first row in the right);

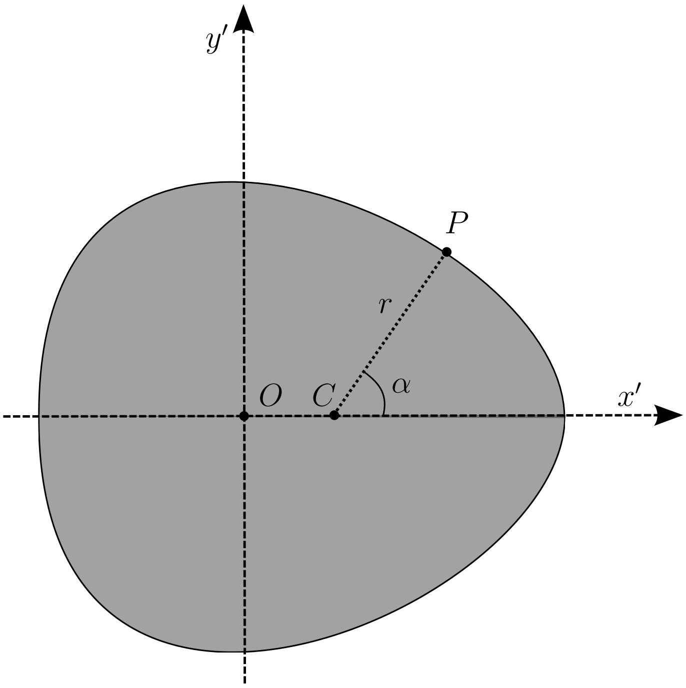

Figure 2.4.9: Representation of a BH shadow in the (x', y') plane of the observer.

this specific case is labeled with (*).

	D_C	$D_{x'}$	$D_{y'}$	$\bar{r}$	σ_r	$\sigma_r/\bar{r}$ (%)	σ_{Kerr} (%)
Configuration I	2.07	8.48	9.33	4.48	0.17	3.8	4.8
Configuration II	2.39	7.14	6.91	3.60	0.12	3.3	25.5
Configuration III	1.79	5.30	4.67	1.63	0.84	51.3	68.1
Kerr $a_o = 0.99869$ (I)	2.39	8.70	9.86	4.70	0.26	5.5	0.27
Kerr $a_o = 0.971$ (I*)	2.10	8.48	9.33	4.50	0.19	4.1	0.41
Kerr $a_o = 0.849$ (II)	1.82	9.33	9.83	4.82	0.11	2.3	0.37
Kerr $a_o = 0.894$ (III)	1.94	9.23	9.83	4.80	0.13	2.7	0.35
Kerr $a_o = 0.99869$ ($\text{I}^\dagger$)	2.38	8.66	9.86	4.70	0.26	5.5	0
Kerr $a_o = 0.971$ ($\text{I}^\dagger$*)	2.08	8.48	9.36	4.50	0.18	4.0	0
Kerr $a_o = 0.849$ ($\text{II}^\dagger$)	1.79	9.32	9.86	4.82	0.10	2.2	0
Kerr $a_o = 0.894$ ($\text{III}^\dagger$)	1.92	9.22	9.86	4.80	0.13	2.6	0

The displayed Kerr parameters are either obtained from the respective analytic solution for the shadow (marked with the symbol †) or from numerical ray-tracing. For the latter conservation symmetries of the Kerr space-time

were used, namely the Carter constant. The details of the analytic solution can be found in Appendix A.6.
The integrals defined previously, namely for $\bar{r}$, σ_r and σ_{Kerr}, were all computed using a modified Simpson's rule. Also, each parameter σ_{Kerr} was calculated with respect to the corresponding analytic Kerr shadow with the same ADM parameters. Furthermore, there is an observable difference if the analytic solution for the Kerr shadow is computed for an observer at infinity, rather than at $\tilde{r} = 15M$ (ADM).

For shadow I, besides $\sigma_{\text{Kerr}} = 4.8\%$, we can also compute $\sigma^*_{\text{Kerr}} = 0.52\%$, e.g. its deviation from the analytic Kerr shadow with the same horizon quantities (not ADM), marked in the table with ($^{\dagger *}$). Thus the shape and size of shadow I is almost identical to the shadow of the associated Kerr$_H$. Additionally, notice that $\bar{r}$ of shadow II is almost $\sim 75\%$ smaller than the mean radius associated with the Kerr$_{ADM}$. Shadow II is also much more square-like, with a larger normalized deviation from sphericity ($\sigma_r/\bar{r}$). However, the strongest deviation from Kerr is clearly for shadow III: almost 70%!

This shadow parametrization allows us to estimate the numerical error for the shadows. For instance, it is clear that there is a deviation $\sim 0.3\%$ between Kerr shadows computed analytically and ones obtained from the Kerr ray-tracing code with the full symmetries, such as the Kerr shadows in Fig. 2.4.6. Additionally, it is estimated that for HBH shadows the associated error is of order $\sim 1\%$. This can be obtained by analysing the shadow for a Kerr configuration obtained numerically, using the methods described in section 2.3 as an endpoint of the HBH family (not shown here). This shadow can then be compared with the analytic solution, which is known for Kerr. The total $\sim 1\%$ deviation then includes numerical error for the space-time geometry, the interpolation of that data, and the possible difference between the ADM parameters of the numerical space-time and of the comparable Kerr BH. The numerical error of the HBH ray-tracing algorithm itself also makes a contribution but it is estimated to be only of the order $\sim 0.3\%$. This can be done by using the analytic form of the Kerr geometry.

2.5 Conclusions

Kerr BHs with scalar hair (KBHsSH) are novel exact solutions of Einstein's General Relativity which display very interesting properties. Some of these features are shadows with a significant deviation from standard Kerr predictions. Indeed, as it is illustrated by shadows II and III, new types of shadows can arise. However, even for HBHs close to Kerr in the solution space, there is a significant difference between the corresponding shadows, given that they have the same ADM quantities; this is well illustrated by shadow I.
Another important result is that HBH shadows are *smaller* than for the corresponding Kerr$_{ADM}$. This is anticipated, since part of the total energy is contained in the "hair" besides the central BH. As such, when compared with a Kerr BH with the same total (ADM) mass, the HBH shadow is expected to be smaller. Although the astrophysical relevance of these solutions is not absolutely clear, they could provide an appealing alternative to Kerr predictions, namely since HBHs can make a continuous connection from Kerr shadows to some other exotic shapes. Thus, possible shadow templates could be provided for future VLBI and EHT observations using this family of solutions.

The gravitational lensing produced by BSs is also a fascinating subject, with a close connection to HBH shadows. Indeed, it proves helpful to understand the shapes of the latter and some of its features, such as possible fractal structures. To the knowledge of the author, lensing images of BS had not yet been provided in literature, together with the realization that they have no shadow [71].

The present work can be continued, opening a line of possible research directions. For instance, analysis of shadows can be made exhaustively for all the space of solutions, and even extended for observers outside the equatorial plane; preliminary work in this direction has already revealed potentially interesting results. Furthermore, the introduction of more realistic light sources such as an accretion disk, instead of a celestial sphere, is also a compelling possibility. For the latter, a red-shift analysis would also be conducted.

Moreover, the HBH ray-tracing algorithm can be improved, and the usage of other ray-tracing codes, such as GYOTO, would also allow a cross-check of the results. The fit approach, tested as a numerical approximation tool to the HBH geometry, could be further developed and used to ease the public access to HBH solutions. This pseudo-analytic form of the metric would also improve computational performance.
Additionally, this analysis could even be extended to BH solutions with more general hair, namely scalars with self-interactions or Proca hair [59, 60].

Appendices

Appendix A

A.1 Heuristic arguments for $a^2 \leq m^2$ (Kerr bound)

This appendix is aimed to give three reasonable and heuristic arguments for the condition $m^2 \geq a^2$, which establishes a maximum limit for the rotation of a Kerr BH. The following reasoning strongly follows a private talk by Prof. Carlos Herdeiro [9].

First we will start by analysing the geodesic motion of a photon near the event horizon. The equations for $\dot{\varphi}$ and $\dot{t}$ are given by (1.3.4) and (1.3.3) on page 20. They are here repeated for convenience:

$$\rho^2\dot{\varphi} = 2mr\frac{Ea}{\Delta} + \Phi\frac{\Delta - a^2\sin^2\theta}{\Delta\sin^2\theta}, \tag{A.1.1a}$$

$$\rho^2\dot{t} = \frac{E}{\Delta}\left[(r^2+a^2)^2 - a^2\Delta\sin^2\theta\right] - 2mr\frac{a\Phi}{\Delta}. \tag{A.1.1b}$$

Dividing both equations and using $2mr = (r^2 + a^2 - \Delta)$ we obtain:

$$\frac{\dot{\varphi}}{\dot{t}} = \frac{d\varphi}{dt} = \frac{(r^2+a^2-\Delta)Ea + \Phi(\Delta - a^2\sin^2\theta)/\sin^2\theta}{E\left[(r^2+a^2)^2 - a^2\Delta\sin^2\theta\right] - a\Phi(r^2+a^2-\Delta)}.$$

On the outer event horizon $r = r_+$ and $\Delta = 0$:

$$\frac{d\varphi}{dt}_{(r=r_+)} \equiv \Omega_H = \frac{(r_+^2+a^2)Ea - \Phi a^2}{E(r_+^2+a^2)^2 - a\Phi(r_+^2+a^2)},$$

$$= \left(\frac{a}{r_+^2+a^2}\right)\frac{(r_+^2+a^2)E - \Phi a}{E(r_+^2+a^2) - a\Phi}.$$

We conclude therefore that the photon's angular velocity[1] as observed from infinity [21] is given by:

$$\boxed{\Omega_H = \frac{a}{r_+^2 + a^2}.}$$

This result does not depend on the constants of motion E and Φ of the photon and neither on the latitude coordinate θ. This angular velocity is therefore an intrinsic property of the event horizon itself, which rotates uniformly as if it was a solid body [11]. For this reason, in literature Ω_H is defined to be the angular velocity of the event horizon of a Kerr BH [1,5].

The "perimeter" of the horizon equator ($\theta = \pi/2$ and $r = r_+$) is given by:

$$\mathcal{P} = \int_0^{2\pi} \sqrt{g_{\varphi\varphi}}\, d\varphi = 2\pi\sqrt{g_{\varphi\varphi}}\,;$$

since none of the metric terms depends on φ the integration is trivial. Defining the perimetral radius $\tilde{r}$ (see 1.5.24) such that:

$$\mathcal{P} = 2\pi\tilde{r},$$

we conclude that $\tilde{r} = \sqrt{g_{\varphi\varphi}}$. Defining the velocity[2] of the horizon $\tilde{v}$ as:

$$\tilde{v} = \Omega_H\, \tilde{r},$$

we obtain

$$\tilde{v} = \frac{a}{r_+^2 + a^2}\sqrt{r_+^2 + a^2 + \frac{(r_+^2 + a^2 - \cancel{\Delta})a^2}{r_+^2}} = \frac{a\sqrt{r_+^2 + a^2}}{r_+^2 + a^2}\sqrt{1 + \frac{a^2}{r_+^2}} =$$

$$= \frac{a}{\cancel{\sqrt{r_+^2 + a^2}}}\sqrt{\frac{\cancel{(r_+^2 + a^2)}}{r_+^2}} = \frac{a}{r_+} = \frac{a}{m + \sqrt{m^2 - a^2}}.$$

We conclude that $\tilde{v}$ it always less or equal than 1 for $m^2 \geq a^2$. Because the velocity $\tilde{v}$ is measured in units of c, it means that the "horizon speed" never surpasses the speed of light. Curiously enough, the speed of light is in fact only reached for the extremal case $|a| = m$. From this analysis, a possible heuristic viewpoint is that the restriction $m^2 \geq a^2$ in fact enforces the horizon velocity not to be greater than the speed of light.

---

[1] In fact, because t has units of distance, Ω_H only has dimensions of an angular velocity if units $c = 1$ are used. If not, it is $c\,\Omega_H$ that has the correct dimensions.

[2] The quantity $\tilde{v}$ only has dimensions of a velocity if units $c = 1$ are used.

Another heuristic argument relies on the order of magnitude of the gravitational and rotational energies of a BH as expected classically. For instance, the gravitational bending energy is of order:

$$E_g \sim \frac{GM^2}{r},$$

and the energy associated with rotation is of order:

$$E_r \sim \frac{J^2}{Mr^2},$$

where J is the BH angular momentum.
Because the centrifugal forces cannot overcome the gravitational attraction, we must have:

$$E_g \gtrsim E_r \implies \frac{GM^2}{r} \gtrsim \frac{J^2}{Mr^2},$$

Also, r has the same order of magnitude as the event horizon length scale:

$$r \sim \frac{GM}{c^2}.$$

This leads to:

$$\frac{G^2M^2}{c^4} \gtrsim \frac{J^2}{M^2c^2} \implies m^2 \gtrsim a^2.$$

It is interesting that although we followed a very simple (and almost naive) reasoning, we have in fact obtained an exact result!

A third heuristic argument starts from the requirement for the velocity of the event horizon to be less than the speed of light, in order of magnitude:

$$v = \omega r \lesssim c,$$

where ω is given by:

$$\omega \sim \frac{J}{Mr^2}.$$

This leads to:

$$\frac{Jr}{Mr^2} \lesssim c \implies \frac{J}{Mc} \lesssim \frac{GM}{c^2} \implies a \lesssim m,$$

where $r \sim GM/c^2$ was also used.

A.2 Kerr spherical orbits

From equations (1.4.8) and (1.4.2) we have the conditions for spherical orbits in the Kerr metric:

$$\mathcal{R} = r^4 + Ar^2 + Br + C = 0, \tag{A.2.1}$$

$$\frac{d\mathcal{R}}{dr} = 4r^3 + 2Ar + B = 0, \tag{A.2.2}$$

with

$$A = a^2 - \eta - \lambda^2, \qquad B = 2m\left(\eta + (a-\lambda)^2\right) \qquad \text{and} \qquad C = -\eta a^2.$$

Combining (A.2.1) and (A.2.2) we get

$$-3r^4 - Ar^2 + C = 0,$$

or

$$-3r^4 + \eta r^2 - (a^2 - \lambda^2)r^2 - \eta^2 a^2 = 0,$$

which can be solved for η:

$$\boxed{\eta = \frac{3r^4 + (a^2-\lambda^2)r^2}{r^2 - a^2}.} \tag{A.2.3}$$

Inserting this expression back into (A.2.2) yields

$$4r^3 + 2r\left(a^2 - \lambda^2 - \frac{3r^4 + r^2(a^2-\lambda^2)}{r^2-a^2}\right) + 2m\left((a-\lambda)^2 + \frac{3r^4 + r^2(a^2-\lambda^2)}{r^2-a^2}\right) = 0,$$

Multiplication by $(r^2 - a^2)/2$ gives after some algebraic manipulations

$$A_2\lambda^2 + B_2\lambda + C_2 = 0, \tag{A.2.4}$$

with

$$A_2 = a^2(r-m), \quad B_2 = -2ma(r^2-a^2), \quad \text{and} \quad C_2 = -(r^2+a^2)(r^3+ra^2-3mr^2+ma^2).$$

The solution to the quadratic equation (A.2.4) is

$$\lambda = \frac{-B_2 \pm \sqrt{D}}{2A_2}, \tag{A.2.5}$$

were the discriminant $D = B_2^2 - A_2C_2$ is given by

$$D = 4(r^2 - a^2)^2 m^2 a^2 + 4a^2(r-m)(r^2+a^2)(r^3 + ra^2 - 3mr^2 + ma^2),$$

which can be simplified into

$$D = 16a^2r^4m^2 - 16a^2r^3(r^2+a^2)m + 4a^2r^2(r^2+a^2)^2.$$

Making use of the expression $2mr = r^2 + a^2 - \Delta$, we obtain

$$D = 4a^2r^2(r^2+a^2-\Delta)^2 - 8a^2r^2(r^2+a^2)(r^2+a^2-\Delta) + 4a^2r^2(r^2+a^2)^2,$$

which leads to [20]

$$\boxed{D = 4a^2r^2\Delta^2.}$$

The root (A.2.5) has therefore the form

$$\lambda = \frac{2ma(r^2-a^2) \pm \sqrt{4a^2r^2\Delta^2}}{2a^2(r-m)},$$

or

$$\lambda = \frac{m(r^2-a^2) \pm r\Delta}{a(r-m)}. \tag{A.2.6}$$

For the **positive sign** in (A.2.6):

$$\lambda_+ = \frac{m(r^2-a^2) + r^3 + a^2r - 2mr^2}{a(r-m)} = \frac{(r^2+a^2)\cancel{(r-m)}}{a\cancel{(r-m)}},$$

or

$$\boxed{\lambda_+ = \frac{r^2+a^2}{a}.} \tag{A.2.7}$$

Using (A.2.3) we obtain for η_+

$$\eta_+ = \frac{1}{r^2-a^2}\left(3r^4 + a^2r^2 - r^2\frac{(r^2+a^2)^2}{a^2}\right) = -\frac{r^4\cancel{(r^2-a^2)}}{a^2\cancel{(r^2-a^2)}},$$

and thus we obtain

$$\boxed{\eta_+ = -\frac{r^4}{a^2}.} \tag{A.2.8}$$

The class of solutions λ_+ and η_+ are called class i). In subsection 1.4.1 it is proven that this class does not correspond to spherical orbits and thus it is not physical [22, 23].

For the **negative sign** in (A.2.6):

$$\lambda_- = \frac{m(r^2-a^2) - r^3 - a^2r + 2mr^2}{a(r-m)},$$

which leads to

$$\boxed{\lambda_- = -\frac{r^3 + a^2r + ma^2 - 3mr^2}{a(r-m)}.} \tag{A.2.9}$$

The value of η_- can be computed using (A.2.3):

$$\begin{aligned}\eta_- &= \frac{r^2}{(r^2-a^2)}(3r^2 + a^2 - (\lambda_-)^2) \\ &= \frac{r^2}{(r^2-a^2)(r-m)^2a^2}\{(3r^2+a^2)(r-m)^2a^2 - (r^3 + a^2r + ma^2 - 3mr^2)^2\}.\end{aligned}$$

After some algebraic simplifications and factorization this yields:

$$\eta_- = \frac{r^2\cancel{(r^2-a^2)}}{\cancel{(r^2-a^2)}(r-m)^2a^2}(-r^4 - 9m^2r^2 + 6mr^3 + 4rma^2),$$

or

$$\boxed{\eta_- = -\frac{r^3(r^3 + 9m^2r - 6mr^2 - 4ma^2)}{a^2(r-m)^2}.} \tag{A.2.10}$$

The class of solutions λ_- and η_- are called class ii). They correspond to the physical photon orbits [22, 23].

A.3 Theorem 1

Theorem:

For spherical photon orbits in the Kerr metric we must always have [23]:

$$f(r) \equiv a^2 - \eta - \lambda^2 < 0,$$

for $r > r_+$ and $0 \le a^2 \le m^2$. Here $r_+ = m + \sqrt{m^2 - a^2}$ is the outer event horizon radial coordinate and r is the orbit radius.

Proof:

Starting from (A.2.3) in Appendix A.2,

$$\eta = \frac{3r^4 + a^2r^2 - \lambda^2 r^2}{r^2 - a^2}, \qquad \text{we get} \qquad \lambda^2 = 3r^2 + a^2 + \left(\frac{a^2}{r^2} - 1\right)\eta,$$

and so,

$$f(r) = a^2 - \eta - 3r^2 - a^2 + \left(1 - \frac{a^2}{r^2}\right)\eta = -\left(3r^2 + \frac{a^2}{r^2}\eta\right), \quad \forall\, |a_o| \in [0,1].$$

Because η is finite, if $a = 0$ we have $f(r) = -3r^2 < 0, \quad \forall\, r > r_+ > 0$. So the theorem is proven for all classes if $a = 0$.

For class i) [3], and for $r > r_+ > 0,\ |a_o| \in]0,1]$ we have (see (A.2.8))

$$\eta = -\frac{r^4}{a^2}, \qquad \text{and so} \qquad f(r) = -\left(3r^2 - \frac{a^2}{r^2}\frac{r^4}{a^2}\right) = -2r^2 < 0.$$

We conclude therefore that for class i) we must have $f(r) < 0$ for $r > r_+$, as pretended, $\forall\, |a_o| \in [0,1]$.

For class ii) the function f takes the form (see (A.2.10)):

$$\begin{aligned} f(r) &= -\frac{3r^4(r-m)^2 + a^2(r-m)^2\eta}{r^2(r-m)^2} \\ &= -\frac{3r^4(r-m)^2 - r^3(r^3 - 6mr^2 + 9m^2r - 4a^2m)}{r^2(r-m)^2}, \end{aligned}$$

which simplifies to

$$f(r) = -\frac{2r(r^3 - 3rm^2 + 2a^2m)}{(r-m)^2}. \tag{A.3.1}$$

The derivative of this function is easily computed as

$$\frac{df}{dr}(r) = -\frac{4(r+m)}{(r-m)^3}(r^3 - 3mr^2 + 3m^2r - ma^2), \tag{A.3.2}$$

For the moment being we will take $0 < a^2 < m^2$ and $r \geq r_+ > m$. The case

---

[3] See Appendix A.2 for discussion.

$a^2 = m^2$ will be analyzed later.
We now prove that (A.3.2) is always negative for $r > m$. Proving this statement is equivalent to show that

$$F(r) \equiv r^3 - 3mr^2 + 3m^2 r - ma^2 > 0, \qquad \text{for} \qquad r > m.$$

Notice that

$$\frac{dF}{dr}(r) = 3r^2 - 6mr + 3m^2,$$

which is a parabola in the r coordinate with only one zero:

$$r = \frac{6m \pm \sqrt{\cancel{36m^2} - \cancel{4 \times 3^2 m^2}}}{6} = m.$$

Because the parabola has a positive curvature we have

$$\frac{dF}{dr}(r) > 0, \qquad \text{for} \qquad r > m.$$

Also

$$F_{(r=m)} = m(m^2 - a^2) > 0,$$

so we conclude therefore that

$$F(r) > 0, \qquad \text{for} \qquad r > m,$$

which proves

$$\frac{df}{dr}(r) < 0, \qquad \text{for} \qquad r > m.$$

For $r \geq r_+ > m$, we then have

$$f(r) \leq f(r_+), \tag{A.3.3}$$

where

$$f(r_+) = -\frac{2r_+}{(r_+ - m)^2} \underbrace{(r_+^3 - 3r_+ m^2 + 2a^2 m)}_{\xi}. \tag{A.3.4}$$

The factor ξ can be simplified into

$$\xi = (m^2 - a^2)(m + \sqrt{m^2 - a^2}) > 0,$$

which implies by (A.3.4) that

$$f(r_+) < 0.$$

From (A.3.3) we conclude therefore that

$$\boxed{f(r) = a^2 - \eta - \lambda^2 < 0},$$

for $r \geq r_+$ and $0 \leq a^2 < m$.

The case $a^2 = m^2$ should be handle with special care due to the pole at $r = r_+ = m$. We have then from (A.3.1) and (A.3.2):

$$f(r) = -\frac{2(r^4 - 3r^2m^2 + 2m^3r)}{(r-m)^2},$$

$$\frac{df}{dr}(r) = -\frac{4(r^4 + 2m^3r - m^4 - 2mr^3)}{(r-m)^3}.$$

The limit $r \to m^+$ is of type $0/0$ for both f and df/dr. Using L'Hospital rule [26]:

$$\lim_{r\to m^+} f(r) = \lim_{r\to m^+} -\frac{4r^3 - 6m^2r + 2m^3}{r-m} = \lim_{r\to m^+} -(12r^2 - 6m^2) = -6m^2 < 0,$$

as for

$$\lim_{r\to m^+} \frac{df}{dr}(r) = \lim_{r\to m^+} -\frac{4(4r^3 + 2m^3 - 6mr^2)}{3(r-m)^2} = \lim_{r\to m^+} -\frac{4(12r^2 - 12mr)}{6(r-m)}$$

$$= \lim_{r\to m^+} -\frac{4}{6}(24r - 12m) = -8m < 0.$$

These limits are well defined from positive values and the derivative df/dr is well behaved all the way until $r = m$. The previous argument for $a^2 \neq m^2$ can then still be used to conclude that

$$\frac{df}{dr}(r) < 0, \qquad \text{for} \qquad r > m.$$

If we now take $r > (r_+ = m)$ and make the substitution in the previous reasoning ($a^2 \neq m^2$)

$$f(r_+) \to \lim_{r\to m^+} f(r),$$

we would still obtain

$$f(r) < 0, \qquad \text{for} \qquad r > m.$$

We have therefore proven the theorem for $r > r_+$ and $0 \leq a^2 \leq m^2$.

A.4 Cubic roots

The solution to a cubic equation is not very well known in the science community, except for mathematicians. In this appendix the roots of a generic cubic equation are computed. We follow a trigonometric approach, discovered by François Viéte (1540-1603) more than 400 years ago [74].

Starting from a generic cubic equation[4]

$$x^3 + bx^2 + cx + d = 0, \tag{A.4.1}$$

we can change the variable[5] x by

$$x = t - \frac{b}{3},$$

which yields the depressed cubic form

$$\boxed{t^3 + pt + q = 0,} \tag{A.4.2}$$

where

$$p = \frac{3c - b^2}{3} \qquad \text{and} \qquad q = \frac{2b^3 - 9bc + 27d}{27}.$$

By a new change of variable

$$t = 2\sqrt{-\frac{p}{3}}\cos\theta, \qquad \text{with} \qquad p < 0,$$

we then obtain

$$2^3\sqrt{-\frac{p}{3}}\left(-\frac{p}{3}\right)\cos^3\theta + 2p\sqrt{-\frac{p}{3}}\cos\theta = -q,$$

which leads to the form

$$4\cos^3\theta - 3\cos\theta = \frac{3}{2}\frac{q}{p}\sqrt{-\frac{3}{p}}. \tag{A.4.3}$$

From trigonometry it can be shown that [26]

$$4\cos^3\theta - 3\cos\theta = \cos(3\theta),$$

and so from (A.4.3) we conclude that

$$\cos(3\theta) = \frac{3}{2}\frac{q}{p}\sqrt{-\frac{3}{p}},$$

---

[4] This cubic equation is indeed general: if the factor multiplied by x^3 is non unity, all the equation can by divided by that factor, which gives the form (A.4.1).

[5] Notice on notation: x, t, θ are not related to the variables depicted in the main text.

and that

$$\theta = \frac{1}{3}\arccos\left(\frac{3}{2}\frac{q}{p}\sqrt{-\frac{3}{p}}\right) - \frac{2\pi}{3}k,$$

with $k \in \{0, 1, 2\}$.

The solution of the cubic equation has then the form

$$\boxed{x = -\frac{b}{3} + 2\sqrt{-\frac{p}{3}}\cos\left(\frac{1}{3}\arccos\left[\frac{3}{2}\frac{q}{p}\sqrt{-\frac{3}{p}}\right] - \frac{2\pi}{3}k\right)}, \tag{A.4.4}$$

where the integer $k \in \{0, 1, 2\}$ yields the three possible solutions.

A.4.1 Applications: finding roots of η and λ

In section 1.4.2 it is necessary to compute the roots of the equation (see (1.4.10))

$$\eta(r) = 0.$$

This implies, for $r \neq 0$, that

$$r^3 - 6mr^2 + 9m^2 r - 4a^2 m = 0.$$

This cubic equation can be brought into dimensionless form by defining

$$x \equiv \frac{r}{m} \qquad \text{and} \qquad a_o = \frac{a}{m},$$

where $0 \leq a_o^2 \leq 1$. We have then

$$x^3 - 6x^2 + 9x - 4a_o^2 = 0.$$

Comparison to (A.4.1) yields $b = -6$, $c = 9$ and $d = -4a_o^2$.
For the depressed cubic form we have:

$$p = -3, \qquad \text{and} \qquad q = 2 - 4a_o^2.$$

We then get:

$$x = 2 + 2\cos\left(\frac{1}{3}\arccos\left(2a_o^2 - 1\right) - \frac{2\pi}{3}k\right), \tag{A.4.5}$$

with $k \in \{0, 1, 2\}$.

To simplify expression (A.4.5) we now prove that

$$\arccos(2a_o^2 - 1) = 2\arccos(|a_o|).$$

We start from the complex form of $\arccos\beta$ [26]:

$$\arccos\beta = i\ln\left(\beta - i\sqrt{1-\beta^2}\right), \qquad \text{with} \qquad 0 \leq \beta^2 \leq 1.$$

It is possible to set $\beta = 2a_o^2 - 1$ because $0 \leq a_o^2 \leq 1 \implies 0 \leq \beta^2 \leq 1$. We have therefore

$$\begin{aligned} \arccos(2a_o^2 - 1) &= i\ln\left(2a_o^2 - 1 - i\sqrt{\cancel{1} - 4a_o^4 - \cancel{1} + 4a_o^2}\right) \\ &= i\ln\left(2a_o^2 - 1 - 2|a_o|i\sqrt{1-a_o^2}\right). \end{aligned}$$

Because of the equality

$$\left(|a_o| - i\sqrt{1-a_o^2}\right)^2 = 2a_o^2 - 1 - 2|a_o|i\sqrt{1-a_o^2},$$

we then obtain

$$\begin{aligned} \arccos(2a_o^2 - 1) &= i\ln\left(\left[|a_o| - i\sqrt{1-a_o^2}\right]^2\right) \\ &= 2i\ln\left(|a_o| - i\sqrt{1-a_o^2}\right) \\ &= 2\arccos(|a_o|), \end{aligned}$$

as pretended.

The solutions to the equation $\eta(r) = 0$ are therefore given by

$$r = 2m\left\{1 + \cos\left(\frac{2}{3}\arccos\left(\frac{|a|}{m}\right) - \frac{2\pi}{3}k\right)\right\},$$

with $k \in \{0, 1, 2\}$.

For $\boxed{k = 0}$:

$$\boxed{r = r_2 \equiv 2m\left\{1 + \cos\left(\frac{2}{3}\arccos\left(\frac{|a|}{m}\right)\right)\right\},}$$

and it corresponds to a orbit with retrograde motion (see section 1.4.3).

For $\boxed{k = 1}$ the value of θ is:

$$\theta = \frac{2}{3}\arccos|a_o| - \frac{2\pi}{3}.$$

Using the trigonometric relation

$$\arccos(y) = \pi - \arccos(-y),$$

we get

$$\theta = \frac{2\cancel{\pi}}{\cancel{3}} - \frac{2}{3}\arccos\left(-|a_o|\right) - \frac{2\cancel{\pi}}{\cancel{3}} = -\frac{2}{3}\arccos\left(-|a_o|\right),$$

The associated root is then

$$\boxed{r = r_1 \equiv 2m\left\{1 + \cos\left(\frac{2}{3}\arccos\left(-\frac{|a|}{m}\right)\right)\right\},}$$

and it corresponds to a orbit with prograde motion (see section 1.4.3).

For $\boxed{k = 2}$ the value of θ is:

$$\theta = \frac{2}{3}\arccos|a_o| - \frac{4\pi}{3}.$$

The trigonometric inequalities now used are:

$$x_1 > x_2 \implies \arccos x_1 < \arccos x_2,$$

and

$$\theta_1 > \theta_2 \implies \cos\theta_1 < \cos\theta_2,$$

for θ_1, θ_2 both in the first and second trigonometric quadrants.
We then have

$$0 \le |a_o| \le 1 \implies \frac{\pi}{2} \ge \arccos|a_o| \ge 0 \implies \pi \ge 2\arccos|a_o| \ge 0,$$

and so

$$-3\pi \ge (2\arccos|a_o| - 4\pi) \ge -4\pi \implies -\pi \ge \left(\frac{2}{3}\arccos|a_o| - \frac{4\pi}{3}\right) \ge -\frac{4\pi}{3}.$$

Because both $-\pi$ and $-\frac{4\pi}{3}$ are in the second quadrant we have

$$\cos(-\pi) \le \cos\theta \le \cos\left(-\frac{4\pi}{3}\right) \implies -1 \le \cos\theta \le -\frac{1}{2} \implies 0 \le r \le m.$$

This is not a physical solution as $r < m$ is always inside the event horizon.

In section 1.4.3 is necessary to compute the roots of the equation $\lambda(r) = 0$. From (1.4.10) we obtain the condition

$$r^3 - 3mr^2 + a^2 r + a^2 m = 0;$$

in dimensionless form:

$$x^3 - 3x^2 + a_o^2 x + a_o^2 = 0.$$

Comparison to (A.4.1) yields $b = -3$, $c = a_o^2$ and $d = a_o^2$.
For the depressed cubic form we have then

$$p = a_o^2 - 3, \qquad \text{and} \qquad q = 2(a_o^2 - 1).$$

The solution with $k = 0$ in (A.4.4) is then

$$r = r_3 \equiv m \left\{ 1 + 2\sqrt{1 - \frac{a_o^2}{3}} \cos\left(\frac{1}{3} \arccos\left[\frac{1 - a_o^2}{\left(1 - \frac{a_o^2}{3}\right)^{3/2}} \right] \right) \right\},$$

with $a_o = a/m$. The other two solutions are nonphysical, as one is always inside the event horizon ($0 \leq r \leq m$) and the other has negative r, although this is not proven here (similar to above).

A.5 Theorem 2: "No Bound Theorem"

No Bound Theorem:

In a Kerr space-time, photon geodesics are never bounded, which means the radial coordinate r is never restricted to a limited interval: the photon either escapes to infinity or it is captured by the BH.

The spherical photon orbits mentioned in section 1.4.2 are necessarily unstable. These orbits are not considered here as bounded since any small perturbation causes the photon to escape or being captured.

Proof [6]:

Starting from (1.4.2):

$$R = E^2 r^4 + (a^2E^2 - \Phi^2 - Q)r^2 + 2mr\left[(aE - \Phi)^2 + Q\right] - a^2 Q,$$

it can be rearranged into

$$R = (r^4 + a^2r^2 + 2mra^2)E^2 - 4mra\Phi E - \left[(Q + \Phi^2)\Delta - a^2\Phi^2\right].$$

---

[6] This proof is strongly follows the work by Wilkins [17].

So R is a parabola as a function of E.
A radial potential $V(r)$ is by definition one such that [17]

$$E = V(r) \implies R(r) = 0.$$

Solving for E yields two solutions:

$$V_{\pm} = \frac{4mra\Phi \pm \sqrt{16m^2r^2a^2\Phi^2 + 4[r^4 + a^2r^2 + 2mra^2][(Q + \Phi^2)\Delta - a^2\Phi^2]}}{2(r^4 + a^2r^2 + 2mra^2)},$$

and so R can be factorized as

$$R = (r^4 + a^2r^2 + 2mra^2)(E - V_+)(E - V_-).$$

From (1.3.1) we have that $R \geq 0$. From the parabolic behaviour in E (see Fig. A.5.1) this implies that

$$E \geq V_+ \qquad \text{or} \qquad E \leq V_-.$$

By making the simultaneous transformations

$$E \to -E \qquad \text{and} \qquad \Phi \to -\Phi, \tag{A.5.1}$$

we can transform the inequality $E \leq V_-$ into $E \geq V_+$ and vice-versa. Since transformations (A.5.1) leave the value of R invariant the analysis can be made with either V_+ or V_-, with no loss of generality.

We can gain insight into the conditions for bending by computing the limits of V_+ and V_- at infinity:

$$\lim_{r\to\infty} V_+ = \lim_{r\to\infty} \sqrt{Q}\,\frac{r^3}{r^4} = 0^+,$$

$$\lim_{r\to\infty} V_- = \lim_{r\to\infty} -\sqrt{Q}\,\frac{r^3}{r^4} = 0^-.$$

The physical interpretation of this result is that at infinity the radial potential is equal to the rest energy of the particle, which is zero for the case of a photon.
In order to have a region for bending, we thus must have at least three zeros of R (three turning points) for a given value of $E > 0$ (see Fig. A.5.2), since $V_+ \to 0^+$ at infinity. In fact it will proven that such a case is not possible for photons, as the typical form of V_+ has only two such zeros or less (see Fig. A.5.3).

We will now assume $E > 0$ for the moment and $0 \leq a^2 \leq m^2$. Using a variable transformation

$$r = x + m,$$

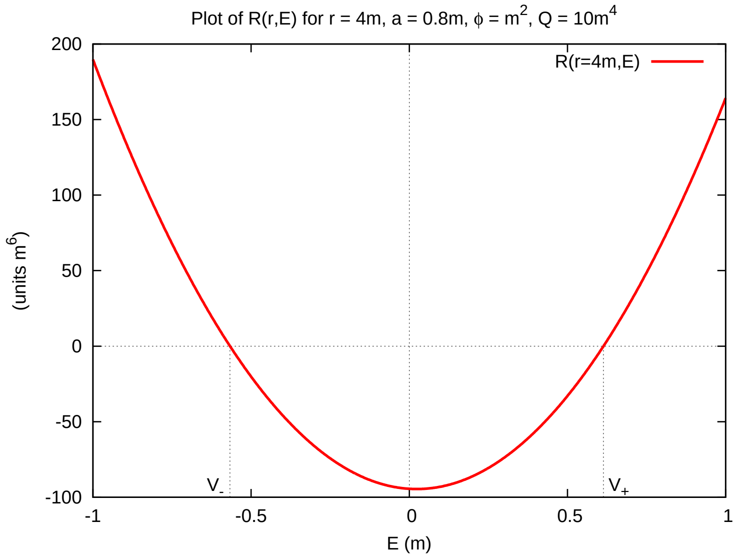

Figure A.5.1: Plot of R as function of the energy at infinity E and for radial coordinate $r = 4m$. The roots are $E = V_+$ and $E = V_-$. Because we must have $R \geq 0$ this implies $E \geq V_+$ or $E \leq V_-$.

we obtain for R:

$$R(x) = E^2(x+m)^4+(a^2E^2-\Phi^2-Q)(x+m)^2+2m(x+m)\left[(aE-\Phi)^2+Q\right]-a^2Q,$$

which can be expanded into

$$R(x) = E^2x^4 + (4mE^2)x^3 + c_2\,x^2 + c_1\,x + c_o,$$

with

$$c_2 = E^2(6m^2+a^2) - \Phi^2 - Q,$$
$$c_1 = 4E^2(m^3+ma^2) - 4maE\Phi,$$
$$c_o = (m^2-a^2)(Q+E^2m^2) + m^2(2aE-\Phi)^2.$$

The so called Descartes's rule of signs, after his work in "Le Géométrie", states that the number of positive roots of a polynomial is always less than or equal to the number of changes in sign between consecutive (non-zero) coefficients, ordered by power of the monomials. For the case of an inequality, the number of positive roots must be less by a even number [75].

Using this rule, R can have in principle three roots at maximum, if the following conditions are met:

$$c_2 < 0, \qquad c_1 > 0 \qquad \text{and} \qquad c_o < 0. \tag{A.5.2}$$

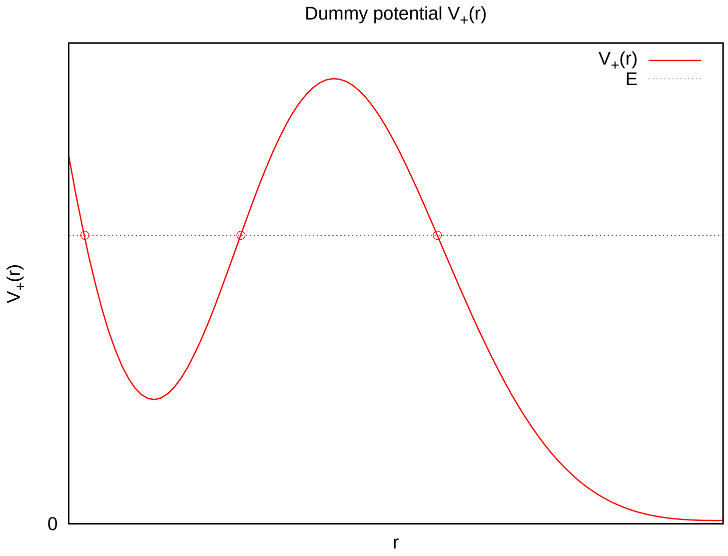

Figure A.5.2: Dummy potential $V_+(r)$ as function of the radial coordinate r, with three turning points for the given value of energy E (doted line). Because we must have $E \geq V_+$ and the potential approaches zero by positive values at infinity, it is clear that binding requires three turning points. In this picture there is a binding region between the first two turning points, counting from the origin. This type of potential does not actually exist for photons and in fact there are at most two turning points.

Taking into account dimensional analysis, then we can write

$$mc_1 > c_o + m^2\,c_2;$$

this yields after some algebra simplifications

$$a^2 Q > 3m^4 E^2.$$

For $E > 0$, as assumed, we must have $3m^4E^2 > 0$ and therefore

$$\text{if} \quad a = 0 \implies 0 > 0, \tag{A.5.3}$$

$$\text{if} \quad a \neq 0 \implies Q > 0 \implies c_o > 0. \tag{A.5.4}$$

Condition (A.5.3) is not possible and condition (A.5.4) contradicts the initial assumption (A.5.2). Therefore, for $E > 0$, is only possible to have at most two positive roots of $R(x)$.
As was already discussed, the system is invariant by transformation (A.5.1). The previous result for $E > 0$ does not depend on Φ so the conclusion can also be extended for $E < 0$.
The case $E = 0$ yields

$$R(x) = -(\Phi^2 + Q)x^2 + \left[Q(m^2 - a^2) + m^2\Phi^2\right],$$

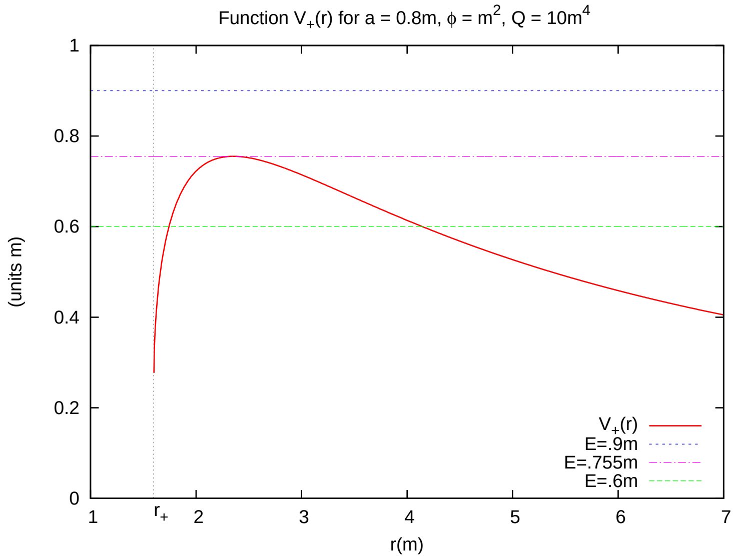

Figure A.5.3: Potential V_+ for photons with $a = 0.8m$, $\Phi = m^2$ and $Q = 10m^4$, as function of the radial coordinate r. The vertical doted black line displays the BH's event horizon, the limit of the potential's domain. Three different values of E are given by the horizontal doted lines. Each represent one of the possible three cases: of one, two or no turning points. From this picture it is clear that a bending region is not possible. For the case of one turning point ($E \simeq 0.755m$ given the mentioned parameters) an unstable photon orbit is possible at the intersection between V_+ and the doted pink line.

which has only one positive root.

We conclude that it is possible to have at most two roots of $R(x)$ for $x > 0$, or equivalently $r > m$. Attending to the fact that $r_+ \geq m$, the region outside[7] the event horizon is always covered by the previous condition $r > m$. Therefore binding is not possible for photons[8]. From this theorem it is clear that photon orbits are necessarily unstable, since a stable one would imply the existence of bounded states.

As a curiosity:

---

[7] The possible existence of a turning point at exactly $r = m$, which can only happen for $|a| = m$, should be of no concern. It is possible in fact to have $R = 0$ and $dR/dr = 0$ at that point if $\Phi = 2mE$ (for $a = m$). However it can be proven that for that case there can be at most one turning point for $r > m$ (similar above).

[8] However for time-like particles with rest mass $\mu > |E|$, bounded orbits are possible [17]. Photons are a special case for which the rest mass $\mu = 0$ and so the previous condition can never be met.

$R(E, r)$ defines a 2-surface (see Fig. A.5.4), with Φ, Q constant. By definition of $V_+(r)$:

$$R\Big(V_+(r), r\Big) = 0,$$

so the derivative with respect to r is also zero:

$$\frac{dR}{dr}(V_+, r) = 0 \implies \frac{\partial R}{\partial E}\frac{dV_+}{dr} + \frac{\partial R}{\partial r} = 0;$$

$$\text{if} \quad \frac{dV_+}{dr} = 0 \implies \frac{\partial R}{\partial r} = 0.$$

So if $V_+(r) = E$ and $\frac{dV_+}{dr} = 0$, then we have $R = 0$ and $\frac{\partial R}{\partial r} = 0$, the conditions for a spherical photon orbit.

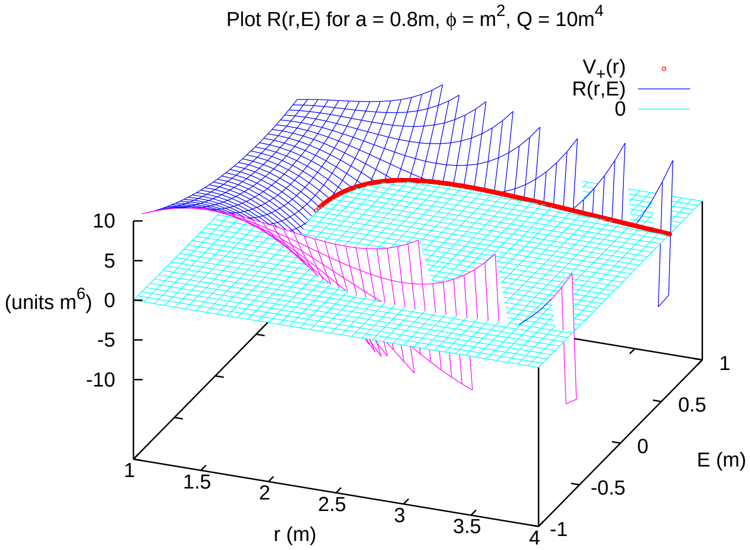

Figure A.5.4: Surface plot of R as function of the radial coordinate r and energy at infinity E for the photon. The parameters used were $a = 0.8m$, $\Phi = m^2$ and $Q = 10m^4$. Curves of constant E are polynomials of 4th order and curves of constant r are parabolas (see Fig. A.5.1). The intersection of the R surface with the xy plane of the graph yields both V_+ and V_-. The potential V_+ is given by the red line in the figure and is the same as in Fig. A.5.3.

A.6 Calculation of a shadow edge for a Kerr BH

In this section the shadow's edge of a Kerr BH will be calculated analytically for a more general ZAMO observer, rather than one at infinity as was done in page 48.

In the following calculations the observer is at a given perimetral radius $\tilde{r}$ and latitude coordinate θ_o. Also, the radial coordinate r_o can be computed from $\tilde{r}$ by using (1.5.32). Equations (1.5.26) are now repeated for convenience:

$$\begin{aligned} p^{(\varphi)} &= \mathsf{p} \sin\beta \, \cos\alpha, \\ p^{(\theta)} &= \mathsf{p} \sin\alpha, \\ p^{(r)} &= \mathsf{p} \cos\beta \, \cos\alpha. \end{aligned}$$

Solving for the observation angles α, β we obtain

$$\tan\beta = \frac{p^{(\varphi)}}{p^{(r)}},$$

$$\sin\alpha = \frac{p^{(\theta)}}{p^{(t)}}.$$

Since the domain of α is $[-\pi/2 : \pi/2]$ and assuming[9] $p^{(r)} \geq 0 \implies \cos\beta \geq 0$:

$$\beta = \arctan\left[\frac{p^{(\varphi)}}{p^{(r)}}\right],$$

$$\alpha = \arcsin\left[\frac{p^{(\theta)}}{p^{(t)}}\right].$$

Combining equations (1.3.1), (1.3.2) and (1.5.20 - 1.5.23) we have

$$\begin{aligned} p^{(\theta)} &= \pm\frac{\sqrt{\Theta}}{\sqrt{g_{\theta\theta}}}, \\ p^{(\varphi)} &= \frac{\Phi}{\sqrt{g_{\varphi\varphi}}}, \\ p^{(r)} &= \frac{\sqrt{R}}{\Delta\sqrt{g_{rr}}}, \\ p^{(t)} &= E\zeta - \gamma\Phi. \end{aligned}$$

Using the definition of the impact parameters $\lambda = \Phi/E$ and $\eta = Q/E^2$ in (1.4.1) and of the Cartesian parameters x', y' in (1.5.25):

$$y' = \tilde{r} \arcsin\left[\frac{p^{(\theta)}/E}{p^{(t)}/E}\right] = \tilde{r} \arcsin\left[\frac{\pm 1}{(\zeta - \lambda\gamma)} \frac{\sqrt{\eta + a^2\cos^2\theta_o - \lambda^2/\tan^2\theta_o}}{\sqrt{r_o^2 + a^2\cos^2\theta_o}}\right],$$

---

[9] This is a reasonable assumption since it implies that, given an observer facing towards the BH, photons that are coming from the edge of the shadow are never received from "behind".

$$
\begin{aligned}
x' &= -\tilde{r}\,\mathrm{arctan}\left[\frac{p^{(\varphi)}/E}{p^{(r)}/E}\right]\\
&= -\tilde{r}\,\mathrm{arctan}\left[\frac{\lambda\sqrt{\rho^2\Delta}}{\sqrt{g_{\varphi\varphi}}\sqrt{r_o^4+(a^2-\eta-\lambda^2)r_o^2+2mr_o[\eta+(a-\lambda)^2]-\eta a^2}}\right].
\end{aligned}
$$

For the edge of the shadow the impact parameters λ, η are given by (1.4.10) as functions of the spherical photon orbit radius r (which is not the radial coordinate of the observer). The shadow's edge in the x', y' image plane is then defined parametrically by allowing r to vary in the range $r\in[r_1,r_2]$ (both defined in (1.4.11-1.4.12)).

A.7 Mapping $(\theta,\varphi)\to(\alpha,\beta)$ in flat space

In this section the mapping in flat space from the spherical coordinates (θ,φ) on a celestial sphere to the observation angles (α,β) is formulated (see page 1.5.1).

This mapping is useful to correct the parallax distortion due to the fact that the observer is not centered within the celestial sphere (see Fig. 1.5.9). Given a regular pattern imprinted on a "local sphere", which is centered on the observer, smaller than the celestial sphere and parametrized by the angles α,β, we can project the pattern on the celestial sphere via ray-tracing. Since in flat space rays follow straight lines this problem is purely euclidean geometry. After this projection is done, an observer would perceive the pattern on the celestial sphere undistorted; of course the projection itself is not uniform but from the observer's perspective it looks regular.

If this projection on the celestial sphere is locked for a curved space-time, a backward ray-tracing algorithm has to assign a pattern information to the point (θ,φ) on that sphere. This can be accomplished with the mapping $(\theta,\varphi)\to(\alpha,\beta)$ in flat space, given that the pattern is regular on those last coordinates (on the "local sphere").

Attending to Fig. A.7.1 we have

$$\vec{R}=\vec{r}-\vec{r}_o, \tag{A.7.1}$$

where those vectors are given by

$$
\begin{aligned}
\vec{r}_o &= r_o\,\hat{x}, && \text{(A.7.2a)}\\
\vec{r} &= r\sin\theta\,\cos\varphi\,\hat{x}+r\sin\theta\,\sin\varphi\,\hat{y}+r\cos\theta\,\hat{z}, && \text{(A.7.2b)}\\
\vec{R} &= -R\cos\beta\,\cos\alpha\,\hat{x}-R\sin\beta\cos\alpha\,\hat{y}+R\sin\alpha\,\hat{z}. && \text{(A.7.2c)}
\end{aligned}
$$

The value of $\vec{R}$ squared is

$$R^2=r^2+r_o^2-2\,\vec{r}\cdot\vec{r}_o$$

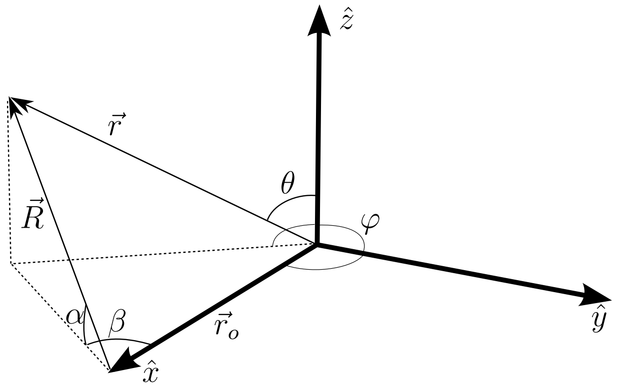

Figure A.7.1: Drawing of the geometric configuration. The observer is at position $\vec{r}_o$ and assumed to be on the equatorial plane ($\theta = \pi/2.$). A generic point on the celestial sphere is at position $\vec{r}$. The respective planes of α, β are perpendicular between themselves. All angles are drawn positive.

$$= r^2 + r_o^2 - 2\, r r_o \sin\theta\, \cos\varphi.$$

So we obtain

$$\boxed{R = \sqrt{r^2 + r_o^2 - 2\, r r_o \sin\theta\, \cos\varphi}}.$$

The vectorial equations (A.7.1-A.7.2) yield

$$r \sin\theta\, \cos\varphi = r_o - R\cos\beta\, \cos\alpha, \tag{A.7.3a}$$
$$r \sin\theta\, \sin\varphi = -R\sin\beta\, \cos\alpha, \tag{A.7.3b}$$
$$r \cos\theta = R\sin\alpha. \tag{A.7.3c}$$

From this set of equations we obtain

$$\sin\alpha = \frac{r\cos\theta}{R},$$

$$\sin\beta = -\frac{r\sin\theta\, \sin\varphi}{R\cos\alpha} \equiv A \qquad \text{and} \qquad \cos\beta = \frac{r_o - r\sin\theta\, \cos\varphi}{R\cos\alpha}.$$

We can now have the following algorithm to compute the value of β:

$$\text{if} \quad \cos\beta \geq 0 \implies \beta = \arcsin A;$$

$$\text{if} \quad \cos\beta < 0 \quad \text{and} \quad \sin\beta \geq 0 \implies \beta = \pi - \arcsin A;$$

$$\text{if} \quad \cos\beta < 0 \quad \text{and} \quad \sin\beta < 0 \implies \beta = -\pi - \arcsin A.$$

Because $\alpha \in [-\pi/2, \pi/2]$:

$$\alpha = \arcsin\left[\frac{r\cos\theta}{R}\right].$$

Appendix B

B.1 Bekenstein's no-scalar-hair theorem for V-scalar-vacuum

The following reasoning closely follows [52]. Units $G = 1, c = 1, \hbar = 1$ will be used.

Given a rotating, stationary, asymptotically flat BH with axial symmetry one may pose the question if it is possible to have a scalar field ϕ in equilibrium with it.

Assumption 1: the scalar field is minimally coupled to gravity. The Hilbert action functional $\mathcal{S}[g_{\mu\nu}, \phi]$ has then the form:

$$\mathcal{S}[g_{\mu\nu}, \phi] = \int d^4x\sqrt{-g}\left(\frac{R}{16\pi} - \nabla_\mu\phi\nabla^\mu\phi - 2V(\phi)\right),$$

where g is the determinant of the metric. Both the Einstein equations and the field equation for ϕ can be obtained from this functional by the variational principle. Then the scalar field should obey a generalized Klein-Gordon equation with a potential $V(\phi)$, which accounts for possible non-linear self-interactions but does not depend on the space-time curvature. For instance, one of simplest cases is a non-self-interacting massive scalar, for which $V(\phi) = \frac{1}{2}\mu^2\phi^2$, where μ stands for the mass of the particle; however such a specific case will not be considered. The generalized Klein-Gordon then yields:

$$\nabla_\mu\nabla^\mu\phi - V'(\phi) = 0,$$

where the derivative V' is taken with respect to the field ϕ.

Assumption 2: The scalar field ϕ has the same symmetries as the space-time, namely

$$\partial_t\phi = 0 = \partial_\varphi\phi.$$

The coordinates t, φ are chosen such that the vectors ∂_t and ∂_φ are the two Killing vectors related respectively to the space-time stationary symmetry and to axial symmetry. Multiplying the Klein-Gordon equation by ϕ and integrating over the BH exterior space-time leads to

$$\int d^4x\sqrt{-g}\,(\phi\nabla_\mu\nabla^\mu\phi - \phi V') = 0.$$

After integration by parts[1] of the **first** term we obtain

$$\int d^4x\sqrt{-g}\,(-\nabla_\mu\phi\nabla^\mu\phi - \phi V') + \int_{\mathcal{H}} d^3\sigma\,\phi\, n^\mu\nabla_\mu\phi = 0.$$

The contribution of the boundary term from infinity vanishes, since ϕ must decrease fast enough to ensure asymptotically flatness. The other boundary contribution from the BH's event horizon turns out also to be zero. The event horizon of a stationary, asymptotically flat space-time is a Killing horizon [1] and so the normal vector n^μ to the horizon surface is a combination of the Killing vector fields. Then due to the assumed symmetries for ϕ we must have

$$n^\mu\nabla_\mu\phi = 0.$$

This leads to

$$\int d^4x\sqrt{-g}\,(-\nabla_\mu\phi\nabla^\mu\phi - \phi V') = 0. \tag{B.1.1}$$

Assumption 3: The potential V follows the condition $\phi V' \geq 0$ everywhere. Since the gradient of ϕ is orthogonal to both Killing vectors, the gradient cannot be time-like:

$$\nabla_\mu\phi\nabla^\mu\phi \geq 0.$$

For equality (B.1.1) to hold, then we must have everywhere either $\phi = 0$ or $\phi = Const. \equiv \phi_i$, such that $V' = 0$ for that constant value of ϕ_i. For the last case, ϕ_i simply narrows down to a cosmological constant. This conclusion establishes the no-scalar-hair theorem.

B.2 Christoffel symbols for the HBH metric

For a Kerr Black Hole with Scalar Hair (KBHSH) the metric is given by the ansatz:

$$ds^2 = e^{2F_1}\left(\frac{dr^2}{N} + r^2 d\theta^2\right) + e^{2F_2} r^2 \sin^2\theta (d\varphi - W dt)^2 - e^{2F_0} N dt^2,$$

---

[1] The integration by parts can be done using the Divergence (or Gauss) Theorem, by selecting the integrating vector $\underline{F} = \phi\,\underline{\nabla}\phi$ [57].

with

$$N = 1 - \frac{r_H}{r}.$$

Therefore we have for the metric components $g_{\mu\nu}$:

$$g_{tt} = W^2 r^2 \sin^2\theta\, e^{2F_2} - N\, e^{2F_o}, \tag{B.2.1a}$$

$$g_{t\varphi} = -W r^2 \sin^2\theta\, e^{2F_2}, \tag{B.2.1b}$$

$$g_{\varphi\varphi} = r^2 \sin^2\theta\, e^{2F_2}, \tag{B.2.1c}$$

$$g_{rr} = \frac{e^{2F_1}}{N}, \tag{B.2.1d}$$

$$g_{\theta\theta} = r^2\, e^{2F_1}. \tag{B.2.1e}$$

For the inverse metric $g^{\mu\nu}$ the components are:

$$g^{tt} = \frac{g_{\varphi\varphi}}{g_{tt}\, g_{\varphi\varphi} - g_{t\varphi}^2} = -\frac{1}{N} e^{-2F_o}, \tag{B.2.2a}$$

$$g^{t\varphi} = -\frac{g_{t\varphi}}{g_{tt}\, g_{\varphi\varphi} - g_{t\varphi}^2} = -\frac{W}{N} e^{-2F_o}, \tag{B.2.2b}$$

$$g^{\varphi\varphi} = \frac{g_{tt}}{g_{tt}\, g_{\varphi\varphi} - g_{t\varphi}^2} = -\frac{W^2}{N} e^{-2F_o} + \frac{1}{r^2 \sin^2\theta} e^{-2F_2}, \tag{B.2.2c}$$

$$g^{rr} = \frac{1}{g_{rr}} = N e^{-2F_1}, \tag{B.2.2d}$$

$$g^{\theta\theta} = \frac{1}{g_{\theta\theta}} = \frac{1}{r^2} e^{-2F_1}, \tag{B.2.2e}$$

Due to symmetry the functions F_0, F_1, F_2 and W only depend on r and θ. The relevant Christoffel symbols Γ^k_{ij} for the $\ddot{r}$ and $\ddot{\theta}$ geodesic equations are:

$$
\begin{aligned}
&\Gamma^r_{tt} = \frac{e^{-2F_1}\,(r_H - r)\,A}{r^3} \\
&A = W r^4 \sin^2\theta e^{2F_2}\left(\frac{W}{r} + W_{,r} + W F_{2,r}\right) - r_H\, e^{2F_o}\left(\frac{r^2 F_{o,r}}{r_H} - r F_{o,r} + \frac{1}{2}\right) \\
&\Gamma^r_{rr} = \frac{2 r_H\, r F_{1,r} + r_H - 2\, r^2 F_{1,r}}{2\, r\,(r_H - r)} \\
&\Gamma^r_{\theta\theta} = \big(r F_{1,r} + 1\big)\,(r_H - r) \\
&\Gamma^r_{\varphi\varphi} = \sin^2\theta\, e^{2(F_2 - F_1)}\,\big(r F_{2,r} + 1\big)\,(r_H - r) \\
&\Gamma^r_{\varphi t} = -\frac{1}{2}\sin^2\theta\, e^{2(F_2 - F_1)}\,(r_H - r)\,\big(r\, W_{,r} + 2\, r F_{2,r} W + 2\, W\big) \\
&\Gamma^r_{\theta r} = F_{1,\theta} \\
&\Gamma^\theta_{tt} = -\frac{e^{-2F_1} B}{r^3} \\
&B = W r^3 e^{2F_2}(\sin^2\theta[W_{,\theta} + W F_{2,\theta}] + \cos\theta\, \sin\theta\, W) + F_{o,\theta}\, e^{2F_o}(r_H - r) \\
&\Gamma^\theta_{rr} = \frac{F_{1,\theta}}{r\,(r_H - r)} \\
&\Gamma^\theta_{\theta\theta} = F_{1,\theta} \\
&\Gamma^\theta_{\varphi\varphi} = -\sin\theta\, e^{2(F_2 - F_1)}\,\big(\sin\theta\, F_{2,\theta} + \cos\theta\big) \\
&\Gamma^\theta_{\varphi t} = \frac{1}{2}\sin\theta\, e^{2(F_2 - F_1)}\,\big(\sin\theta\, W_{,\theta} + 2\, W \sin\theta\, F_{2,\theta} + 2\, W \cos\theta\big) \\
&\Gamma^\theta_{\theta r} = F_{1,r} + \frac{1}{r}
\end{aligned}
$$

Bibliography

[1] V. P. Frolov and I. D. Novikov, *Black Hole Physics: Basic concepts and new developments.* Kluwer Academic Publishers, 1998.

[2] S. Gillessen, F. Eisenhauer, S. Trippe, T. Alexander, R. Genzel, F. Martins, and T. Ott, "Monitoring stellar orbits around the massive black hole in the galactic center," *The Astrophysical Journal*, vol. 692, no. 2, p. 1075, 2009.

[3] R. Narayan and J. E. McClintock, "Observational evidence for black holes," *arXiv preprint arXiv:1312.6698*, 2013.

[4] A. Phillips, *The Physics of Stars.* Manchester Physics Series, Wiley, 2013.

[5] L. Ryder, *Introduction to General Relativity.* Cambridge University Press, 2009.

[6] J. Hartle, *Gravity: An Introduction to Einstein's General Relativity.* Pearson Education, Limited, 2013.

[7] F. Tombesi, M. Meléndez, S. Veilleux, J. Reeves, E. González-Alfonso, and C. Reynolds, "Wind from the black-hole accretion disk driving a molecular outflow in an active galaxy," *Nature*, vol. 519, no. 7544, pp. 436–438, 2015.

[8] S. M. Carroll, *Lecture Notes on General Relativity.* University California, 1997.

[9] C. Herdeiro. Private talk held in Aveiro University, Portugal, February 2015.

[10] J. Mathews and R. L. Walker, *Mathematical methods of physics*, vol. 271. WA Benjamin New York, 1970.

[11] M. Visser, "The kerr spacetime: A brief introduction," *arXiv preprint arXiv:0706.0622*, 2007.

[12] S. W. Hawking, *The large scale structure of space-time*, vol. 1. Cambridge university press, 1973.

[13] R. Penrose and R. Floyd, "Extraction of rotational energy from a black hole," *Nature*, vol. 229, no. 6, pp. 177–179, 1971.

[14] P. C. v. d. Wijk, *The Kerr-Metric: describing Rotating Black Holes and Geodesics.* Groningen University, 2007.

[15] M. Begelman and M. J. Rees, *Gravity's Fatal Attraction.* Scientific American Library, 1996.

[16] P. K. Townsend, "Black holes," *arXiv preprint gr-qc/9707012*, 1997.

[17] D. C. Wilkins, "Bound geodesics in the kerr metric," *Physical Review D*, vol. 5, no. 4, p. 814, 1972.

[18] H. Goldstein, *Classical Mechanics, 2nd edition.* Addison-Wesley, 1980.

[19] B. Carter, "Global structure of the kerr family of gravitational fields," *Phys. Rev.*, vol. 174, pp. 1559–1571, Oct 1968.

[20] S. Chandrasekhar, *The Mathematical Theory of Black Holes.* Oxford classic texts in the physical sciences, Clarendon Press, 1998.

[21] C. Misner, K. Thorne, and J. Wheeler, *Gravitation.* W. H. Freeman, 1973.

[22] J. M. Bardeen, *Timelike and null geodesies in the Kerr metric.* C. Witt and B. Witt, editors, Black Holes, pp.215, 1973.

[23] E. Teo, "Spherical photon orbits around a kerr black hole," *General Relativity and Gravitation*, vol. 35, no. 11, pp. 1909–1926, 2003.

[24] B. Schutz, *A first course in general relativity.* Cambridge university press, 2009.

[25] J. Brink, M. Geyer, and T. Hinderer, "Orbital resonances around black holes," *Physical review letters*, vol. 114, no. 8, p. 081102, 2015.

[26] M. Abramowitz and I. Stegun, *Handbook of Mathematical Functions: With Formulas, Graphs, and Mathematical Tables.* Applied mathematics series, Dover Publications, 1964.

[27] W. H. Press, *Numerical recipes 3rd edition: The art of scientific computing.* Cambridge university press, 2007.

[28] T. Johannsen, "Photon rings around kerr and kerr-like black holes," *The Astrophysical Journal*, vol. 777, no. 2, p. 170, 2013.

[29] J. Luminet, *How Black Holes Affect Gravity.* Astronomical Review. 6(7), 5-7, 2011.

[30] Riazuelo, *A 2008 Voyage au Coeur d'u Trou Noir, a DVD (Paris: Science et Avenir);.* http://www.sciencesetavenir.fr/espace/20120925.OBS3469/voyage-au-coeur-d-un-trou-noir-dvd.html.

[31] Riazuelo, *A 2014 Simulation of starlight lensed by a camera orbiting a Schwarzschild black hole,.* www2.iap.fr/users/riazuelo/interstellar.

[32] O. James, E. von Tunzelmann, P. Franklin, and K. S. Thorne, "Gravitational lensing by spinning black holes in astrophysics, and in the movie interstellar," *Classical and Quantum Gravity*, vol. 32, no. 6, p. 065001, 2015.

[33] O. James, E. von Tunzelmann, P. Franklin, and K. S. Thorne, "Visualizing interstellar's wormhole," *arXiv preprint arXiv:1502.03809*, 2015.

[34] F. H. Vincent, T. Paumard, E. Gourgoulhon, and G. Perrin, "Gyoto: a new general relativistic ray-tracing code," *Classical and Quantum Gravity*, vol. 28, no. 22, p. 225011, 2011.

[35] Wilson Morgado, Website of original Aveiro image: http://www.panoramio.com/user/716417?with_photo_id=49459377.

[36] ESA/Nasa, Website of the Hubble Telescope's image: http://www.spacetelescope.org/images/heic0607a/.

[37] Alan Dyer, Website of Milky Way image: http://amazingsky.net/2011/10/01/milky-way-mosaic/.

[38] GYOTO manual's website: http://gyoto.obspm.fr.

[39] D. N. Page and K. S. Thorne, "Disk-accretion onto a black hole. time-averaged structure of accretion disk," *The Astrophysical Journal*, vol. 191, pp. 499–506, 1974.

[40] H. Falcke, F. Melia, and E. Agol, "Viewing the shadow of the black hole at the galactic center," *The Astrophysical Journal Letters*, vol. 528, no. 1, p. L13, 2000.

[41] R.-S. Lu, A. E. Broderick, F. Baron, J. D. Monnier, V. L. Fish, S. S. Doeleman, and V. Pankratius, "Imaging the supermassive black hole shadow and jet base of m87 with the event horizon telescope," *The Astrophysical Journal*, vol. 788, no. 2, p. 120, 2014.

[42] V. L. Fish, "Observing a black hole event horizon:(sub) millimeter vlbi of sagittarius a*," in *IAU Symposium# 261, American Astronomical Society*, vol. 261, p. 1304, 2009.

[43] S. S. Doeleman, J. Weintroub, A. E. Rogers, R. Plambeck, R. Freund, R. P. Tilanus, P. Friberg, L. M. Ziurys, J. M. Moran, B. Corey, *et al.*, "Event-horizon-scale structure in the supermassive black hole candidate at the galactic centre," *Nature*, vol. 455, no. 7209, pp. 78–80, 2008.

[44] H. Bartko, G. Perrin, W. Brandner, C. Straubmeier, A. Richichi, S. Gillessen, T. Paumard, S. Hippler, A. Eckart, M. Schöller, *et al.*, "Gravity: Astrometry on the galactic center and beyond," *New Astronomy Reviews*, vol. 53, no. 11, pp. 301–306, 2009.

[45] T. Johannsen and D. Psaltis, "Testing the no-hair theorem with observations in the electromagnetic spectrum. iii. quasi-periodic variability," *The Astrophysical Journal*, vol. 726, no. 1, p. 11, 2011.

[46] S. S. Doeleman, V. L. Fish, A. E. Broderick, A. Loeb, and A. E. Rogers, "Detecting flaring structures in sagittarius a* with high-frequency vlbi," *The Astrophysical Journal*, vol. 695, no. 1, p. 59, 2009.

[47] F. Eisenhauer, G. Perrin, W. Brandner, C. Straubmeier, A. Richichi, S. Gillessen, J. Berger, S. Hippler, A. Eckart, M. Schöller, *et al.*, "Gravity: getting to the event horizon of sgr a*," in *SPIE Astronomical Telescopes+ Instrumentation*, pp. 70132A–70132A, International Society for Optics and Photonics, 2008.

[48] J. D. Bekenstein, "Black hole hair: twenty–five years after," *arXiv preprint gr-qc/9605059*, 1996.

[49] C. A. Herdeiro and E. Radu, "Kerr black holes with scalar hair," *Physical review letters*, vol. 112, no. 22, p. 221101, 2014.

[50] T. Johannsen and D. Psaltis, "Testing the no-hair theorem with observations in the electromagnetic spectrum. i. properties of a quasi-kerr spacetime," *The Astrophysical Journal*, vol. 716, no. 1, p. 187, 2010.

[51] T. Johannsen and D. Psaltis, "Testing the no-hair theorem with observations in the electromagnetic spectrum. ii. black hole images," *The Astrophysical Journal*, vol. 718, no. 1, p. 446, 2010.

[52] C. A. Herdeiro and E. Radu, "Asymptotically flat black holes with scalar hair: a review," *arXiv preprint arXiv:1504.08209*, 2015.

[53] K. Thorne, *The Science of Interstellar.* WW Norton & Company, 2014.

[54] T. Johannsen, "Testing the no-hair theorem with sgr a*," *Advances in Astronomy*, vol. 2012, 2011.

[55] T. Johannsen and D. Psaltis, "Testing the no-hair theorem with observations in the electromagnetic spectrum. iv. relativistically broadened iron lines," *The Astrophysical Journal*, vol. 773, no. 1, p. 57, 2013.

[56] C. Herdeiro and E. Radu, "Construction and physical properties of kerr black holes with scalar hair," *arXiv preprint arXiv:1501.04319*, 2015.

[57] J. Jackson, *Classical Electrodynamics.* Wiley, 1998.

[58] V. Cardoso, Ó. J. Dias, J. P. Lemos, and S. Yoshida, "Black-hole bomb and superradiant instabilities," *Physical Review D*, vol. 70, no. 4, p. 044039, 2004.

[59] P. Pani, V. Cardoso, L. Gualtieri, E. Berti, and A. Ishibashi, "Black-hole bombs and photon-mass bounds," *Physical review letters*, vol. 109, no. 13, p. 131102, 2012.

[60] M. Zilhão, H. Witek, and V. Cardoso, "Nonlinear interactions between black holes and proca fields," *arXiv preprint arXiv:1505.00797*, 2015.

[61] W. H. Press and S. A. Teukolsky, "Floating orbits, superradiant scattering and the black-hole bomb," Nature 238, 211 - 212, (1972).

[62] R. Brito, V. Cardoso, and P. Pani, "Superradiance," *arXiv preprint arXiv:1501.06570*, 2015.

[63] S. Hod, "Stationary scalar clouds around rotating black holes," *Physical Review D*, vol. 86, no. 10, p. 104026, 2012.

[64] J. Sakurai and J. Napolitano, *Modern Quantum Mechanics.* Addison-Wesley, 2011.

[65] C. L. Benone, L. C. Crispino, C. Herdeiro, and E. Radu, "Kerr-newman scalar clouds," *Physical Review D*, vol. 90, no. 10, p. 104024, 2014.

[66] C. A. Herdeiro and E. Radu, "A new spin on black hole hair," *International Journal of Modern Physics D*, vol. 23, no. 12, p. 1442014, 2014.

[67] S. L. Liebling and C. Palenzuela, "Dynamical boson stars," *Living Rev. Relativity*, vol. 15, no. 6, 2012.

[68] F. E. Schunck and E. W. Mielke, "Topical review: General relativistic boson stars," *arXiv preprint arXiv:0801.0307*, 2008.

[69] C. A. Herdeiro and E. Radu, “How fast can a black hole rotate?,” *arXiv preprint arXiv:1505.04189*, 2015.

[70] C. Herdeiro and E. Radu, “Ergosurfaces for kerr black holes with scalar hair,” *Physical Review D*, vol. 89, no. 12, p. 124018, 2014.

[71] P. V. P. Cunha, C. A. R. Herdeiro, E. Radu, and H. F. Runarsson, “Shadows of kerr black holes with scalar hair,” *arXiv preprint arXiv:1509.00021, gr-qc*, 2015.

[72] D. Psaltis and T. Johannsen, “A ray-tracing algorithm for spinning compact object spacetimes with arbitrary quadrupole moments. i. quasi-kerr black holes,” *The Astrophysical Journal*, vol. 745, no. 1, p. 1, 2012.

[73] A. Bohn, W. Throwe, F. Hébert, K. Henriksson, D. Bunandar, M. A. Scheel, and N. W. Taylor, “What does a binary black hole merger look like?,” *Classical and Quantum Gravity*, vol. 32, no. 6, p. 065002, 2015.

[74] R. Nickalls, “Viète, descartes and the cubic equation,” *The Mathematical Gazette*, pp. 203–208, 2006.

[75] B. Anderson, J. Jackson, and M. Sitharam, “Descartes’ rule of signs revisited,” *Amer. Math. M.*, vol. 105, pp. 447–451, May 1998.